X-ray Study of Strain, Composition, Elastic energy and Atomic ordering in Ge islands on Si(001)

Ângelo Malachias de Souza

2005

X-ray Study of Strain, Composition, Elastic energy and Atomic ordering in Ge islands on Si(001)

Ângelo Malachias de Souza

Thesis submitted to the UNIVERSIDADE FEDERAL DE MINAS GERAIS as a partial requirement for obtaining the Ph.D. degree in Physics.

Thesis supervisor: Prof. Dr. Rogério Magalhães Paniago (UFMG)
Thesis co-supervisors: Dr. Gilberto Medeiros Ribeiro (LNLS)
Dr. Till Hartmut Metzger (ESRF – Grenoble)

Departamento de Física – ICEx – UFMG
2005

To Ângela

Agradecimentos – Acknowledgements – Remerciements

Professor Rogério Paniago, pelo interesse sincero na minha formação como cientista. Durante todo o doutorado não me deparei com qualquer entrave ou obstáculo que, graças ao seu empenho, não tenha sido contornado. Sou grato pelos conselhos e discussões (científicos ou não).

Dr. Gilberto Medeiros Ribeiro, pelo extremo otimismo e espírito crítico, capazes de remover nossas análises e interpretações do lugar comum. Agradecer-lhe pelas amostras é um mero detalhe...

Dr. Hartmut Metzger for his warm hospitality during my stay in Grenoble, for the confidence and freedom he gave me, for the nice and positive atmosphere of his group and for being open towards many (unscheduled) scientific discussions.

Dr. Stefan Kycia, for the crucial improvements of the diffraction beamlines at LNLS that made this work possible and for sharing his experimental knowledge. I also have to thank his continuous support during many experiments.

Dr. Tobias Schülli, for the productive collaboration. Our interaction has been a continuous source of ideas, learning and motivation.

Dr. Václav Holý, for his interest and kindly advice in the interpretation of x-ray measurements.

Dr. David Cahill, Dr. Martin Schmidbauer, Dr. Oliver Schmidt and Dr. Mathieu Stoffel for their invaluable support with samples, ideas and criticisms.

Luiz Gustavo Cançado, pela ajuda com as medidas de Raman e análise dos resultados.

Agradeço aos colegas do Laboratório de Nanoscopia, Prof. Bernardo, Giselle, Bráulio, Elisângela, Lino, Ana Paula, Ivonete e Mariana, por, no convívio diário, me contagiar com seu bom humor (mesmo nos dias mais tensos).

Agradeço aos amigos do Departamento de Física da UFMG, Prof. Luiz Cury, Gustavo Sáfar, Daniel Elias, Letícia Coelho, Guilherme José e Antônio Francisco Neto por manterem um ambiente profissional agradável e acolhedor. Este agradecimento é extensivo a todos aqueles que comigo conviveram durante esses últimos quatro anos.

Sou grato a Marluce, Idalina e Júlio, pela extrema eficiência com que resolveram meus problemas burocráticos, tratando minha tradicional ansiedade com paciência infinita.

I must thank Dr. Luciana Capello, Dr. Bärbel Krause and Dr. Michael Sztucki for their friendship, hospitality and assistance concerning the use of beamline ID01.

Je tiens a remercier Dr. Olivier Plantevin, Dr. Bruno Jean et Hamid Djazouli pour leur aide technique, leurs précieux conseils dans le domaine administratif, ainsi que pour leurs encouragements.

Dr. Peter Böescke for bringing successful, immediate and efficient solutions to all technical problems at beamline ID01. I also thank Dr. Cristian Mocuta for interesting scientific discussions and for his optimism.

Je remercie Mme Leila Van Yzendhorn pour m'avoir aidé à resoudre mes problèmes pratiques (surtout logement et documentation). Mes remerciements vont également à Mme Martine Cédile pour m'avoir appris, courageusement, un peu de français.

Agradeço aos amigos Ernesto Paiser (extensivo à Laura, Laurent e Sophie) e Ricardo Hino (também Natalie, Cecília, Emma e Lisa) pelos agradáveis momentos em família que compartilharam comigo em Grenoble.

Sou grato a Leide, Júlio, Daniela e Fabiano pelo apoio constante e pelas divertidas reuniões.

Agradeço profundamente à minha mãe pelo carinho e esforço dedicados a minha educação e crescimento moral. Ao meu pai devo agradecer por sempre me alegrar nas horas boas ou ruins e pelas nossas conversas de onde tirava uma incrível sabedoria prática. Não há um único dia em que não sinta a falta dos dois (espero ter crescido frente às expectativas deles...).

Sou muito grato a Marina por ter estado sempre ao meu lado nos momentos difíceis que enfrentamos, principalmente nos primeiros anos do doutorado.

Agradeço aos meus amigos Bruno Friche, Fred, Camilo, Léo π e Bruno Durão pelo estímulo e amizade.

Sou imensamente grato à Ângela Maria, João Calixto, Cláudia e Flávia pela constante ajuda e apoio.

Tia Ione, Tio Marcos, Juliana, Cristina, Mariza, Luís e Emerson por resgatarem minha alegria do convívio com a família, também pelo carinho e atenção.

Tia Dirce por estar por perto em todas as horas, com seu otimismo e senso prático.

Tia Gilda pelo carinho e incentivo.

Às instituições cujo apoio financeiro e logístico foi indispensável ao longo deste trabalho: UFMG, CNPq, LNLS, CAPES e ESRF.

Abstract

X-ray diffraction techniques were employed here to study several structural and chemical properties of Ge:Si(001) islands. Grazing incidence diffraction was used to map the strain status of Ge pyramids and domes. By tuning the x-ray energy near the Ge K edge – to perform anomalous diffraction measurements – it was possible to determine the chemical composition of both types of islands. The elastic energy was directly evaluated and found to be one of the driving forces of morphological evolution in this system. These results were extended by a new analysis method to a complete three-dimensional chemical and structural mapping of Ge domes. Finally, the existence of SiGe ordered alloys was observed inside domes, indicating the important rule played by surface kinetics on Si interdiffusion.

Resumo

Neste trabalho foram utilizadas técnicas de difração de raios-x para estudar propriedades químicas e estruturais de ilhas de Ge:Si(001). Através de experimentos de difração por incidência rasante foi realizado um mapeamento estrutural da relaxação de strain dentro de pirâmides e domos de Ge. Alterando-se a energia dos raios-x próximo à borda K do Ge – em medidas de difração anômala – foi possível determinar a composição química dos dois tipos de ilhas. A energia elástica, obtida correlacionando-se estes dois resultados, provou ser um dos fatores responsáveis pelas transições morfológicas neste sistema. Uma extensão dos resultados, com o uso de um novo método de análise, permitiu um completo mapeamento tri-dimensional da estrutura e estequiometria dos domos de Ge. Por último, foi observada a existência de uma liga ordenada de SiGe dentro dos domos, indicando o importante papel da cinética de crescimento na incorporação de Si nas ilhas.

CONTENTS

Introduction

Nanostructured materials have attracted the interest of basic and applied research during the last two decades. The eletronic response of one–dimensional and zero–dimensional systems such as self assembled semiconductor islands (quantum dots) and nanowires, fulerenes, carbon nanotubes and polymers strongly depend on their morphological, structural and chemical properties.

In this thesis the x-ray diffraction technique is employed to study the most relevant features of self-assembled Ge:Si(001) islands. Three-dimensional maps were obtained for the following parameters:

1) strain, that influences semiconductor band alignment and the quantum efficiency of nanostructures;
2) composition, that changes the confining profile (by changing the energy bandgap);
3) elastic energy, that may render an island ensemble stable, with a preferred shape and a fixed size distribution, directly related to the width of spectral and eletronic response of these materials;
4) atomic order, that can also affect the band alignment.

The knowledge of this set of information is crucial not only for the engineering of applied devices but also for understanding basic mechanisms that govern self-assembled island growth.

Chapter 1

X-ray Scattering at Surfaces

1.1 Synchrotron Radiation

Synchrotron facilities have become essential in many fields of science. There are many advantages in using synchrotron radiation instead of conventional x-ray sources: energy tunability, polarization, coherence and high brilliance. These properties lead to the development of x-ray techniques such as scattering, spectroscopy, imaging and time-resolved studies. A detailed introduction to synchrotron radiation can be found in [AlsNielsen01] and [Michette01].

The measurements shown in this thesis were performed at the Brazilian National Source LNLS (Laboratório Nacional de Luz Síncrotron), located in Campinas and at the ESRF (European Synchrotron Radiation Facility), located in Grenoble (France). All experiments described in this thesis profit from the tunability of the x-ray photon energy for anomalous scattering and from the high brilliance of these facilities. Since this work is based on the analysis of surface reflections and superstructure peaks the use of enhanced brightness synchrotron sources was imperative. The emission spectra of ESRF and LNLS are shown in fig. 1.1.

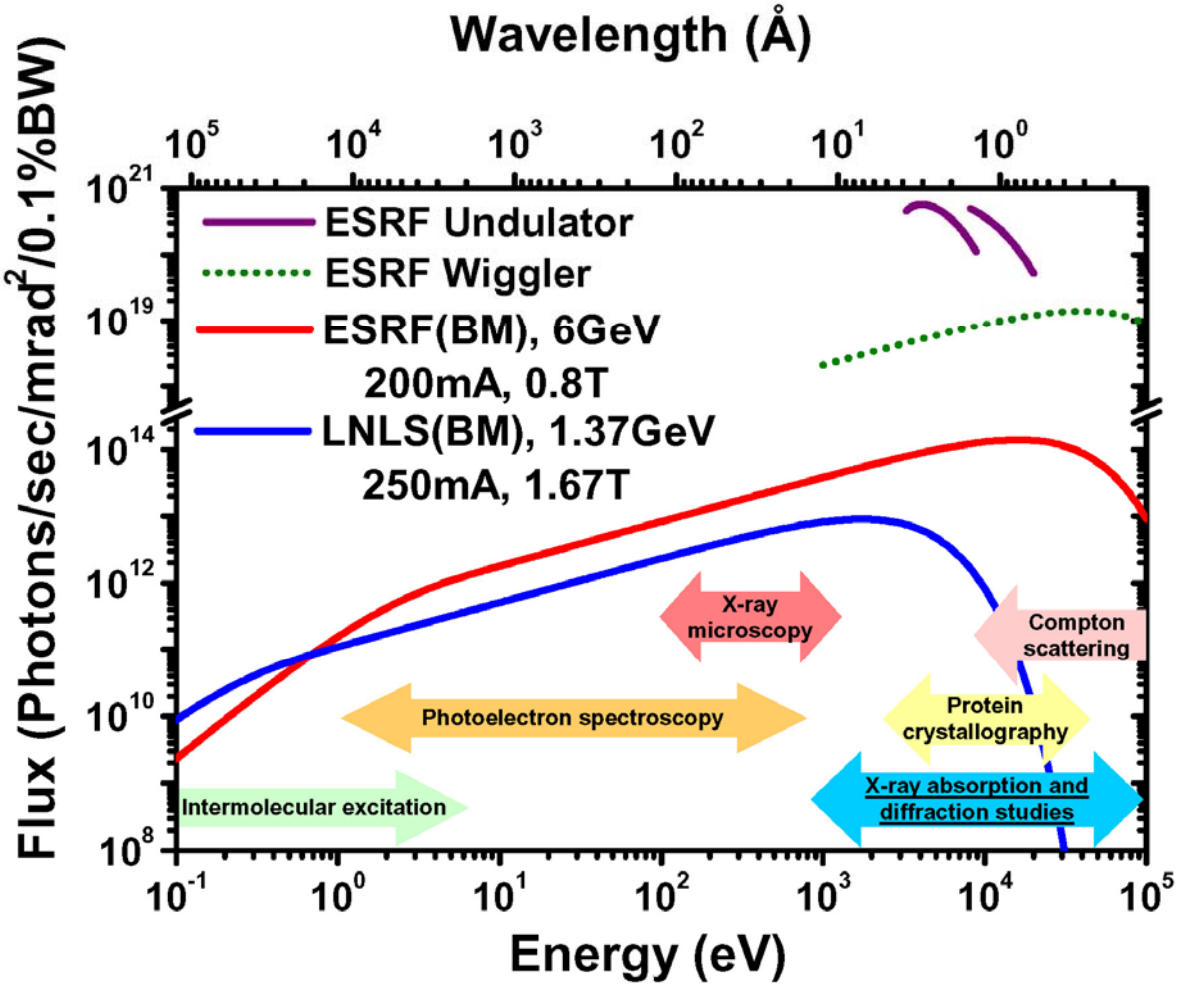

Fig. 1.1: Schematic representation of synchrotron radiation spectral range. The bremsstrahlung curves for LNLS and ESRF bending magnets (BM) beamlines are represented by blue and red solid lines, respectively. The graph also shows the spectral response of an ESRF wiggler (W70 – green dashed line) and an undulator (U42 – purple solid line). Arrows indicate the typical photon energies used for selected x-ray techniques.

Two beamlines of the LNLS are dedicated to x-ray diffraction in single crystals: XRD1 and XRD2. Both operate in an energy range between 4 and 12 KeV (wavelength range between 3 and 1 Å). Their optics systems are essentially the same. A gold-coated silicon mirror is used to remove high energy photons, focusing the white beam vertically. A double crystal Si(111) sagital monochromator makes the horizontal focalization. XRD1 beamline is equipped with a 2+1 circle diffractometer. It consists of a theta-2theta vertical table and an independent horizontal circle (α_i) that allows the adjustment of the x-ray incident angle. A 4-circle Huber diffractometer is installed at the XRD2 beamline, allowing

measurements in different (and more complex) geometries such as reciprocal-space mapping of asymmetric reflections.

At the ESRF all experiments were performed at the ID01 beamline, which is equipped with an insertion device (undulator or wiggler, depending on the energy range) to increase the photon flux. The optics hutch is equipped with two Si mirrors and a sagital double crystal Si(111) monochromator. The intensity of the monochromatic beam at 8KeV is approximately 10^6 times larger than a bending magnet beamline of LNLS. The ID01 beamline is equipped with a 4+2-circle diffractometer where four degrees of freedom are used to sample positioning and two for the detector movement.

A schematic representation of the x-ray optic elements of XRD1/2 and ID01 beamlines is shown in fig. 1.2.

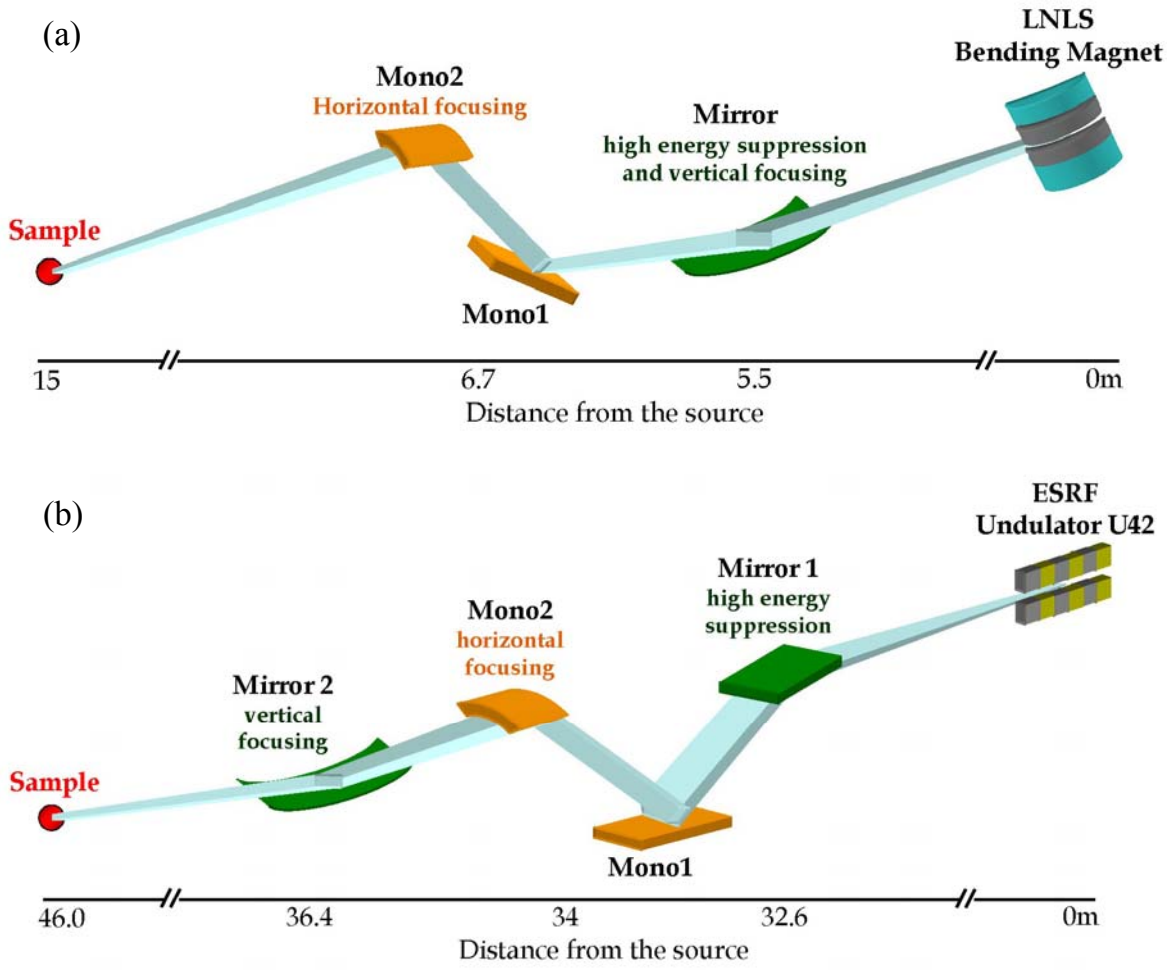

Fig. 1.2 - (a) Sketch of X-ray optical elements of XRD1/2 (LNLS) beamlines. (b) ID01 optics hutch scheme.

Fig. 1.3 shows the diffractometers of the three beamlines and their movements.

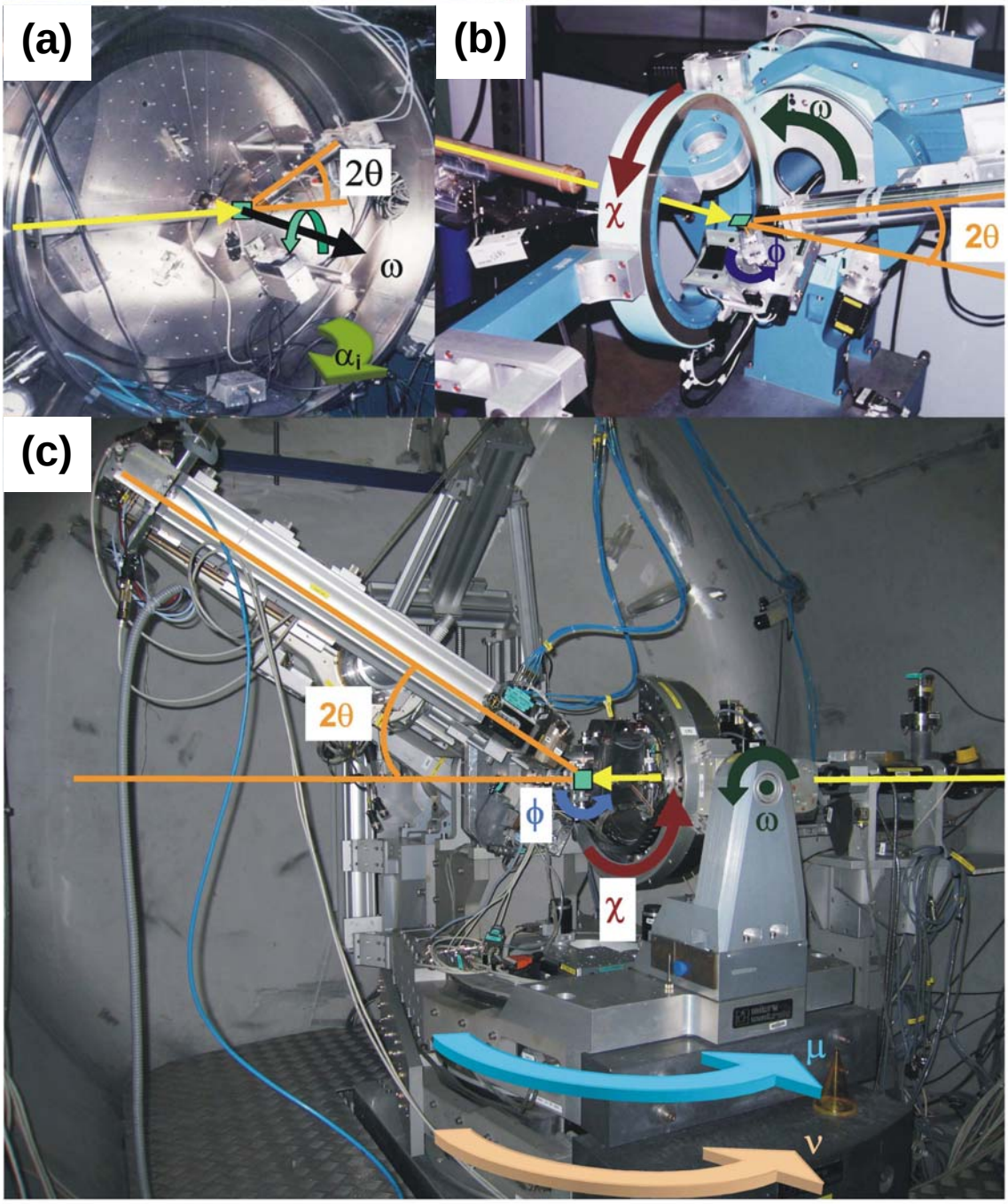

Fig. 1.3 – Diffractometers of (a) XDR1 and (b) XRD2 beamlines at LNLS and (c) ID01 beamline at ESRF. The x-ray path is indicated by the yellow line while diffractometer movements are represented by arrows.

In the next sections the x-ray background of this work is given in three main parts. Initially we discuss the x-ray kinematical diffraction formalism used in the determination of

structural parameters along this thesis. Section 1.2 is dedicated to atomic scattering factor and its dependence on the x-ray photon energy. A brief introduction to the use of anomalous (resonant) x-ray scattering to obtain chemical contrast is found in this section. Form factor and structure factor calculations are shown in section 1.3 and 1.4, respectively. Finally, in section 1.5 we discuss the x-ray technique which is employed here to investigate structures on the near-surface region: Grazing Incidence Diffraction.

1.2 Atomic scattering factor and anomalous x-ray scattering

Essentially two types of interaction can occur when an x-ray photon falls on an atom. The photon may be absorbed by the atom, with ejection of an electron or it can be scattered. It is useful to start a description of these processes from the most simple case: the elastic scattering of a photon by a single electron following the classical theory. If the radiation is unpolarized the acceleration of the electron will be given by the force of the electromagnetic field from the incident wave $E_0e^{-i\omega t}$ acting on the particle that has charge q and mass m: [Jackson99]

$$\mathbf{a} = \frac{\mathbf{f}}{m} = \frac{qE_0 e^{i\omega t}}{m}. \tag{1.1}$$

According to the electromagnetic theory an accelerated charge radiates. The radiated energy is proportional to the square of the radiated field $\mathbf{E_{rad}}$. Then, E_{rad} must decrease as $1/R$. Since the elementary scattering unity of an X-ray in an atom is the electron the field is proportional to its charge $-e$ and to the acceleration $a(t')$ evaluated at a time $t'=t-R/c$ earlier than the observation time t (the radiation propagates at a finite velocity c). The electric field that results from this acceleration is given by:

$$\mathbf{E_{rad}} = -\frac{-ea(t')}{4\pi\varepsilon_0 c^2 R} \tag{1.2}$$

where the term $1/(4\pi\varepsilon_0 c^2)$ was included to make eq. 1.2 dimensionally correct. By using equation 1.1 in 1.2:

$$\mathbf{E}_{\mathbf{rad}}(R,t) = -\frac{-e}{4\pi\varepsilon_0 c^2 R}\frac{-e}{m}\mathbf{E}_{\mathbf{in}} e^{i\omega\left(\frac{R}{c}\right)} \cos\psi$$
$$\Rightarrow \frac{\mathbf{E}_{\mathbf{rad}}(R,t)}{\mathbf{E}_{\mathbf{in}}} = -\left(\frac{e^2}{4\pi\varepsilon_0 mc^2}\right)\frac{e^{ikR}}{R}\cos\psi \quad , \tag{1.3}$$

where $k=\omega/c$ and $\mathbf{E_{in}}= E_0 e^{-i\omega t}$. The the position of the observer relatively to the acceleration direction is represented by the inclusion of the term $\cos\psi$. For $\psi=\pi/2$ the observer does not see any acceleration while for $\psi=0$ the full acceleration is observed. The prefactor of the spherical wave e^{ikR}/R is denoted by $r_0=(e^2/4\pi\varepsilon_0 mc^2)$ and known as the classical electron radius [Jackson99, AlsNielsen01].

1.2.1 Atomic form factor

In the preceding pages the x-ray scattering was calculated considering one free electron. However, in real atoms the electrons are spatially restricted to a small volume around the nucleus. The atom is then viewed by x-rays as a charge cloud with a number density $\rho(\mathbf{r})$. The charge in a volume element $d\mathbf{r}$ at a position $\mathbf{r}$ is, then, given by $-e\rho(\mathbf{r})d\mathbf{r}$. To evaluate the scattering amplitude one must weight the element contribution $d\mathbf{r}$ by the phase factor $e^{i\mathbf{q}\cdot\mathbf{r}}$ and integrate over $d\mathbf{r}$. This leads to the form factor of one atom, which is also known as the **Q**-dependent part of the *atomic scattering factor*:

$$f_0(\mathrm{Q}) = \int \boldsymbol{\rho}(\mathbf{r}) e^{i\mathbf{Q}\cdot\mathbf{r}} d\mathbf{r} \, . \tag{1.4}$$

At Q = 0 the result of eq. 1.4 is the total number of electrons Z in the atom. One can assume, for simplicity, that the charge density has spherical symmetry with the hydrogen-like form

$$\rho = (e^{-2r/a})/(\pi a^3) \tag{1.5}$$

where a is the effective radius of the charge distribution. Eq. 1.4 can be re-written in spherical polar coordinates in the following way:

$$
\begin{aligned}
f_0(\mathrm{Q}) &= \frac{1}{\pi a^3}\int_{r=0}^{\infty} 2\pi r^2 e^{-2r/a}\int_{\theta=0}^{\pi} e^{iQr\cos\theta}\sin\theta\, d\theta\, dr \\
&= \frac{1}{\pi a^3}\int_{r=0}^{\infty} 2\pi r^2 e^{-2r/a}\frac{1}{iqr}\left[e^{iQr}-e^{-iQr}\right]dr \\
&= \frac{1}{\pi a^3}\int_{r=0}^{\infty} 2\pi r^2 e^{-2r/a}\frac{2\sin(Qr)}{Qr}dr
\end{aligned}
\qquad (1.6)
$$

The integrand is independent of the azimutal angle ϕ so that the volume element becomes $2\pi r^2 \sin\theta d\theta dr$. In order to solve eq. 1.6 the term *sin(qr)* is written as the imaginary part of a complex exponential. Then,

$$
f_0(\mathrm{Q}) = \frac{4}{qa^3}\,Im\left\{\int_{r=0}^{\infty} re^{-2r/a}e^{iQr}dr\right\} = \frac{4}{qa^3}\,Im\left\{\int_{r=0}^{\infty} re^{-r\left(2/a-iQ\right)}dr\right\} \qquad (1.7)
$$

that may be integrated by parts to yield the final result

$$
f_0(\mathrm{Q}) = \frac{1}{\left[1+(Qa/2)^2\right]^2}. \qquad (1.8)
$$

The atomic form factor $f_0(\mathrm{Q})$ given by eq. 1.8 and the form factors of Si and Ge atoms are plotted in fig. 1.4. These results refer to isolated atoms with spherical symmetry. In a real crystal this symmetry is modified by the lattice and also depends on the type of atomic bond (i.e, covalent or ionic).

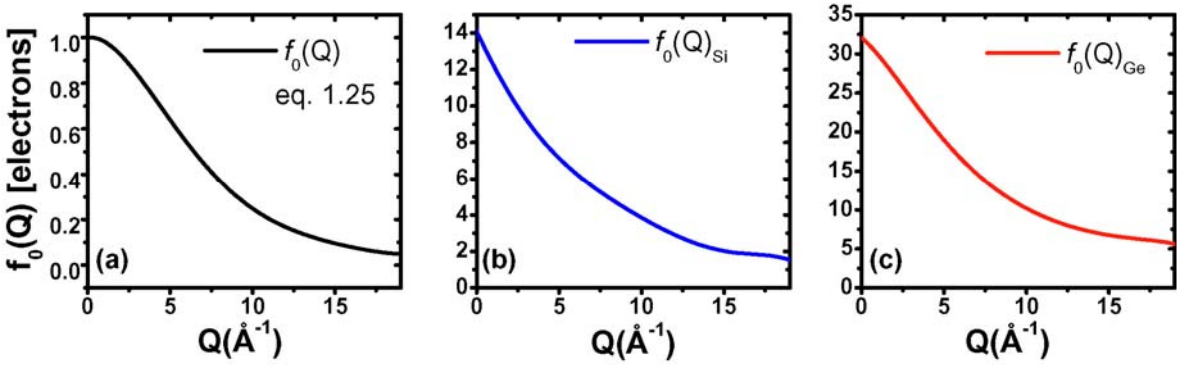

Fig. 1.4 – Atomic form factors (Q-dependent part of the atomic scattering factor) of (a) hydrogen-like atom (eq. 1.8 with a = 0.2Å), (b) Si atom (Z = 14) and (c) Ge atom (Z = 32). The experimental results of (b) and (c) were taken from ref. [Warren69].

1.2.2 Anomalous (resonant) x-ray scattering

The simple treatment of the atomic scattering factor outlined above is based in the assumptions that the x-ray wavelength is smaller than any absorption edge wavelengths in the atoms. In case this condition is not satisfied dispersion corrections are necessary. These corrections take into account the fact that electrons are found in bound states of an atom. Although the quantitative calculation of such corrections can be performed only by using quantum mechanics formalism it is still possible to use a classical model to understand their physical meaning. Let the incident field be polarized along the x axis, with amplitude E_0 and frequency ω, $\mathbf{E_{in}}=\mathbf{x}E_0e^{-i\omega t}$. The equation of a forced charge oscillator describes the motion of the electron [Jackson99, AlsNielsen01]:

$$\ddot{x}+\gamma\dot{x}+\omega_s^2 x=\mathbf{f}=-\left(\frac{eE_0}{m}\right)e^{-i\omega t}\ . \tag{1.9}$$

This equation has a velocity dependent damping term $\gamma\dot{x}$ that represents the dissipation of the applied field and a resonant term with frequency ω_s (usually much bigger than the γ). Using a trial solution $x(t)=x_0e^{-i\omega t}$ the amplitude x_0 of the forced oscillator is given by:

$$x_0=-\left(\frac{eE_0}{m}\right)\frac{1}{\left(\omega_s^2-\omega^2-i\omega\gamma\right)}. \tag{1.10}$$

Similarly to equation 1.2 the radiated field is evaluated at the earlier time $t'=t-R/c$

$$\mathbf{E_{rad}}(R,t)=-\left(\frac{-e}{4\pi\varepsilon_0c^2R}\right)\ddot{x}(t-R/c)\,. \tag{1.11}$$

Inserting $\ddot{x}(t-R/c)=-\omega^2x_0e^{-i\omega t}e^{i(\omega/c)R}$ and x_0 given by equation 1.11 leads to

$$\begin{aligned}\mathbf{E_{rad}}(R,t)&=\frac{\omega^2}{\left(\omega_s^2-\omega^2-i\omega\gamma\right)}\left(\frac{e^2}{4\pi\varepsilon_0c^2m}\right)E_0e^{-i\omega t}\left(\frac{e^{ikR}}{R}\right)\\ \Rightarrow\frac{\mathbf{E_{rad}}(R,t)}{\mathbf{E_{in}}}&=-r_0\frac{\omega^2}{\left(\omega^2-\omega_s^2+i\omega\gamma\right)}\left(\frac{e^{ikR}}{R}\right)\end{aligned}\ . \tag{1.12}$$

The amplitude of the outgoing wave (in units of $-r_0$) is given by the atomic scattering length $f_s=\omega^2/(\omega^2-\omega_s^2+i\omega\gamma)$.

For frequencies that are larger than the resonant frequency ($\omega >> \omega_s$) the electron can be considered free and equation 1.12 change its form to 1.3. The expression for f_s can be rearranged in the following way:

$$f_s = \frac{\omega^2 - \omega_s^2 - i\omega\gamma + \omega_s^2 + i\omega\gamma}{\left(\omega^2 - \omega_s^2 + i\omega\gamma\right)} = 1 + \frac{\omega_s^2 - i\omega\gamma}{\left(\omega^2 - \omega_s^2 + i\omega\gamma\right)} \cong 1 + \frac{\omega_s^2}{\left(\omega^2 - \omega_s^2 + i\omega\gamma\right)}. \qquad (1.13)$$

The last term follows from the fact that γ is usually much lower than ω_s. From eq. 1.13 the dispersion correction $\chi(\omega)$ (also known as dieletric susceptibility) can be written as

$$\chi(\omega) = f_s' + i f_s'' = \frac{\omega_s^2}{\left(\omega^2 - \omega_s^2 + i\omega\gamma\right)}, \qquad (1.14)$$

with real and imaginary parts given by

$$f_s' = \frac{\omega_s^2\left(\omega^2 - \omega_s^2\right)}{\left(\omega^2 - \omega_s^2\right)^2 + (\omega\gamma)^2} \qquad \text{and} \qquad f_s'' = \frac{\omega_s^2\omega\gamma}{\left(\omega^2 - \omega_s^2\right)^2 + (\omega\gamma)^2}. \qquad (1.15)$$

These dispersion corrections for the single oscillator model are shown in fig. 1.5 with ω_s=0.1 [Jackson99].

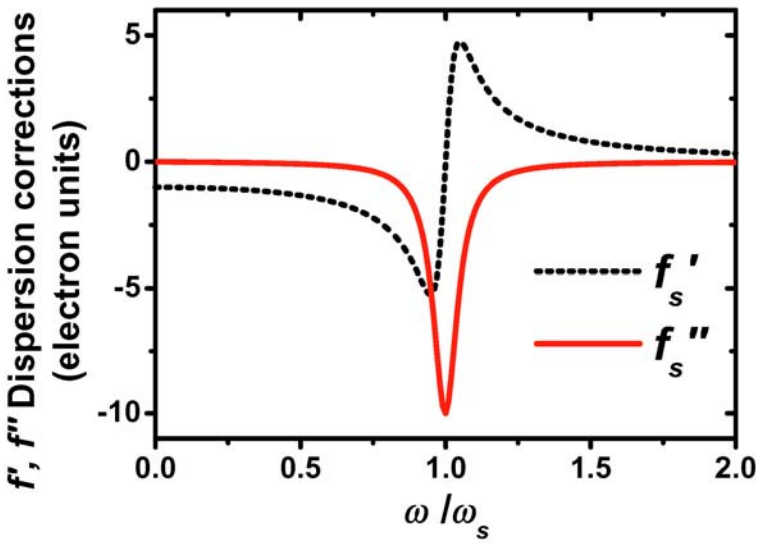

Fig. 1.5 – Real f_s' and imaginary f_s'' parts of the dispersion corrections as a function of the ratio between the driving frequency ω and the resonant frequency ω_s.

In order to calculate the dispertion corrections for a real atom one must consider electron-electron interaction that can only be described using the quantum mechanics

formalism. This theoretical description is usually based on self-consistent equations that describes an atom as a multi-electron system and will not be presented here.

The theoretical values of $\chi(\omega)$ can be obtained only with a very precise knowledge of ω_s and γ (there is no straightforward way to measure γ). However, the casuality principle of electrodynamics can be employed to derive relations between real and imaginary parts of $\chi(\omega)$. These relations are known as the Kramers-Kronig dispertion relations. Since *f'* and *f''* are the real and imaginary parts of $\chi(\omega)$ these relations can be written as [Jackson99]:

$$f'(\omega) = \int_0^\infty \frac{\omega' f''(\omega')}{\omega'^2 - \omega^2} d\omega' \qquad \text{and} \qquad f''(\omega) = -\int_0^\infty \frac{f'(\omega')}{\omega'^2 - \omega^2} d\omega' . \qquad (1.16)$$

The first equation can be used to estimate *f'* if *f''* is known from near-edge absorption measurements. However, the integrals of equation 1.16 requires measurements from $\omega = 0$ until $\omega = \infty$ that are not feasible. Alternatively, it is possible to use tabulated values of *f''* based on self-consistent theoretical calculations for multi-electron systems. These values, which exist in a wide frequency range, can be combined with high resolution frequency measurements close to the atomic absorption edges.

A program to perform the integration of the first equation 1.16 was made by Dr. Tobias Schülli and is available on internet (http://www.schuelli.com/physics/kkpage.html). To use this computer routine one must measure the x-ray absorption at the vicinity of the absorption edge of interest. This is usually done by scanning the x-ray energy of the incident beam while it is pointed out to a sample that contains the atomic specie of interest. Tabulated values of *f''* are replaced by the re-normaized experimental intensity in the energy range which was measured and used as input to calculate *f'*. Fig. 1.6(a) shows theoretical values for *f'* and *f''* close to the Ge-K edge (E = 11103.1 eV). The set of measured absorption data is pasted on top of the *f''* values – fig. 1.6(b) – and the experimental *f'* is obtained. Electron units are generally used for *f*.

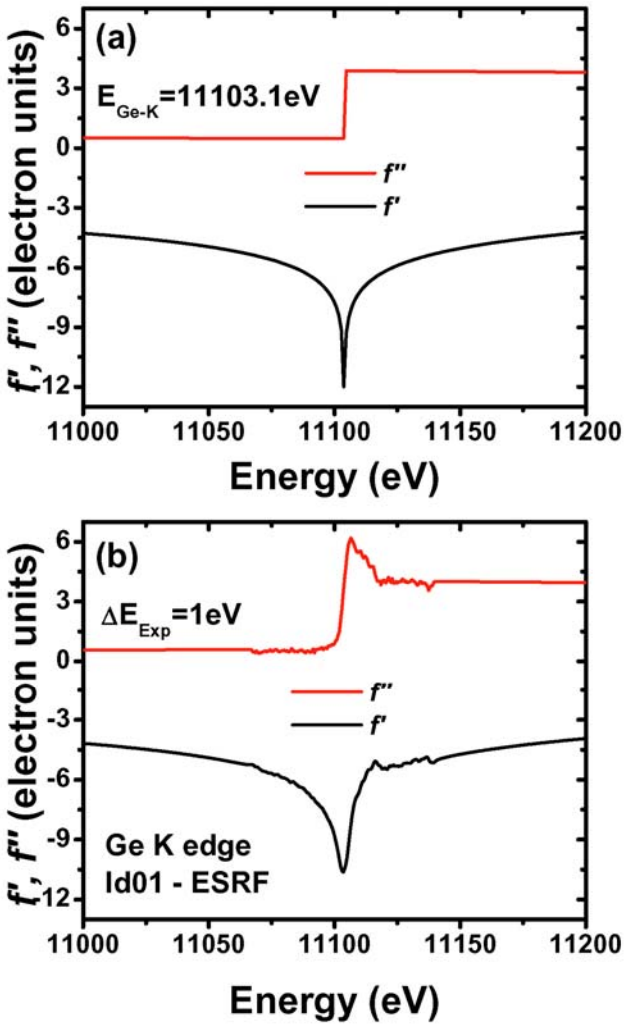

Fig. 1.6 – (a) Theoretical and (b) measured values for f" close to te Ge K absorption edge. Values of f' are obtained by the first equation (1.16). The Id01 Si (111) monochromator used here has 1eV energy resolution. These corrections change the non-resonant Ge atomic form factor shown in fig. 1.4(c).

The scattering factor of an atom is, then, given by [AlsNielsen01, Warren69]:

$$f = f_0(\mathrm{Q}) + f'(E) + f''(E), \tag{1.17}$$

where the photon energy E replaces the frequency dependence of f' and f''. The first term, given by eq. 1.4, is proportional to the number of electrons of an atom and decreases for high momentum transfer Q (higher scattering angles). By tuning the x-ray photon energy one can change the values of f' and f'' and perform chemically sensitive experiments. Both Q and energy dependence effects were recentlly explored by Schülli et. al. [Schulli03a] to enhance the chemical contrast at high momentum transfer reflections.

1.3 Form factor of a small crystal

In section 1.2.1 the atomic form factor was calculated assuming a spherical electron cloud surrounding the atom. For a general case, an object with arbitrary shape and homogeneous charge density ρ will have a form factor S_{obj} given by the integral

$$S_{obj} = \int \rho\,\theta(\mathbf{r}) e^{i\mathbf{q}\cdot\mathbf{r}} d\mathbf{r}\,, \tag{1.18}$$

where $\theta(\mathbf{r})$ is a step function which has value 1 inside the object. The general form of equation 1.18 holds for any continuous charge distribution.

A crystal can be imagined as a regularly repeated atomic arrangement and form factors for the most simple crystal shapes can be calculated analytically[1]. All objects studied in this work can be seen as stacks of 2D crystal layers. If the object has a four-fold symmetry, the form factor can be calculated as a stack of square crystals. A square with N^2 atoms with sides oriented along the q_a and q_r direction and lattice parameter d will scatter with intensity given by[2]:

$$I = \frac{I_0}{N^4}\left|\left(\int e^{i\mathbf{q}_\mathbf{r}\cdot\mathbf{x}}\sigma(x)dx \cdot \int e^{i\mathbf{q}_\mathbf{r}\cdot\mathbf{y}}\sigma(y)dy\right)\right|^2. \tag{1.19}$$

The atomic positions are denoted as $\sigma(x) = \sum_{j=0}^{N-1} f\,\delta(x - jd)$ and $\sigma(y) = \sum_{g=0}^{N-1} f\,\delta(y - gd)$ and the atomic scattering factor of each atom is given by f. Hence, using $f = 1$ for simplicity, the scattered intensity of one square-shaped atomic layer can be written as

$$\begin{aligned} I &= \frac{I_0}{N^4}\left|\left(\sum_{j=0}^{N-1}\int_{-\infty}^{\infty} e^{i\mathbf{q}_\mathbf{r}\cdot\mathbf{x}}\delta(x - jd)dx \cdot \sum_{g=0}^{N-1}\int_{-\infty}^{\infty} e^{i\mathbf{q}_\mathbf{a}\cdot\mathbf{y}}\delta(y - gd)dy\right)\right|^2 \\ \Rightarrow I &= \frac{I_0}{N^4}\left|\left(\sum_{j=0}^{N-1}\left(e^{iq_r d}\right)^j \cdot \sum_{g=0}^{N-1}\left(e^{iq_a d}\right)^g\right)\right|^2 \end{aligned}. \tag{1.20}$$

The summations of the last equation have the form of geometric progressions for which the sum is given by $S = a + ar + ar^2 + \ldots + l = (rl - a)/(r - l)$, where a is the first term, l is the last term and r is the ratio. The intensity scattered by the 2D square layer is [Warren69]

[1] In this section we assume a simple cubic crystal symmetry.
[2] The intensity equations of the form factors calculated in this thesis are normalized by the intensity I_0, that is defined as $I_0 \equiv I(q=0)$.

$$I = \frac{I_0}{N^4}\left|\frac{e^{iq_r Nd}-1}{e^{iq_r d}-1}\cdot\frac{e^{iq_a Nd}-1}{e^{iq_a d}-1}\right|^2 . \tag{1.21}$$

To obtain the scattering of an island that consists of a stack of square layers one must sum over the contributions of layers with different side lengths $L = Nd$ and/or lattice parameters d. The result for the complete structure is obtained performing a sum over the heights h_j of the atomic layers with respect to the substrate [Malachias01]

$$I(q_a, q_r, q_z) = \frac{I_0}{N^4 M^2}\left|\sum_{j=1}^{M}\frac{e^{iL_j q_a}-1}{idq_a}\cdot\frac{e^{iN_j d_j q_r}-1}{e^{id_j q_r}-1}e^{iq_z h_j}\right|^2 . \tag{1.22}$$

For fixed q_r and q_z eq. 1.22 can be simplified into [Warren69]

$$I(q_a) = \frac{I_0}{L^2}\left|\frac{\sin\left(L/2\, q_a\right)}{\sin(q_a)}\right|^2 . \tag{1.23}$$

The form factor of a disc with constant charge density is very useful for structures with radial symmetry. In this case S_{disc} is given by the integral in cylindrical coordinates [Kegel99]

$$S_{disc}(\mathbf{q}) = \int_0^R\int_0^{2\pi} e^{i\mathbf{q}\cdot\mathbf{r}} r d\varphi d\mathbf{r} = \int_0^R\int_0^{2\pi} e^{iq_r r\cos\varphi} r d\varphi dr . \tag{1.24}$$

Similarly to eq. 1.22 a stack of discs will scatter with intensity given by

$$I(q_a, q_r, q_z) = \frac{I_0}{M^2\pi^2 R^4}\left|\sum_{j=1}^{M}\left[\int_0^R\int_0^{2\pi} e^{iq_r r\cos\varphi} r d\varphi dr\right]e^{iq_z h_j}\right|^2 . \tag{1.25}$$

1.4 Structure factor

The scattering of crystals with simple geometries can be understood by the results of the preceding sections. However, the scattered intensity for a real crystal depends on the symmetry of the atoms inside the crystal unit cells and is proportional to the structure factor F. Atomic positions are represented by the vector $\mathbf{r_n} = x_n\mathbf{a_1} + y_n\mathbf{a_2} + z_n\mathbf{a_3}$.

We are interested in the value of F for an *hkl*-reflection when the Bragg's law is satisfied for a set of atomic planes. In reciprocal space this means that $(\mathbf{q_0}/\lambda)=\mathbf{H}_{hkl}$. The

vector $\mathbf{H}_{hkl}$ is given by $\mathbf{H}_{hkl} = h\mathbf{b_1} + k\mathbf{b_2} + l\mathbf{b_3}$ in terms of the reciprocal vectors $\mathbf{b_1}\,\mathbf{b_2}\,\mathbf{b_3}$. The structure factor for a Bragg reflection is [Warren69]

$$\mathrm{F}_{hkl} = \sum_n f_n e^{(2\pi i/\lambda)(\mathbf{q_0}\cdot\mathbf{r_n})} = \sum_n f_n e^{2\pi i(h\mathbf{b_1}+k\mathbf{b_2}+l\mathbf{b_3})(x_n\mathbf{a_1}+y_n\mathbf{a_2}+z_n\mathbf{a_3})} = \sum_n f_n e^{2\pi i(hx_n+ky_n+lz_n)} \quad (1.26)$$

If F = 0 for a given *hkl* reflection no scattered intensity of this reflection is also zero.

All materials studied in this work have diamond-like unit cells. It is easier to obtain the diamond structure factor starting from a face-centered (FCC) cubic lattice. The basis of a FCC unit cell consists of four atoms located in the coordinates (x_n, y_n, z_n), (x_n+½, y_n+½, z_n), (x_n+½, y_n, z_n+½) and (x_n, y_n+½, z_n+½). Each unit cell with n atoms has (n/4) atomic groups that scatter with the same structure factor. Performing a sum over a 4-atoms group leads to

$$\mathrm{F}_{hkl} = \left[1 + e^{\pi i(h+k)} + e^{\pi i(h+l)} + e^{\pi i(k+l)}\right] \sum_{n/4} f_n e^{2\pi i(hx_n+ky_n+lz_n)} . \quad (1.27)$$

If m is an integer, $e^{\pi i m} = (-1)^m$, and hence the first factor takes the value 4 if *hkl* are all odd or all even and the value zero if *hkl* are mixed. Hence,

$$\mathrm{F}_{hkl} = 4\sum_{n/4} f_n e^{2\pi i(hx_n+ky_n+lz_n)} \quad (hkl) \text{ unmixed} \qquad \text{and} \qquad \mathrm{F}_{hkl} = 0 \quad (hkl) \text{ mixed.} \quad (1.28)$$

The diamond (Si or Ge) structure, shown in fig. 1.7, consists of two FCC lattices shifted by ¼ in all directions. The Si (Ge) atoms in these two sub-lattices are located in the coordinates

$$\mathrm{Si}_{(1)} \rightarrow \begin{matrix} 0 & 0 & 0 \\ ½ & ½ & 0 \\ ½ & 0 & ½ \\ 0 & ½ & ½ \end{matrix} \qquad \mathrm{Si}_{(2)} \rightarrow \begin{matrix} ¼ & ¼ & ¼ \\ ¾ & ¾ & ¼ \\ ¾ & ¼ & ¾ \\ ¼ & ¾ & ¾ \end{matrix} .$$

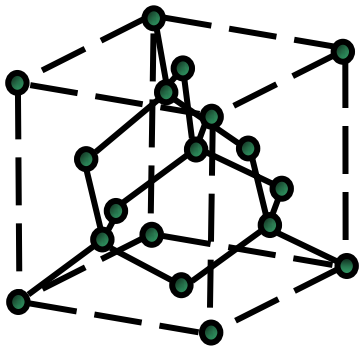

Fig. 1.7 – Diamond (Si or Ge) unit cell.

Using the first equation 1.28 with the positions 0 0 0 for the $Si_{(1)}$ sub-lattice and ¼ ¼ ¼ for $Si_{(2)}$ the structure factor can be written as

$$F_{hkl} = 4\left[f_{Si} + f_{Si}e^{(\pi i/2)(h+k+l)}\right], \qquad \text{for } (hkl) \text{ unmixed.} \tag{1.29}$$

Since the scattered intensity is proportional to the square of the structure factor, i.e., $I \propto F^2_{hkl} = F_{hkl}F^*_{hkl}$, then:

$$\begin{aligned} F^2_{hkl} &= 16\left[f_{Si} + f_{Si}e^{(\pi i/2)(h+k+l)}\right]\cdot\left[f_{Si} + f_{Si}e^{-(\pi i/2)(h+k+l)}\right] \\ &= 16\left[2f^2_{Si} + 2f^2_{Si}\cos\frac{\pi}{2}(h+k+l)\right] \end{aligned} \quad . \tag{1.30}$$

Table 1 shows the scattered intensities of a Si (diamond) structure for different reflections (*n* is an integer number).

Reflection	Intensity
$h+k+l = 4n$	$F_{hkl}^2 = 16(2f_{Si})^2$
hkl odd	$F_{hkl}^2 = 16(2f_{Si}^2)$
hkl mixed	$F_{hkl}^2 = 0$
$h+k+l = (2n+1)2$	$F_{hkl}^2 = 0$

Table 1 – Structure factors of a Si crystal for different reflections.

Key examples of the reflections of the first type are (2 2 0), (4 0 0) and (6 2 0). The second type of reflection includes (1 1 1), (3 3 3) and (3 1 5). Reflections with mixed index are known as lattice-forbidden since the primary lattice (in this case FCC) determines their null structure factor. Reflections of the fourth kind ($h+k+l = 4n+2$) are called basis-forbidden due to their dependence on the sub-lattice (or basis).

In the case where a second type of atom (Ge) is introduced in the Si lattice different reflections can appear. For instance, a Si-Ge zincblend structure as shown in fig. 1.8. Two sub-lattices with Si and Ge atoms located in the following positions:

$$\text{Si} \rightarrow \begin{matrix} 0 & 0 & 0 \\ ½ & ½ & 0 \\ ½ & 0 & ½ \\ 0 & ½ & ½ \end{matrix} \qquad \text{Ge} \rightarrow \begin{matrix} ¼ & ¼ & ¼ \\ ¾ & ¾ & ¼ \\ ¾ & ¼ & ¾ \\ ¼ & ¾ & ¾ \end{matrix}$$

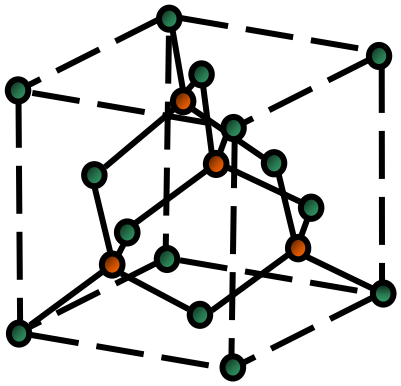

Fig. 1.8 – SiGe zincblend (pseudodiamond) unit cell. Si atoms are represented in green while Ge atoms appear in orange.

The fourth kind of reflection of table 1 presents a non-zero structure factor for the zincblend ordered configuration. The new value of F^2 will be given by [Warren69]

$$F_{hkl}^2 = 16(f_{Ge} - f_{Si})^2 \qquad \text{for} \qquad h+k+l = (2n+1)2. \tag{1.31}$$

This kind of reflection that depends on the possibility of ordering of the alloy is known as superstructure reflection. An ordered alloy consists of sub-units that are periodic along the crystal. The arrangement of alternate Si and Ge atoms in the [1 0 0] direction (such as …Si-Ge-Si-Ge-Si-Ge-Si…) will give rise to a (2 0 0) reflection. If the repetition unit consists of four atoms with the arrangement (…Si-Si-Si-Ge-Si-Si-Si-Ge-Si-Si-Si-Ge...) the (1 0 0) reflection should be measured as a superstructure reflection.

1.4.1 Long-range order and order parameter S

Considering a binary crystal with two kinds of atoms – Si and Ge – the ordered structure has two kinds of positions which will be designated α and γ. For a completely ordered alloy with ideal stoichiometric composition the α-sites are all occupied by Ge atoms and the γ-sites by Si atoms. In this case the sample composition is the sum of the atom fractions $n_{Ge} + n_{Si} = 1$. The same relation can be written to the fractions of α and γ sites $m_\alpha + m_\gamma = 1$.

Some useful parameters for the site occupancies can be defined. Let us call r_α and r_γ the fraction of α-sites and γ-sites occupied by the right atoms. In the other hand w_α and w_γ are the fraction of α and γ sites occupied by the wrong atom [Warren69]. These parameters are related by $r_\alpha + w_\alpha = 1$ and $r_\gamma + w_\gamma = 1$. There is also an additional condition that the fraction of sites occupied by Si atoms must be equal to the fraction of Si atoms (the same is valid for Ge). This can be expressed by:

$$m_\alpha r_\alpha + m_\gamma w_\gamma = n_{Ge} \quad , \quad m_\gamma r_\gamma + m_\alpha w_\alpha = n_{Si}. \tag{1.32}$$

A convenient notation for nonstoichiometric compositions is the Bragg and Williams order parameter S. The definition of S has to be linearly proportional to $(r_\alpha + r_\gamma)$ with S = 0 for a completely random arrangement and S = 1 for $r_\alpha = r_\gamma = 1$ and stoichiometric compotision. Expressing the linear dependence by $S = a + b(r_\alpha + r_\gamma)$, the first condition (S = 0) gives 0 = a + b since a random alloy has half of its α and γ atoms in the right sites and half in wrong sites. The second condition (S = 1) gives 1 = a + 2b since all atoms are in their right sites. Eliminating the constants a and b the long-range order parameter is expressed as [Warren69]:

$$S = r_\alpha + r_\gamma - 1 = r_\alpha - w_\gamma = r_\gamma - w_\alpha. \tag{1.33}$$

With this definition for S the structure factors F for the superstructure reflections are proportional to S and hence a general parameter S^2 is obtained from the experiment. The structure factor for a partially ordered alloy can be obtained by summing over all atomic positions in the unit cell. Since there are two different kinds of atomic sites (α and γ) the total sum of eq. 1.26 can be divided into a sum over the α positions and a sum over the γ positions using the average scattering factor of each kind of site:

$$F = \sum_\alpha \left(r_\alpha f_{Ge} + w_\alpha f_{Si}\right) e^{2\pi i(hx_n + ky_n + lz_n)} + \sum_\gamma \left(r_\gamma f_{Si} + w_\gamma f_{Ge}\right) e^{2\pi i(hx_n + ky_n + lz_n)} \tag{1.34}$$

For the case of the pseudodiamond structure of fig. 1.8 the positions of Ge and Si atoms are (¼¼¼) and (000), respectively. Using these positions in eq. 1.34 leads to

$$
\begin{aligned}
F &= \left(\mathrm{r}_\alpha f_{Ge} + \mathrm{w}_\alpha f_{Si}\right) e^{\frac{\pi i}{2}(h+k+l)} + \left(\mathrm{r}_\gamma f_{Si} + \mathrm{w}_\gamma f_{Ge}\right) \\
&= f_{Si}\left\{\mathrm{r}_\gamma + \mathrm{w}_\alpha e^{\frac{\pi i}{2}(h+k+l)}\right\} + f_{Ge}\left\{\mathrm{r}_\alpha + \mathrm{w}_\gamma e^{\frac{\pi i}{2}(h+k+l)}\right\} \\
&= f_{Si}\left\{\mathrm{r}_\gamma + \mathrm{w}_\alpha\left[cos\left(\frac{\pi}{2}\cdot(h+k+l)\right) + isin\left(\frac{\pi}{2}\cdot(h+k+l)\right)\right]\right\} \\
&\quad + f_{Ge}\left\{\mathrm{r}_\alpha\left[cos\left(\frac{\pi}{2}\cdot(h+k+l)\right) + isin\left(\frac{\pi}{2}\cdot(h+k+l)\right)\right] + \mathrm{w}_\gamma\right\}
\end{aligned}
\quad . \qquad (1.35)
$$

The structure factor of the allowed reflection (400) will be given by

$$F_{(400)} = f_{Si}\ \{\mathrm{r}_\gamma + \mathrm{w}_\alpha\} + f_{Ge}\ \{\mathrm{r}_\alpha + \mathrm{w}_\gamma\} = 2(f_{Si}\mathrm{n}_{\mathrm{Si}} + f_{Ge}\mathrm{n}_{\mathrm{Ge}}); \qquad (1.36)$$

where the fraction of α-sites and γ-sites in eq. 1.32 are $\mathrm{m}_\alpha = ½$ and $\mathrm{m}_\gamma = ½$.

For the (200) superstructure reflection the structure factor of eq. 1.31 is re-calculated as

$$F_{(200)} = f_{Si}\ \{\mathrm{r}_\gamma - \mathrm{w}_\alpha\} + f_{Ge}\ \{-\mathrm{r}_\alpha + \mathrm{w}_\gamma\} = \mathrm{S}(f_{Si} - f_{Ge}), \qquad (1.37)$$

Where S was obtained using eq. 1.33.

Then, the integrated intensity of the (200) reflection is proportional to

$$\mathrm{I}_{(200)} = \mathrm{c}\mathrm{V}_{200}\mathrm{S}^2(f_{Ge} - f_{Si})^2, \qquad (1.38)$$

where V_{200} is the volume of the region at the bragg condition and all scattering constants are represented by c. The integrated intensity of the (400) reflection can be written as

$$\mathrm{I}_{(400)} = \mathrm{c}4\mathrm{V}_{400}(f_{Ge}\mathrm{n}_{\mathrm{Ge}} + f_{Si}\mathrm{n}_{\mathrm{Si}})^2, \qquad (1.39)$$

The order parameter S can be experimentally obtained by comparing the ratio of the measured intensities. Assuming that the intensities were measured in a region of reciprocal space with equal volume ($\mathrm{V}_{400} = \mathrm{V}_{200}$) the ratio between intensities will be given by:

$$\frac{\mathrm{I}_{200}}{\mathrm{I}_{400}} = \frac{\mathrm{S}^2\left(f_{Ge} - f_{Si}\right)^2}{4\left(f_{Ge}\mathrm{n}_{Ge} + f_{Si}\mathrm{n}_{Si}\right)^2}. \qquad (1.40)$$

Hence,

$$\mathrm{S} = \sqrt{\frac{\mathrm{I}_{200}}{\mathrm{I}_{400}}}\,\frac{2\left(f_{Ge}\mathrm{n}_{Ge} + f_{Si}\mathrm{n}_{Si}\right)}{\left(f_{Ge} - f_{Si}\right)}. \qquad (1.41)$$

Although the results of eqs. 1.36 – 1.41 were calculated for a zincblend structure they are valid for any system with two kinds of sites and two kinds of atoms with $n_{Ge} = n_{Si} = 0.5$ and $m_{\alpha(Ge)} = m_{\gamma(Si)} = 0.5$.

1.5 Grazing-Incidence Diffraction

In a typical set-up for x-ray diffraction the incident and exit beams are coplanar. According to Bragg's condition, x-rays are reflected from atomic planes with a spacing d when the path length difference of the x-ray wave into the crystal is an integer (n) multiple of the wavelength. This leads to the well-known Bragg's law: $n\lambda = 2d\sin\theta$. In fig. 1.9 a sketch of a coplanar x-ray diffraction geometry is shown, where ω is the incident angle and the diffracted intensity is measured by the detector under an angle 2θ relative to the incident beam. In this geometry the lattice parameter perpendicular to the surface plane can be measured. Since the wave vectors of the incident and scattered beams are given by $|\mathbf{k}_i| = |\mathbf{k}_f| = k = 2\pi/\lambda$ the x-ray momentum transfer in calculated as $\mathbf{Q} = \mathbf{k_f} - \mathbf{k_i}$.

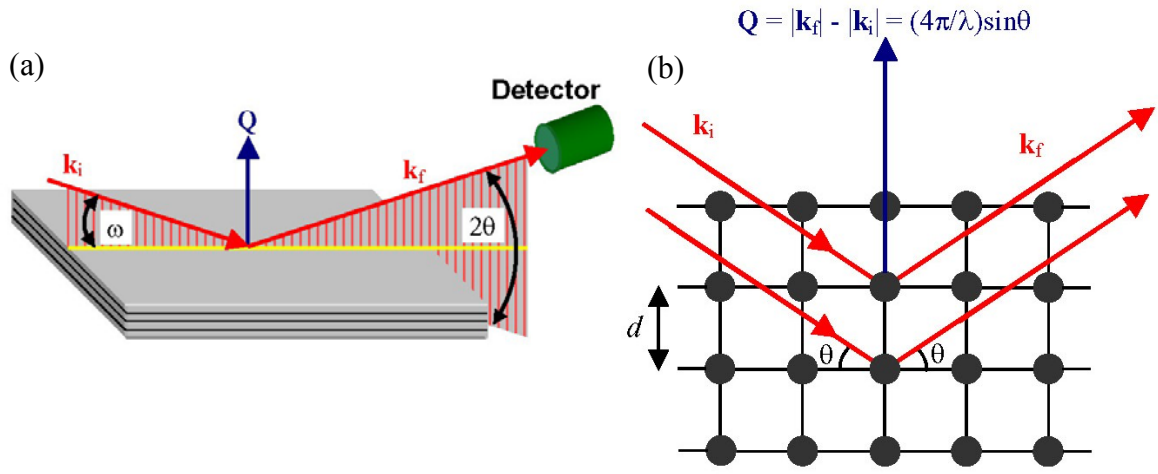

Fig. 1.9 – (a) Geometry used for coplanar x-ray diffraction. (b) Sketch of Bragg's law in reciprocal space. The usual formula $n\lambda = 2d\sin\theta$ can be obtained assuming $|\mathbf{Q}| = n2\pi/d$.

Fig. 1.9(b) shows a sketch of Bragg's law in a coplanar symmetric geometry where the incident and exit angle with respect to the crystal surface are the same.

If one needs to use x-rays as a surface sensitive probe a non-coplanar geometry must be employed. The technique that combines surface sensitivity and diffraction from crystal planes perpendicular to the sample surface is known as Grazing-Incidence Diffraction (GID). It profits from the total external reflection of x-rays at low incident angles [Dosch92].

The refractive index of x-rays is generally described by $n = 1 - \delta + i\beta$, where δ is the dispersion correction constant and β is the absorption correction [Vineyard82, Dosch92]. For typical wavelengths and common solid materials these constants have values of the order of 10^{-5}, generating a refractive index slightly smaller than 1.

Fig. 1.10 shows schematically Snell's law that relates the incident grazing angle α_i to the refracted and reflected grazing angles α_r and α_f. Since the refraction index outside the solid is equals to unity the following relationship is valid (here we neglect the constant β):

$$(1 - \delta)\, sin(\pi/2 - \alpha_r) = sin(\pi/2 - \alpha_f) = sin(\pi/2 - \alpha_i). \qquad (1.42)$$

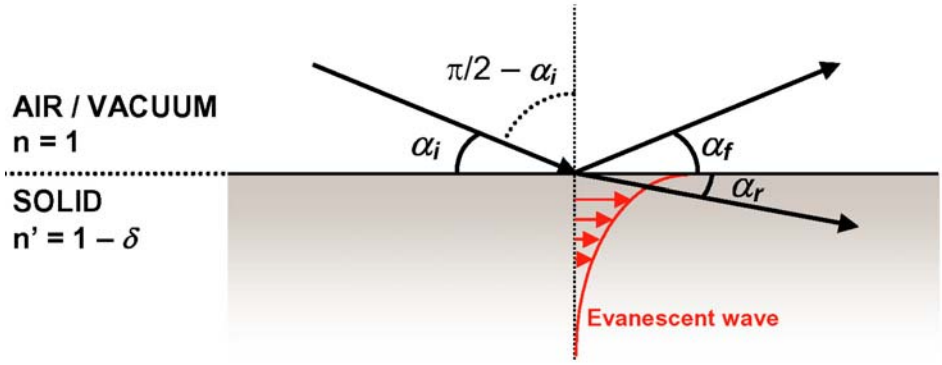

Fig. 1.10 – Representation of Snell's law for x-ray reflection/refraction in solids.

Eq. 1.42 can be re-written as

$$(1 - \delta)\, cos(\alpha_r) = cos(\alpha_f) = cos(\alpha_i). \qquad (1.43)$$

X-rays undergo total external reflection for $\alpha_r = 0$ that implies $cos(\alpha_r) = 1$. In this case, using eq. 1.43, the incident critical angle α_c is given by

$$(1 - \delta) = cos(\alpha_c) \approx 1 - \alpha_c^2/2. \qquad (1.44)$$

Total external reflection is then observed for incident angles smaller than $\alpha_c = \sqrt{2\delta}$ that corresponds to approximate 0.5° for most of solid materials.

The x-ray refracted wave that propagates across the surface will have the form

$$\mathbf{E} = E_0 e^{i\mathbf{k}\cdot\mathbf{x}} = E_0 e^{i\mathbf{k}\cdot\left(x\cos\alpha_r + z\sin\alpha_r\right)}, \tag{1.45}$$

where x is the direction along the interface and z is the normal direction. From eq. 1.43 one can write $(1-\delta)\cos(\alpha_r) = \cos(\alpha_i)$ and

$$\cos(\alpha_r) = \cos(\alpha_i)/(1-\delta). \tag{1.46}$$

Using $\sin^2(\alpha_r) = 1 - \cos^2(\alpha_r)$ and eq. 1.46 one gets

$$\sin\alpha_r = \sqrt{1-\left(\frac{\cos\alpha_i}{1-\delta}\right)^2} = i\sqrt{\left(\frac{\cos\alpha_i}{1-\delta}\right)^2 - 1}. \tag{1.47}$$

With the results of eq. 1.46 and 1.47, eq. 1.45 becomes

$$\mathbf{E} = E_0 e^{-k\left[1-\left(\frac{\cos\alpha_i}{1-\delta}\right)^2\right]^{\frac{1}{2}} z} e^{ik\left(\frac{\cos\alpha_i}{1-\delta}\right)x}. \tag{1.48}$$

Eq. 1.48 describes an evanescent wave that propagates parallel to the solid surface with an exponencial damping in its amplitude across the interface. In this case the x-ray evanescent wave has a limited penetration depth in the sample. The x-ray penetration depth has the form [Dosch92]:

$$L = \frac{\lambda}{2\pi\cdot l} \tag{1.49}$$

with

$$l = 2^{-1/2}\left\{\left(2\delta - \mathrm{sen}^2\,\alpha_i\right) + \left[\left(\mathrm{sen}^2\,\alpha_i - 2\delta\right)^2 + 4\beta^2\right]^{1/2}\right\}^{1/2}. \tag{1.50}$$

The minimum scattering depth is about 50Å for the asymptotic value $\alpha_i = 0$.

In the experimental setup for GID the sample is illuminated by the x-ray beam at a shallow incident angle α_i ($\alpha_i < \alpha_c$). The crystal is rotated around the surface normally until a particular lattice plane lying perpendicularly to the surface fulfills the Bragg condition. A position sensitive detector (PSD) oriented perpendicular to the sample surface is used to collect all wavevectors $\mathbf{k}_f$ in the vertical (z) direction [Metzger98, Malachias02].

A relative momentum transfer coordinate system (radial-angular) is used for the measurements. The radial momentum transfer $\mathbf{q}_r$ defines the distance from the origin of reciprocal space. The angular momentum transfer $\mathbf{q}_a$ is related the deviation $\Delta\omega$ from the Bragg condition $\omega = 2\theta/2$. $\mathbf{q}_z$ is the vertical momentum transfer, that defines the distance

from the $\mathbf{q_r}$-$\mathbf{q_a}$ plane. A schematic representation of the GID geometry and momentum transfer vectors is shown in fig. 1.11 [Kegel99, Malachias02].

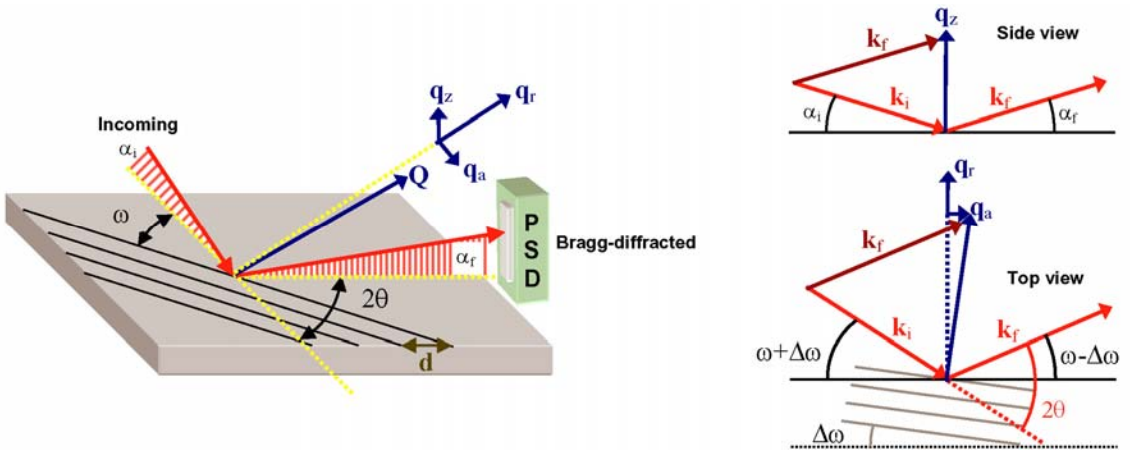

Fig. 1.11 – Grazing-Incidence Diffraction geometry. The x-ray beams are represented in red while the momentum transfer vectors were drawn in blue. The radial ($\mathbf{q}_r$), angular ($\mathbf{q}_a$) and vertical ($\mathbf{q}_z$) components of momentum transfer are shown in detail on the right.

In this case, using $|\mathbf{k}_i| = |\mathbf{k}_f| = k_0 = 2\pi/\lambda$ the momentum transfer components are given by:

$$\begin{aligned} q_r &= 4\pi/\lambda \, sin\left(2\theta/2\right) \\ q_a &= 4\pi/\lambda \, sin\left(2\theta/2\right) sin\Delta\omega \\ q_z &= 2\pi/\lambda \left(sin\alpha_i + sin\alpha_f\right) \end{aligned} \quad . \qquad (1.51)$$

Reciprocal space scans in the directions of these three components have different meanings. Scans in the q_r direction are sensitive to variations in the crystal lattice parameter d (strain). These scans, called *radial scans*, cross the path that points from the reciprocal space origin to the Bragg reflection position. Scanning the angular component q_a one can probe the size and shape of a region with a fixed lattice parameter. The direction of these so called *angular scans* is, by definition, perpendicular to q_r. Finally, scans along q_z can be used to obtain vertical information of the crystalline structure.

Figure 1.12 shows a sketch of the reciprocal space H-K plane and the directions of both radial and angular scans. Experimental examples will be given in chapter 2 with a detailed description.

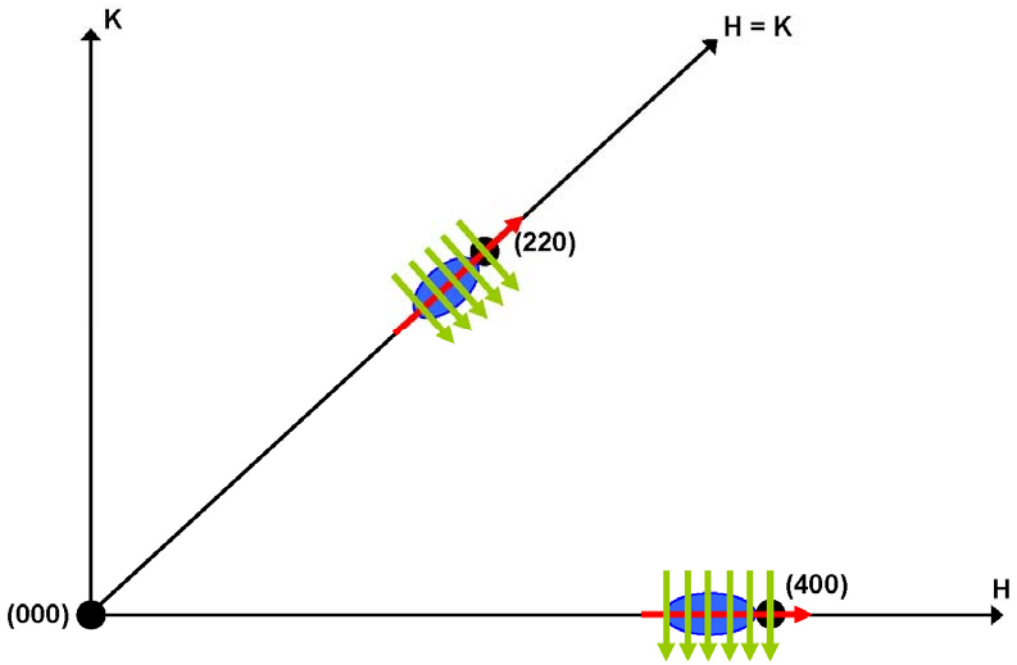

Fig. 1.12 – Schematic representation of radial (q_r) and angular (q_a) scans in the reciprocal space H-K plane. The reciprocal space points of a reference lattice and a strained lattice were represented in black and blue, respectively. Radial scans, represented by red arrows, cross the path along the line that connects a Bragg reflection position to the origin of the reciprocal space. Angular scans, shown in green, are perpendicular to the radial direction.

1.5.1 Distorted-Wave Born Approximation

The propagation of an electromagnetic plane wave in a medium with index of refraction n is described by the homogeneous Helmholtz equation [Jackson99]:

$$\nabla \times \nabla \times E(r) + k^2 n^2 E(r) = 0\,, \tag{1.52}$$

with $k = 2\pi/\lambda$ and $n = 1 - \delta + i\beta$.

In order to model the scattering from a crystal with free-stading islands at the surface one must use the Distorted-Wave Born Approximation (DWBA) [Rauscher99]. In the DWBA the index of refraction (n^2) of equation 1.52 is replaced by $n^2(\mathbf{r}) = n_0^2(z) + (1 - n_{isl}^2)\Theta_{isl}(\mathbf{r})$. The substrate has a refraction index $n_0^2(z)$ equals to unity for $z > 0$ (vacuum) and a constant value n_s for the substrate ($z < 0$). Inside the islands the index of refraction is corrected by the term n_{isl}. $\Theta_{isl}(\mathbf{r})$ is a step function equals to the unity inside islands and zero outside them. Then, equation 1.52 becomes:

$$\nabla \times \nabla \times E(r) + k_0{}^2 n_0{}^2(z) E(r) = -k_0{}^2 \left(1 - n_{isl}{}^2\right) \Theta_{isl}(\mathbf{r}) E(\mathbf{r}) . \qquad (1.53)$$

The solution of equation 1.53 is given by [Rauscher99]

$$E_f = exp\left(i\mathbf{k}_{||} \cdot \mathbf{r}_{||}\right) \cdot \left[exp\left(ik_z \cdot r_z\right) + R_F \, exp\left(-ik_z \cdot r_z\right)\right] \quad (z > 0) \qquad (1.54)$$

for the reflected/incident wave and

$$E_f = exp\left(i\mathbf{k}_{||} \cdot \mathbf{r}_{||}\right) \cdot \left[T_F \, exp\left(i\tilde{k}_z \cdot r_z\right)\right] \qquad (z < 0) \qquad (1.55)$$

for the transmitted wave. R_F and T_F are the Fresnel reflectivity and transmission coefficients, respectively. The wave vector vertical component (for z < 0) inside the substrate (where the index of refraction is n_s) is represented by $\tilde{k}_z$. The wave vector breaks down into its components $\mathbf{k}_{||}$ and k_z, parallel and perpendicular to the surface.

The scattered wave amplitude is obtained treating the islands as a first order perturbation [Rauscher99]

$$E_{sct}(\mathbf{r}) = -k_0^2 (1 - n_{isl}{}^2) \frac{e^{i\mathbf{k}\cdot\mathbf{r}}}{4\pi r} \int_{z \geq 0} E_0(\mathbf{r}', -\mathbf{k}_f) \Theta_{isl}(\mathbf{r}') E_0(\mathbf{r}', \mathbf{k}_i) d^3 r' . \qquad (1.56)$$

Since the scattering comes solely from the islands (z > 0) E_0 can be replaced by equation 1.54. This equation has two terms: the first is related to the scattered eletric field and the second to the reflected part of the outgoing wave.

The scattered amplitude can be understood as a sum of integrals over all islands, with the form

$$\tilde{\Theta}_{isl}\left(\mathbf{r}_{\|}, \pm k_z^i \pm k_z^f\right) = \int d^3 r' e^{-i\mathbf{q}_{\|}\cdot\mathbf{r}_{\|} - i\left(\pm k_z^i \pm k_z^f\right) z} \Theta_{isl}(\mathbf{r}') , \qquad (1.57)$$

where $\tilde{\Theta}_{isl}$ is the Fourier transform of Θ_{isl}. Each sign combination of the scattered (k^f) and incident (k^i) wave vectors can be associated to a different scattering process according to fig. 1.13. Writing eq. 1.56 as functions of Fourier transforms of eq. 1.57 the scattered amplitude [Rauscher99, Kegel01]

$$E_{sct}(\mathbf{r}) = -k_0^2 (1 - n_{isl}{}^2) \frac{e^{i\vec{k}\cdot\vec{r}}}{4\pi r} \left[\tilde{\Theta}_{isl}\left(\mathbf{q}_{||}, q_z\right) + R_f \tilde{\Theta}_{isl}\left(\mathbf{q}_{||}, -p_z\right) + R_i \tilde{\Theta}_{isl}\left(\mathbf{q}_{||}, p_z\right) + R_i R_f \tilde{\Theta}_{isl}\left(\mathbf{q}_{||}, q_z\right)\right] , \qquad (1.58)$$

with $p_z = k_z^f + k_z^i$. R_f and R_i are the reflectivities of the incident and scattered waves, respectively. Each term of eq. 1.66 is related to one of the scattering processes shown below.

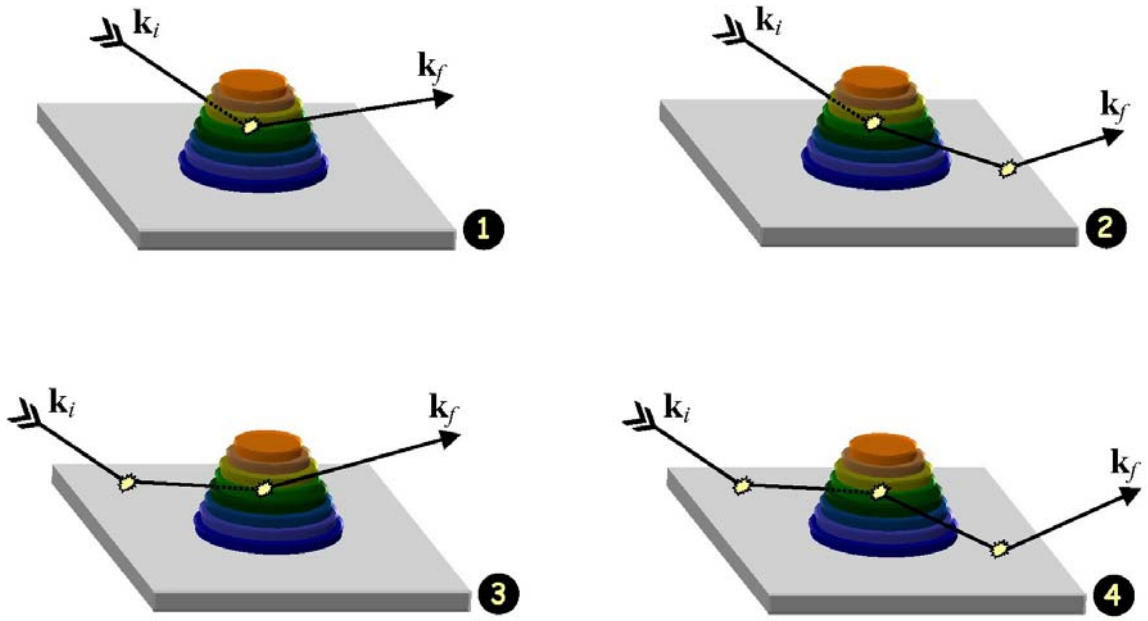

Fig. 1.13 – Four scattering processes according to equation 1.66. Process 1 is a direct scattering from an island. Process 2 includes a substrate reflection after scattering. In (3) the beam is reflected by the substrate and then scattered by the island. Process 4 combines two reflections with one scattering event.

The differential cross section is then given by [Rauscher99]

$$\frac{d\sigma}{d\Omega} = r^2 \left|E_{sct}\right|^2 = \frac{k_0^4 \left|1 - n_{isl}^2\right|^2}{(4\pi)^2} \left|S\left(\mathbf{q}_{||}, k_z^i, k_z^f\right)\right|^2, \tag{1.59}$$

where S is the form factor of the four scattering events

$$S\left(\mathbf{q}_{||}, k_z^i, k_z^f\right) = \left[\widetilde{\Theta}_{isl}\left(\mathbf{q}_{||}, q_z\right) + R_f \widetilde{\Theta}_{isl}\left(\mathbf{q}_{||}, -p_z\right) + R_i \widetilde{\Theta}_{isl}\left(\mathbf{q}_{||}, p_z\right) + R_i R_f \widetilde{\Theta}_{isl}\left(\mathbf{q}_{||}, q_z\right)\right]. \tag{1.60}$$

The scattered intensity ($I_{sct} \propto S^* S$) is obtained by integrating the cross section of eq. 1.59 in the solid angle $\Delta\Omega$ defined by the detector [AlsNielsen01]

$$I_{sct} = \phi \frac{k_0^4 \left|1 - n_{isl}^{\ 2}\right|^2}{(4\pi)^2} \int_{\Delta\Omega} \left|S\left(\mathbf{q}_{||}, k_z^i, k_z^f\right)\right|^2 d\Omega, \tag{1.61}$$

where ϕ is the photon flux defined by $\phi = I/A$. I is the intensity of the incident x-ray beam and A is the sample area. The definitions of cross section and scattered intensity used here hold for the case of a sample that is smaller than the incident beam.

Therefore, x-ray scattering from free-standing islands can be modeled by four different Fourier transforms of the islands. In principle, the ideal situation is when the last 3 terms are not as important as the first one. In this case, the internal structure of these islands can be modeled by a single Fourier transform and the analysis of the data is considerably simpler. This can be obtained by tuning the incident and exit angles such that R_i and R_f are much smaller than one (using α_i close to α_c). The determination of the island shape and composition becomes reasonably straightforward by modeling the structure and form factors.

Chapter 2

Self-assembled Ge islands on Si(001)

2.1 Elastic properties of cubic crystals

2.1.1 Strain

The crystal lattice can be distorted due to externally imposed constraints on the dimensions of the crystalline unit cell. These constraints arise because unit cells with an "ideal" size are embedded in a macroscopic lattice which has its own (and different) average unit cell dimension. Conceptually the externally imposed distortions can be decomposed into a volumetric and a distortional component [Landau59].

The volumetric component comes when alloys are grown in bulk form, when epitaxial films are grown on a lattice-matched substrate or when a hydrostatic pressure is applied to a crystal. The distortional component comes about when epitaxial films are coherently grown on a lattice-mismatched substrate. Suppose, for example, that the substrate is a single unstrained $Si_{1-x}Ge_x$ alloy crystal (bulk) whose Ge composition is x and whose mean lattice parameter $a_{SiGe(sub)}$ is a weighted average (Vegard's law) of the two endpoint lattice parameters, $a_{SiGe(sub)} = (1-x)a_{Si} + xa_{Ge}$.

If an epitaxial $Si_{1-y}Ge_y$ film is grown on top of the $Si_{1-x}Ge_x$ substrate then its lattice parameter parallel to the interface must be the same of that of the substrate, independent of

the Ge composition y of the epitaxial film. This means that $a_{SiGe(epi)\|} = a_{SiGe(sub)} = (1 - x)a_{Si} + xa_{Ge}$.

There will be a parallel strain $\varepsilon_{(epi)\|}$ in the film given by [Tsao93]:

$$\varepsilon_{(epi)\|} = 2(a_{(epi)\|} - a_{(epi)\text{unstr}})/(a_{(epi)\|} + a_{(epi)\text{unstr}}), \tag{2.1}$$

where $a_{(epi)\text{unstr}} = (1 - y)a_{Si} + ya_{Ge}$ is the equilibrium (unstrained) lattice parameter of the epitaxial film.

However, the lattice parameter perpendicular to the interface will change to approximately keep the unit cell volume constant. If the film is locked to a substrate with smaller parallel lattice parameter, the vertical dimension of the epitaxial film unit cell will increase; if the substrate parallel lattice parameter is larger, the vertical dimension of the unit cell of the epitaxial film will decrease.

A quantitative description of the volumetric and distortional components of externally imposed strains can be done writing the generalized Hooke's law for cubic crystals [Landau59, Tsao93]:

$$\begin{pmatrix} \sigma_x \\ \sigma_y \\ \sigma_z \\ \tau_{xy} \\ \tau_{yz} \\ \tau_{zx} \end{pmatrix} = \begin{pmatrix} C_{11} & C_{12} & C_{12} & 0 & 0 & 0 \\ C_{12} & C_{11} & C_{12} & 0 & 0 & 0 \\ C_{12} & C_{12} & C_{11} & 0 & 0 & 0 \\ 0 & 0 & 0 & C_{44} & 0 & 0 \\ 0 & 0 & 0 & 0 & C_{44} & 0 \\ 0 & 0 & 0 & 0 & 0 & C_{44} \end{pmatrix} \begin{pmatrix} \varepsilon_x \\ \varepsilon_y \\ \varepsilon_z \\ \gamma_{xy} \\ \gamma_{yz} \\ \gamma_{zx} \end{pmatrix}, \tag{2.2}$$

where the ε_i's and σ_i's are the normal strains and stresses and the γ_i's and τ_i's are the shear strains and stresses, respectively.

For an epitaxial film and substrate that are oriented along the <100> cubic symmetry directions eq. 2.2 is reduced to

$$\begin{pmatrix} \sigma_{epi\|} \\ \sigma_{epi\perp} \end{pmatrix} = \begin{pmatrix} C_{11} + C_{12} & C_{12} \\ 2C_{12} & C_{11} \end{pmatrix} \begin{pmatrix} \varepsilon_{epi\|} \\ \varepsilon_{epi\perp} \end{pmatrix}. \tag{2.3}$$

In the case of an epitaxial film with a free surface (e.g. uncapped films and/or islands) the perpendicular stress vanishes, hence

$$\sigma_{epi\perp} = 2C_{12}\varepsilon_{epi\|} + C_{11}\varepsilon_{epi\perp} = 0. \tag{2.4}$$

The perpendicular strain and lattice parameter of the film will be given, respectively, by:

$$\varepsilon_{epi\perp} = \frac{-2C_{12}}{C_{11}}\varepsilon_{epi||} = \frac{-2\nu}{1-\nu}\varepsilon_{epi||} \tag{2.5}$$

$$\text{and } a_{epi\perp} = a_{(epi)unstr}\frac{1+\varepsilon_{epi\perp}/2}{1-\varepsilon_{epi\perp}/2}. \tag{2.6}$$

In eq. 2.5 ν is the Poisson's ratio, defined as the negative of the ratio between lateral and longitudinal strain constants under uniaxial longitudinal stress ($\nu = C_{12}/[C_{11}+C_{12}]$) [LandoltBornstein82]. The term that multiplies $\varepsilon_{epi||}$ in eq. 2.5 is the "equivalent" Poisson's ratio for a biaxial strain.

2.1.2 Elastic energy

To calculate the strain energy in a coherent epitaxial film it is useful to write the generalized Hooke's law, given by eq. 2.2, in terms of the Poisson's ratio ν and the shear modulus μ. μ is defined as the ratio between the applied shear stress and shear strain under pure shear. Inverting eq. 2.2 one obtains [Tsao93]

$$\begin{pmatrix}\varepsilon_x\\ \varepsilon_y\\ \varepsilon_z\end{pmatrix} = \frac{1}{2\mu(1+\nu)}\begin{pmatrix}1 & -\nu & -\nu\\ -\nu & 1 & -\nu\\ -\nu & -\nu & 1\end{pmatrix}\begin{pmatrix}\sigma_x\\ \sigma_y\\ \sigma_z\end{pmatrix}, \tag{2.7}$$

where the relationships between coefficients C_{ij} of eq. 2.2 and μ, ν are

$$\begin{aligned} C_{11} &= 2\mu\frac{1-\nu}{1-2\nu}\\ C_{12} &= 2\mu\frac{\nu}{1-2\nu}\end{aligned}. \tag{2.8}$$

The relation between the shear modulus and the elasticity (Young) modulus E is $2\mu=E/(1+\nu)$ [1]. Considering that the epitaxial film is oriented along the <100> direction eq. 2.7 can be written as a function of parallel and perpendicular components

$$\begin{pmatrix}\varepsilon_{||}\\ \varepsilon_{\perp}\end{pmatrix} = \frac{1}{2\mu(1+\nu)}\begin{pmatrix}1-\nu & -\nu\\ -2\nu & 1\end{pmatrix}\begin{pmatrix}\sigma_{||}\\ \sigma_{\perp}\end{pmatrix}. \tag{2.9}$$

[1] The Young modulus is defined as the ratio of stress to strain on the loading plane along the loading direction; $E = \sigma_{||}/\varepsilon_{||} = \sigma_{\perp}/\varepsilon_{\perp}$ [Landau59].

Two terms of eq. 2.9 are known: the parallel strain ($\varepsilon_{\parallel}$), given by the lattice mismatch, and the perpendicular stress ($\sigma_{\perp}$), which vanishes since the layer is free to expand vertically. Then, the parallel stress $\sigma_{\parallel}$ and perpendicular strain $\varepsilon_{\perp}$ are related to $\varepsilon_{\parallel}$ by:

$$\sigma_{\parallel} = 2\mu\left(\frac{1+\nu}{1-\nu}\right)\varepsilon_{\parallel} \tag{2.10}$$

$$\varepsilon_{\perp} = \frac{-2\nu}{1-\nu}\varepsilon_{\parallel}. \tag{2.11}$$

According to figure 2.1 an epitaxial layer strained in a direction parallel to the interface, whose in-plane lattice parameter matches that of the substrate, has a parallel stress. It also develops a perpendicular strain in the same direction as that which would preserve the unit cell volume. If $\varepsilon_{\perp}$ is exactly $-2\varepsilon_{\parallel}$ (that means $2\nu/(1-\nu) = 2$; $\nu = 0.5$) the unit cell volume is preserved. However, Poisson's ratio lies in the range 0.25-0.35 for most materials [LandoltBornstein82] and $2\nu/(1-\nu) \approx 1$ and the unit cell volume is not completely preserved.

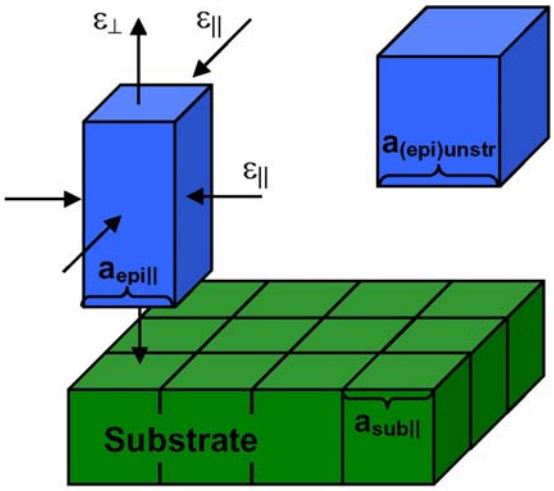

Fig. 2.1 – Sketch of the strains and lattice parameters for heteroepitaxial deposition under biaxial strain. The film unit cells develop strains $\varepsilon_{\perp}$ and $\varepsilon_{\parallel}$ related by eq. 2.11

A coherency elastic energy related to the strain in the epitaxial layer can be calculated, per unit volume, to be [Tsao93]

$$u = \frac{1}{2}\left(2\sigma_{\parallel}\varepsilon_{\parallel} + \sigma_{\perp}\varepsilon_{\perp}\right) = 2\mu\left(\frac{1+\nu}{1-\nu}\right)\varepsilon_{\parallel}^{2}. \quad (2.12)$$

The equation above is essentially a spring potential energy and will be used throughout this work when calculating elastic energies.

2.2 Ge deposition on Si (001)

Deposition of Ge on Si(001) is a model system for understanding the physics of heteroepitaxial growth. The two elements involved have similar structural and eletronic properties: they both crystallize in the diamond structure and have indirect electronic energy gap. The lattice parameters of these materials are a_{Si} = 5.431Å and a_{Ge} = 5.65Å, corresponding to a lattice mismatch of 4.2%.

Several deposition methods can be employed for Ge growth, such as liquid phase epitaxy (LPE) [Dorsch97], chemical vapor deposition (CVD) [Ross99, Vailionis00] and molecular beam epitaxy (MBE) [MedeirosRibeiro98, Montalenti04, Rastelli02]. Although the Ge growth dynamics cannot be uniquely described for all deposition methods the system follows the Stranski-Krastanov [StranskiKrastanov39] growth mode. In this kind of growth some monolayers of material grow as a two-dimensional film forming the so-called wetting layer (WL) before the formation of three-dimensional islands.

Three main different stages of growth can be distinguished for Ge:Si as shown in fig. 2.2. Ge growth first proceeds in a layer-by-layer mode up to a coverage (Θ) of about 3.5 monolayers (ML) of Ge. Then, for thicker layers, the elastic strain is released by the formation of small pyramidal shaped islands. Pyramids are islands with a low aspect ratio and {105} facets. Finally, when the Ge coverage exceeds approximately 6MLs (and for a constant growth temperature) a shape transition from pyramids to dome islands occurs [MedeirosRibeiro98, Montalenti04]. Dome islands are larger in volume (number of atoms) and in height (despite of having essentially the same base radius of pyramids), exhibiting more complex facets when compared to pyramids.

A phenomenological model for island growth in Stranski-Krastanov systems that includes island shape transitions was proposed by Shchukin et. al. [Shchukin95]. In a simplified version of this model the total energy (U_{Total}) stored by an island with volume V

can be described by the sum of surface ($U_{Surface}$) and volume (U_{Volume}) energy contributions. The surface term depends on the island faceting angle α that represents the ratio of the facet angle to an arbitrary reference angle. The energy is, then, given by

$$\begin{aligned} U_{Total} &= U_{Surface} + U_{Volume} \\ &= \alpha^{4/3} \cdot V^{2/3} + U_{elastic} \end{aligned} , \tag{2.13}$$

where $U_{elastic}$ is the elastic energy of the whole island. The ratio between $U_{elastic}$ and V is denoted by u and given by eq. 2.12 of the preceding section. Dividing 2.13 by the island volume *V* one obtains the dimensionless energy

$$u_{Total} = \alpha^{4/3} \cdot V^{-1/3} + u . \tag{2.14}$$

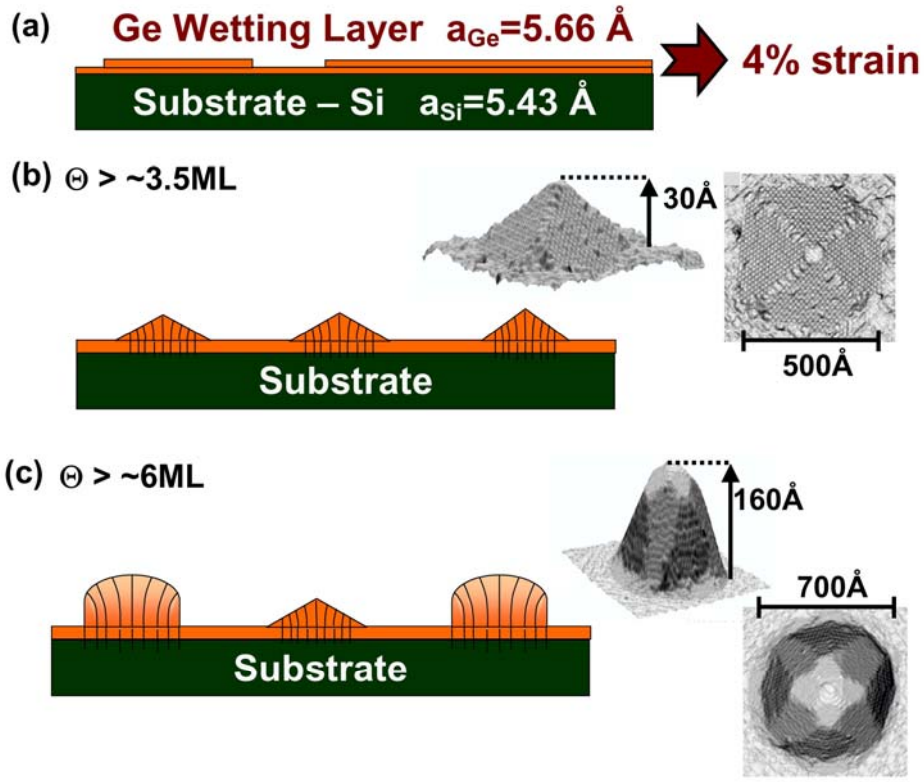

Fig. 2.2 – Steps of Ge growth on Si(001). (a) Wetting layer formation. (b) pyramid islands nucleation for coverages Θ > ~3.5 ML. (c) Island shape transition to domes for Θ > ~6ML. Typical pyramid and dome islands are shown with their dimensions (scanning tunneling microscopy images from [Rastelli02]).

The per-atom energy u_{Total} (eq. 2.14) of the WL is constant since it has only two facets (the film interfaces) with α = 0 while the total energy U_{Total}, given by eq. 2.13, scales linearly with its thickness. Pyramids and domes have both non-constant surface terms with

the ratio between faceting angles given by $\alpha_{Pyramid} \approx 1/3\ \alpha_{Dome}$. In the limit of very small volumes the formation of a film will be always favored over islanding. For larger volumes the surface term becomes less important and the surface energy of islands decreases. However, in order to have WL-pyramid and pyramid-dome transitions the elastic energy term (u) of eq. 2.14 must follow the condition $u_{WL} > u_{Pyramids} > u_{Domes}$. A plot of eq. 2.14 using this elastic energy condition is shown in fig. 2.3. The aim of this chapter it to prove experimentally that an elastic energy reduction takes place during the transitions from WL to pyramids and from pyramids to domes.

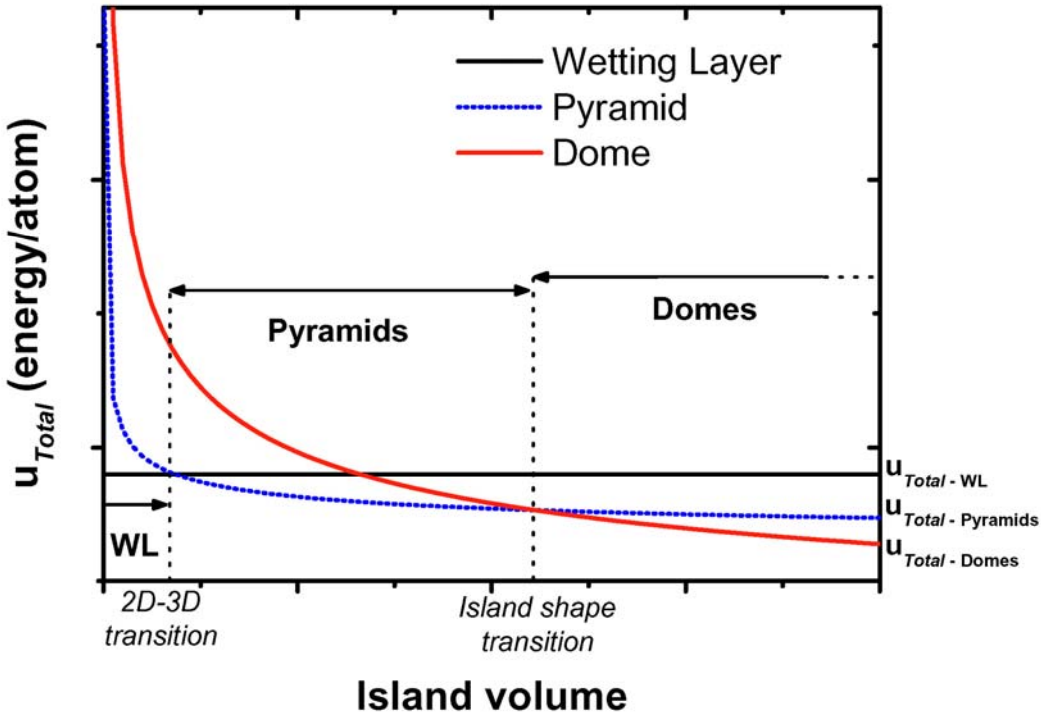

Fig. 2.3 – Phenomenological model for Stranski-Krastanov island shape transition [Shchukin95]. The WL per-atom total energy is constant (horizontal solid line). Dashed vertical lines indicate regions where the growth of WL, pyramids (dashed curve) or domes (solid curve) is favored over the other structures.

In this chapter we show results in two samples grown by CVD, one containing pyramids and another containing domes. The Ge films were deposited on ligthly doped, 150-mm-diam, p-type, (001)-oriented Si wafers at a total pressure of 10 Torr in a H_2 ambient. The layers were deposited in a commercially avaliable, load-locked, lamp-heated reactor with the wafer supported by a SiC-coated graphite plate with moderate thermal mass. After baking a wafer at a nominal temperature of 1150°C in a H_2 ambient to clean the

surface, a Si buffer layer was grown at about 1080°C, using SiH_2Cl_2 as the Si source gas. The temperature chosen for the growth of Ge films was 600°C. The Ge source gas was GeH_4 diluted in H_2. A pyramid sample with 5.9 ML of Ge was grown with a deposition rate of 0.1ML/s for a total deposition time of 60s. For the dome sample 11.2 ML of Ge were deposited at 0.05ML/s for a total deposition time of 240s. Although the growth rates were different, 0.1ML/s represents the upper limit for low supersaturation conditions for the growth of Ge at 600°C. After the Ge samples were grown they were immediately cooled down under a H_2 flow. It has to be emphasized that the difference between these two samples besides the Ge thickness is the corresponding extra amount of time – 180s – necessary for the film growth. Atomic Force Microscopy (AFM) was performed with a Digital Instruments Nanoscope IIIa (at LNLS) and the statistical analysis consisted of evaluating diameter and heights of over 1000 nanocrystals in a $4\mu m^2$ area. In figure 2.4 typical AFM measurements of both samples are shown [MagalhãesPaniago02] as well as size histograms.

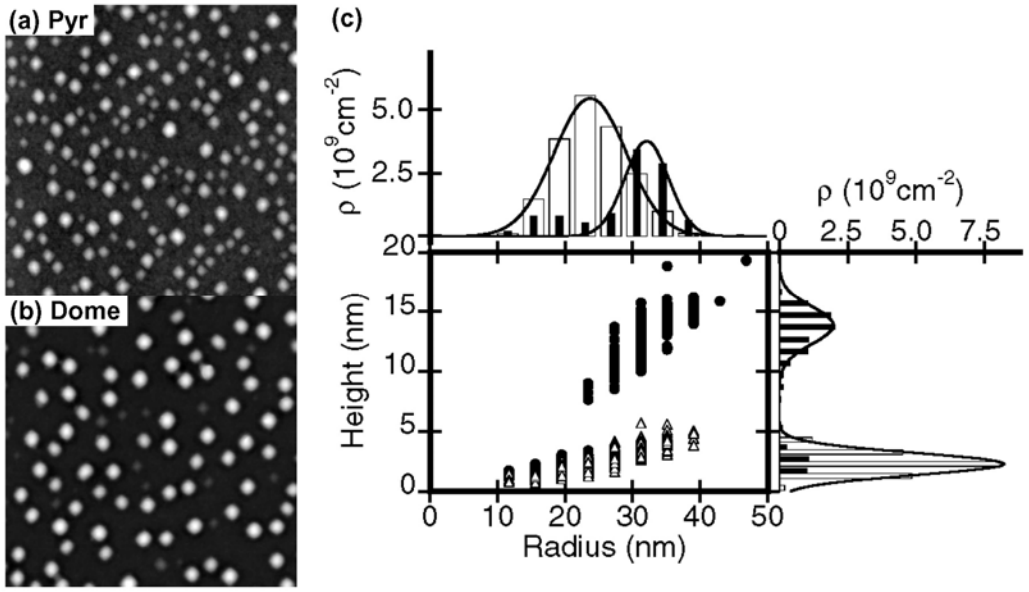

Fig. 2.4 – $1\mu m^2$ AFM images of Pyramid (a) and Dome (b) samples. Note the smaller size of the pyramid islands. The shape of these islands is not completely clear from the measurements due to tip convolution effects. (c) Statistical analisys performed in a $4\mu m^2$ area; open symbols and bars correspond to the pyramid sample whereas solid ones correspond to the dome sample. It can be seen quite clearly the different island types from the height x radius plot.

In both samples the island ensembles are essentially monodisperse. There is a small percentage of pyramid islands amidst the dome sample. However, this small percentage adds a negligible amount of uncertainty in the x-ray experiments due to the reduced volume they represent. From the size distribution analysis of fig. 2.4(c) the following morphological parameters were obtained for the islands of the two samples: Pyramid sample has islands with height 30±10Å and radius 240±60Å; Dome sample has islands with height 140±20Å and radius 320±40Å [2].

2.3 In-plane strain distribution

In order to evaluate the lattice parameter relaxation inside Ge islands GID measurements were performed at the XRD1/XRD2 beamlines using the two samples described in the preceding section. The x-ray energy was fixed to 11KeV and the incident angle was set to 0.35°, essentially the critical angle of total external reflection of the silicon substrate.

Two types of scan can be done in the GID geometry. A radial scan is performed by varying $q_r = (4\pi/\lambda)\sin(2\theta/2)$ (eq. 1.51). This is done experimentally by coupling ω to 2θ with the condition $\omega = 2\theta/2$. Thus, by Bragg's law $\lambda = 2d\sin(2\theta/2)$, radial scans are sensitive to the in-plane lattice parameter and, consequently to the strain status of the islands. For each value of 2θ the scattering from regions of the island with different lattice parameters $a' = 2\pi/q_r$ is probed.

In fig. 2.5(a) we show two radial scans, along the (400) direction, for the dome and the pyramid samples. Since the lattice parameter difference between Si and Ge is 4.2%, these scans span from the Si substrate lattice parameter (sharp substrate peak) up to regions corresponding to larger in-plane lattice parameters, meaning lower q_r values (see arrows indicating bulk Si and Ge peak positions). The arrows point to three selected strained regions inside dome islands that were schematically represented in fig. 2.5(b). For the pyramids a peak is not quite well developed, indicating the higher strain (only 1.5%

[2] A list of samples is shown in appendix B of this thesis.

relaxation) of this particular shape due to its lower aspect ratio. The dome shaped islands, with a higher aspect ratio, are clearly more relaxed since some x-ray scattered intensity can still be observed for $q_r = 4.48Å^{-1}$ (a' = 5.63Å; 3.8% relaxation). This is a first indication that the elastic energy stored inside pyramids is released during the transition to dome islands [Malachias03a].

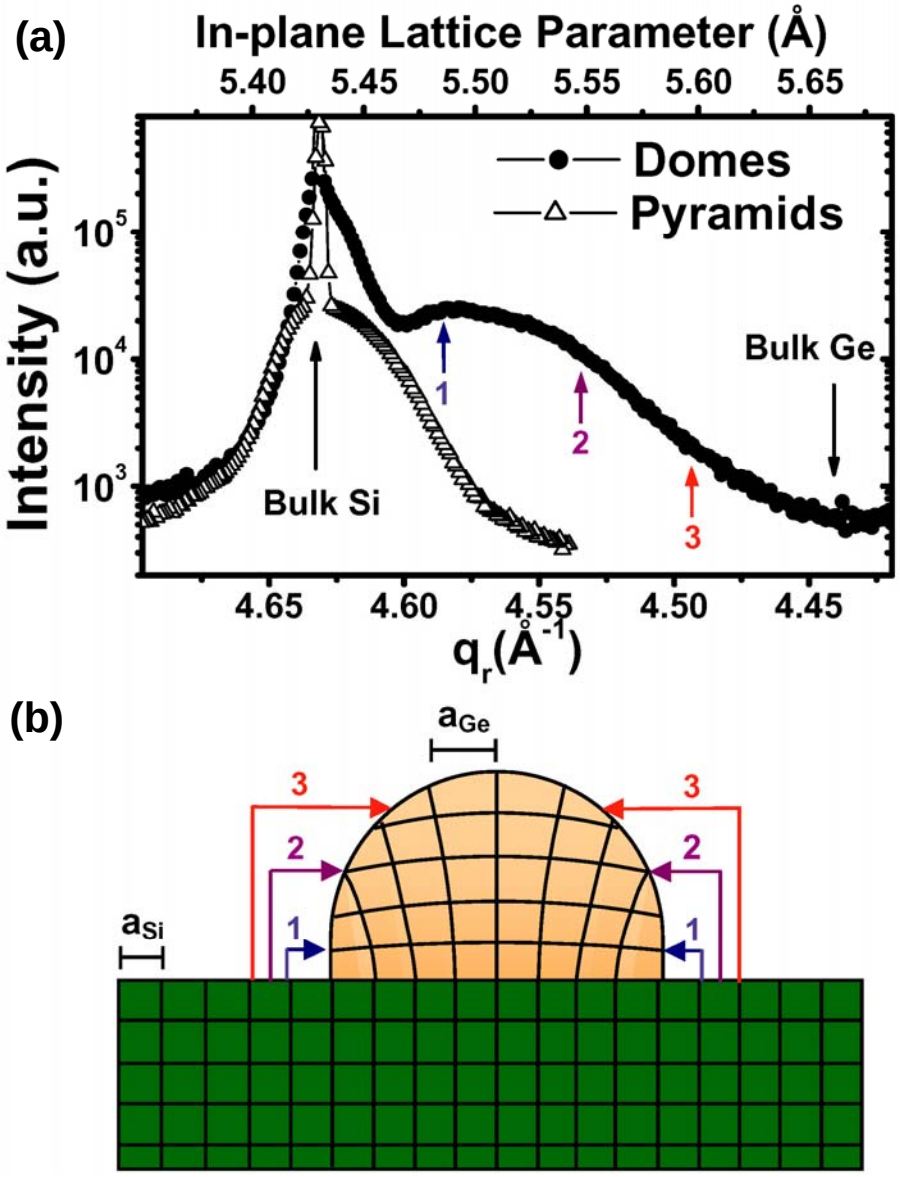

Fig. 2.5 – (a) X-ray radial scans along q_r stemming from the distribution of lattice parameter in the vicinity of the Si (400) reflection inside both pyramids and domes. The upper scale indicates the in-plane lattice parameter. (b) Sketch of the strained regions of a dome island, shown in the dome radial scan of (a).

2.4 Island strain mapping by angular scans

The relationship between island size and strain is determined by angular ω (q_a) scans with the scattering angle 2θ (q_r) fixed. Figure 2.6 (a) and (b) show these angular scans in the vicinity of the (220) reflection for the pyramid and dome sample, respectively, where q_a corresponds to the (1-10) direction. Since the full width at half maximum of these diffraction profiles is inversely proportional to the size of the scattering object [Cowley81, Kegel99], an important point can be made about the origin of the scattered intensity for each angular cut. As the lattice parameter increases, the central maximum broadens, indicating the decrease of the lateral dimension of scattering objects. Hence, our Ge islands are wide in regions where the lattice parameter is close to Si, i.e., the bottom of the islands, and constricted at the nearly relaxed top. Since there is a gradual change of the width of the diffraction profile as a function of a', these islands are nearly monotonically strained from bottom to top [MagalhãesPaniago02].

To quantify the dependence of the island size to its lattice parameter, an analytical description of the angular scattering from portions of the islands limited by planes parallel to the substrate surface was employed. We have assumed that the islands have square sections of side length *L* along the (1-10) direction for a given lattice parameter a' = $2\pi/q_r$. An schematic representation of one square section is seen in fig. 2.7(a). In this case, the scattered intensity of an angular q_a-scan for a fixed q_r can be calculated using eq. 1.23 with constant atomic scattering factor [Warren69, Kegel99, Malachias01]:

$$I(q_a) = \frac{I_0}{L^2}\left|\frac{\sin\left(L/2\, q_a\right)}{\sin(q_a)}\right|^2 . \qquad (2.15)$$

Angular profiles generated by eq. 2.15 are seen in fig. 2.7(b) for two different square sizes. The full width at half maximum of these profiles is inversely proportional to the size of the scattering object.

The solid lines in figures 2.6(a) and 2.6(b) are least-square fits using eq. 2.15, which were performed adjusting only the island diameter for every fixed q_r and included the size distribution from the AFM data.

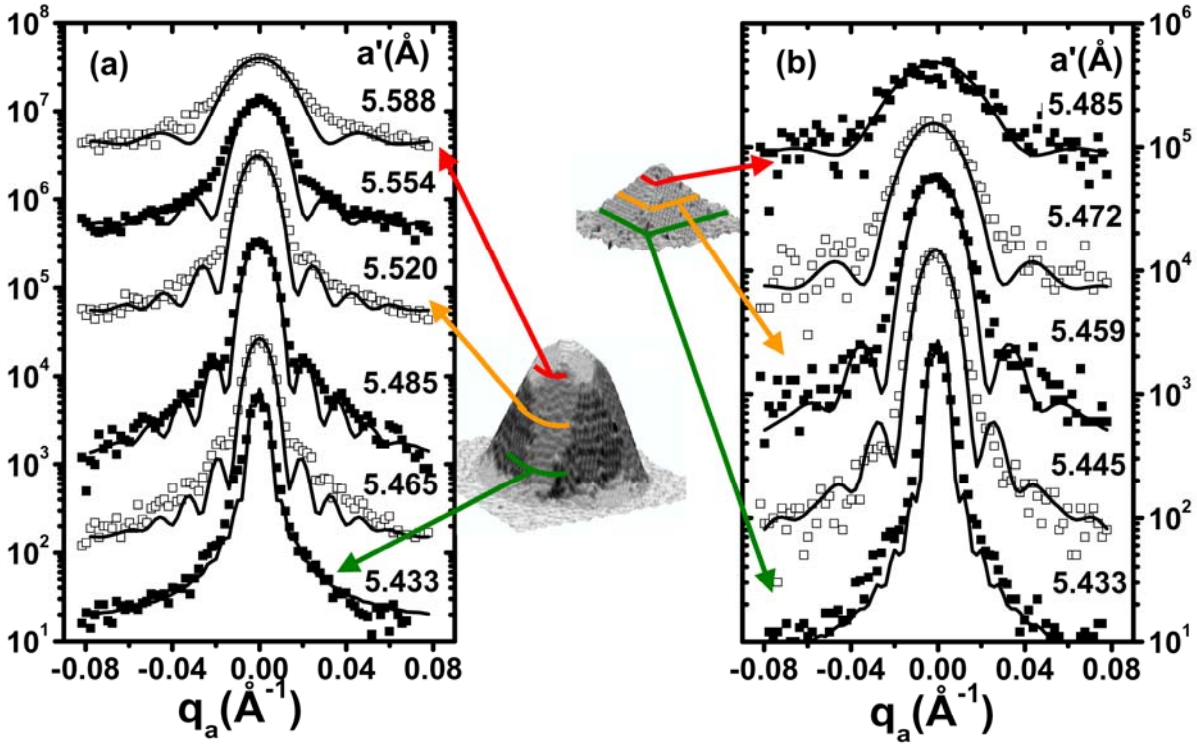

Fig. 2.6 – Angular scans along the [1-10] direction at different local lattice parameters a' (q_r positions), for the dome sample (a) and for the pyramid sample (b). The solid lines are fits according to eq. 2.15. The STM pictures [Rastelli02] indicate schematically the iso-lattice parameter regions inside each island.

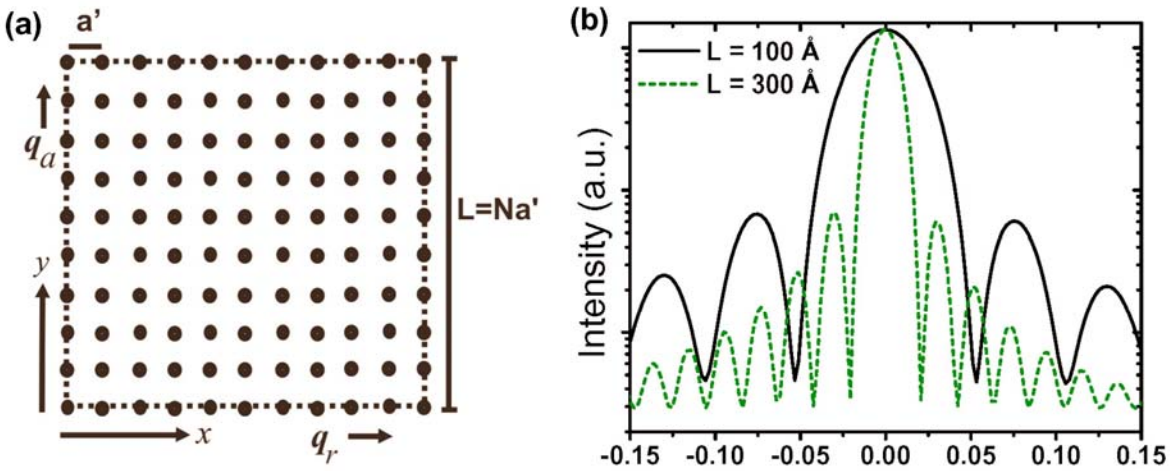

Fig. 2.7 – (a) Sketch of a square section inside an island. (b) Angular profiles generated by eq. 2.15 for L = 100Å (solid line) and L = 300Å (dashed line).

The x-ray results obtained allowed us to associate the island diameter and the local lattice parameter. However, no information about the variation of strain as a function of island height was obtained. Therefore, we have correlated this result with typical atomic force microscopy profiles for both types of island. Figure 2.8 shows the AFM line profiles taken on pyramid and dome islands along with the lattice parameter to radius relationship. For the pyramids (empty triangles) this relationship is monotonic, indicating a smaller lattice parameter for decreasing radii. As for the domes (filled circles), a more complex dependence is revealed and most notably the fact that it is no longer monotonic. The reason for the decrease in radius for decreasing lattice parameters around 5.46Å is related to the fact that we are probing regions of constant lattice parameter under the island, which have a smaller radius than the islands base [Kegel99, Malachias01, MagalhãesPaniago02].

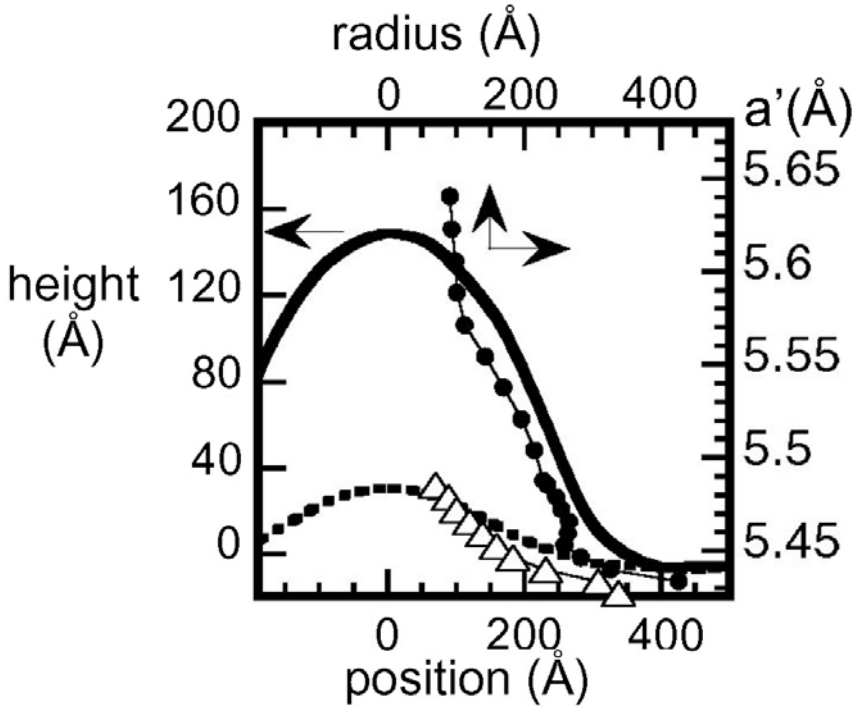

Fig. 2.8 – Comparison between AFM profiles for pyramids (dashed line) and domes (solid lines) and x-ray radius vs lattice parameter relationship obtained from angular scans. The open triangles are x-ray results for the pyramid sample while the dots refer to the dome sample.

2.5 Evaluation of the vertical Ge/Si concentration

For the determination of the Ge/Si vertical concentration inside both pyramids and domes, we have performed anomalous (220) radial scans at two specific x-ray photon energies near the Ge K edge, as was discussed in section 1.2. As shown in figure 2.9, by tuning the x-ray energy near the Ge K absorption edge (11103eV) the Ge atomic scattering factor (f_{Ge}) diminishes by 9 electron units. Since the Ge scattering factor varies rapidly near its K-edge, the x-ray beam was set with a broad energy resolution of 8eV to minimize possible energy fluctuations and to make this variation smoother.

Figure 2.10 shows the change in scattering intensity near the Ge edge for the two x-ray energies for the dome (a) and pyramid (b) samples. The difference in intensity varies from 0 to 35% for these islands (for pure Ge should change by 35%), depending on the strain state of the islands. From fig. 2.10 (a) one can state that there is a substantial amount of Si inside the domes, most notably at the island base. The pyramid sample (fig. 2.10(b)) exhibits a considerable intensity contrast already at local lattice parameters very close to Si, indicating a higher average Ge content as compared to domes.

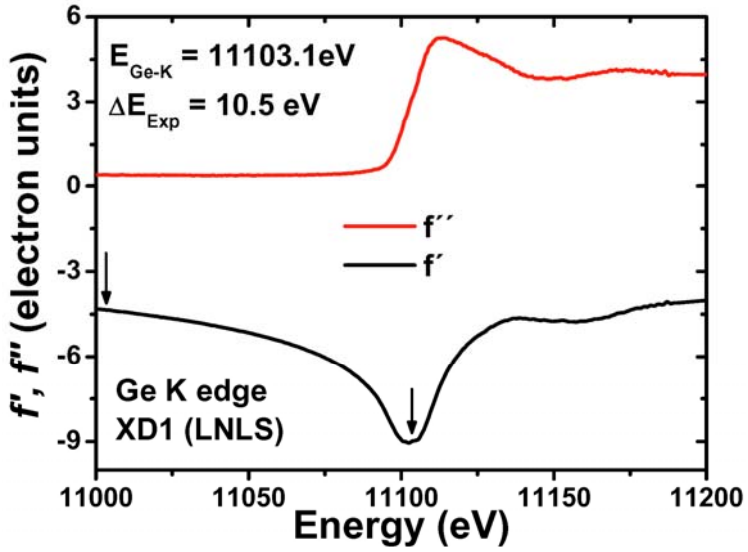

Fig. 2.9 – Variation of real and imaginary corrections of the atomic scattering factor of Ge near its K-edge. The imaginary part *f*" was obtained experimentally from the absorption of a Ge foil. The experimental curve of *f*' was obtained using the Kramers-Kronig relation [SchulliHP]. Note the drastic decrease of f_{Ge} at 11103 eV. Arrows indicate the two energies (11003eV and 11103eV) that were used in the experiments. Energy resolution was set to 8 eV. The Ge atomic scattering factor is given by $f_{Ge} = f_0(Q) + f'(E) + if''(E)$ (eq. 1.17).

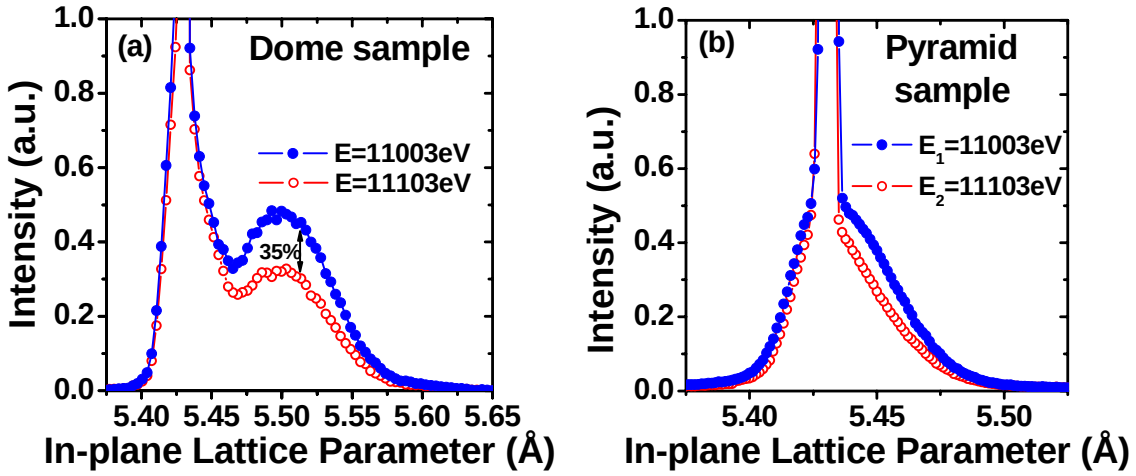

Fig. 2.10 – X-ray radial scans along the (220) direction using two different x-ray photon energies near the Ge K-edge for the dome (a) and pyramid (b) samples. The q_r axis was directly converted to in-plane lattice parameter. The arrow indicates where the difference of intensity is ~35%, i.e. where the island is pure Ge.

Since the islands are composed of two species, the x-ray scattered intensity at the (220) reflection is proportional to the square of the sum of the concentration of each one multiplied by the corresponding Ge or Si scattering factor

$$I_1 = \text{Constant}\left|C_{Ge} f_{Ge} + C_{Si} f_{Si}\right|^2, \tag{2.16}$$

where C_{Ge} and C_{Si} are the Ge and Si concentration inside the islands ($C_{Ge} + C_{Si} = 1$), f_{Ge} and f_{Si} are the atomic scattering factors of Ge and Si respectively and all scattering parameters such as photon flux, sample area, etc, are included in the Constant. If we vary the x-ray photon energy near the absorption edge of one of these two atomic species (in this case, germanium), the scattering factor changes drastically. The ratio of two measured intensities is essentially a function of the scattering factors and the atomic concentrations, i.e.,

$$\frac{I_1}{I_2} = \left|\frac{C_{Ge} f_{Ge1} + C_{Si} f_{Si}}{C_{Ge} f_{Ge2} + C_{Si} f_{Si}}\right|^2, \tag{2.17}$$

where I_1 and I_2 are the measured x-ray intensities and f_{Ge1} and f_{Ge2} the Ge scattering factors for two different energies. One then obtains for the Ge concentration

$$C_{Ge} = \left(1 + \frac{f_{Ge2}\sqrt{I_1} - f_{Ge1}\sqrt{I_2}}{f_{Si}\left(\sqrt{I_2} - \sqrt{I_1}\right)}\right)^{-1}. \tag{2.18}$$

As shown in figs. 2.9 and 2.10, we have chosen two energies, one reasonably far from the Ge absorption edge (E=11002eV) and another right at the edge (E=11103eV). The variation of the atomic contrast is clear, most notably for lattice parameters near the value for Ge bulk position, where the island should be composed of almost pure Germanium. By performing this procedure for all lattice parameters ($a' = 2\pi/q_r$) between the values of Si and Ge, we have extracted the dependence of C_{Ge} to lattice parameter and mapped out the compositional profile for each island. The concentration for both types of islands is given in figure 2.11. In fig. 2.11 (a) the composition is given as a function of lattice parameter. Using the height × lattice parameter relationship of fig. 2.7 one can plot the composition directly as a function of height as shown in fig. 2.11 (b).

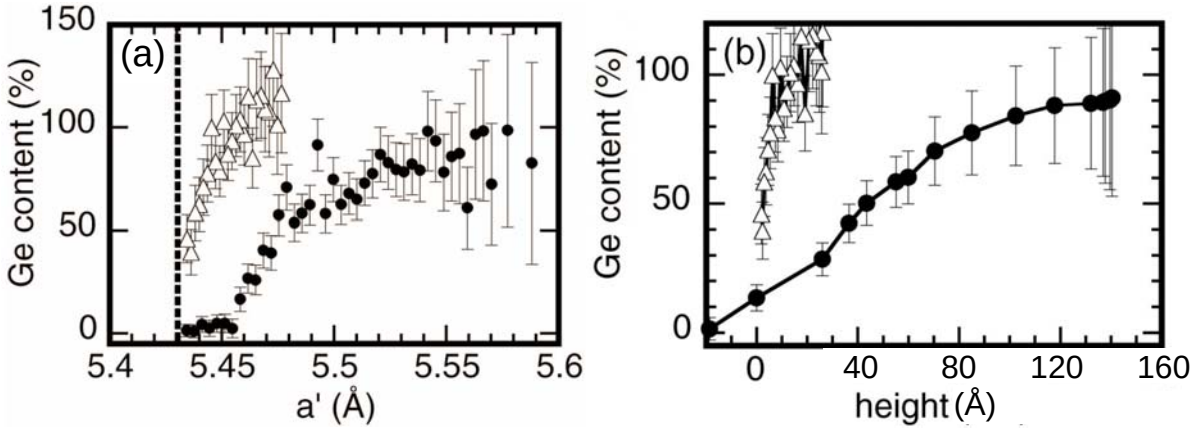

Fig. 2.11 – (a) Ge concentration as a function of local lattice parameter (obtained using eq. 2.15) for both pyramids (triangles) and domes (circles). (b) Ge content as a function of height obtained from a comparison of x-ray anomalous scattering results and typical atomic force microscopy images for both pyrmids (triangles) and domes (circles). Mudar fig.b para Ge content.

2.6 Strain relaxation and elastic energy

It can be seen that the average Ge content on pyramids is much higher than on domes. However, the lattice relaxation is larger for domes than pyramids. For these two experimental results we can see that on a per-atom basis pyramids store more elastic energy than domes. How much is stored? Before getting to the answer, further analysis can improve our understanding of strain status of islands of different shape.

One cannot determine strain without a simultaneous measurement of both local lattice parameter (fig 2.8) and composition (fig 2.11) of the nanocrystal. This is because the change in lattice parameter can be both due to substrate imposed stress as well as change in composition. The correct value of the local strain of the nanocrystal with local composition Si_yGe_{1-y} is given by eq. 2.1, where the lattice parameter of the unstrained alloy is given by $a_{(epi)\text{unstr}} = (1-y)a_{Si} + ya_{Ge}$ and $a_{(epi)\|}$ is the local lattice parameter .

Fig. 2.12 displays the value of the lateral strain (eq. 2.1), inferred from the measured in-plane lattice parameter *a* and the lattice parameter of an unstrained alloy of composition Si_yGe_{1-y} (calculated using Vegard's law). This plot can be divided roughly into two regions: tensile strained material which correspond to the region where $\varepsilon_{\|} > 0$ (below the dashed line) and; compressed strained material that correspond to $\varepsilon_{\|} < 0$ (above the dashed line). One can see than that the average strain in pyramids and domes is about 3% and 1.5%. Moreover, for the domes one can see the underlying tensile stressed Si substrate which correspond to the data for a' < 5.46Å.

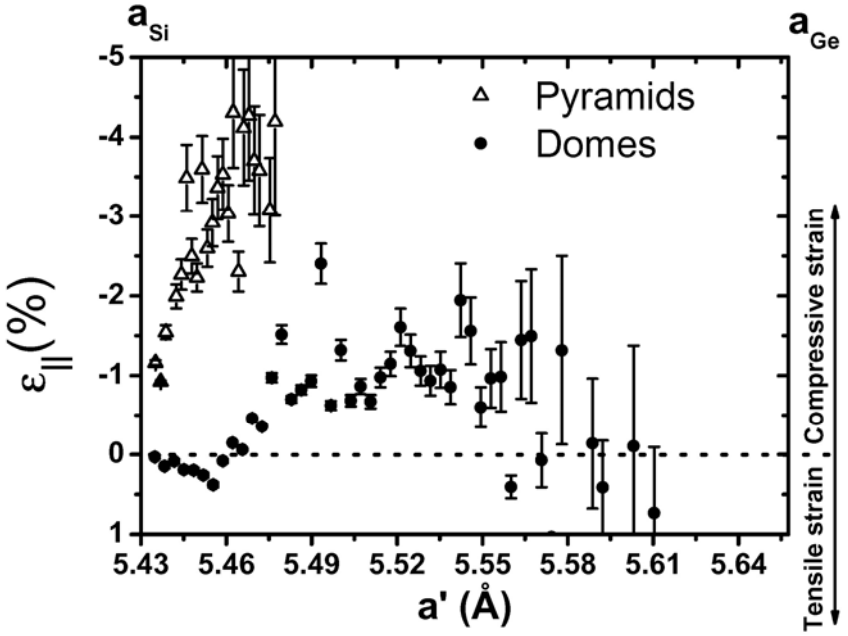

Fig. 2.12 – In-plane strain $\varepsilon_{\|}$ as a function of a' for pyramids and domes. The x-axis of this graph spans from Si to Ge bulk lattice parameter value. The horizontal dashed line correponds to zero strain condition; i.e., that of a SiGe unstressed alloy. Regions below and above the dashed line correspond to tensile and compressive strain, respectively.

In order to evaluate the elastic energy stored we have used the values of strain of fig. 2.12. The elastic energy u per unit volume for a strained alloy is given by eq. 2.12 with μ and ν as the shear modulus and Poisson ratio of the alloy and $\varepsilon_{||}$ as the local strain. From this relation we can extract the elastic energy on a per atom basis by using the Ge atom density. Fig. 2.13 shows the energy on a per atom basis height profile for a 2D uniformly strained pure Ge film grown on a Si substrate (solid line), for pyramids (triangles) and domes (circles). This shows that the average energy per atom for a 2D layer is roughly twice as much that of a pyramid and ten times larger that of a dome. The transition from pyramids to domes is therefore clearly accompanied by a drastic decrease of elastic energy per atom stored in the islands. This result supports the elastic energy condition ($u_{WL} > u_{Pyramids} > u_{Domes}$) discussed in section 2.2 and necessary for the island shape transition.

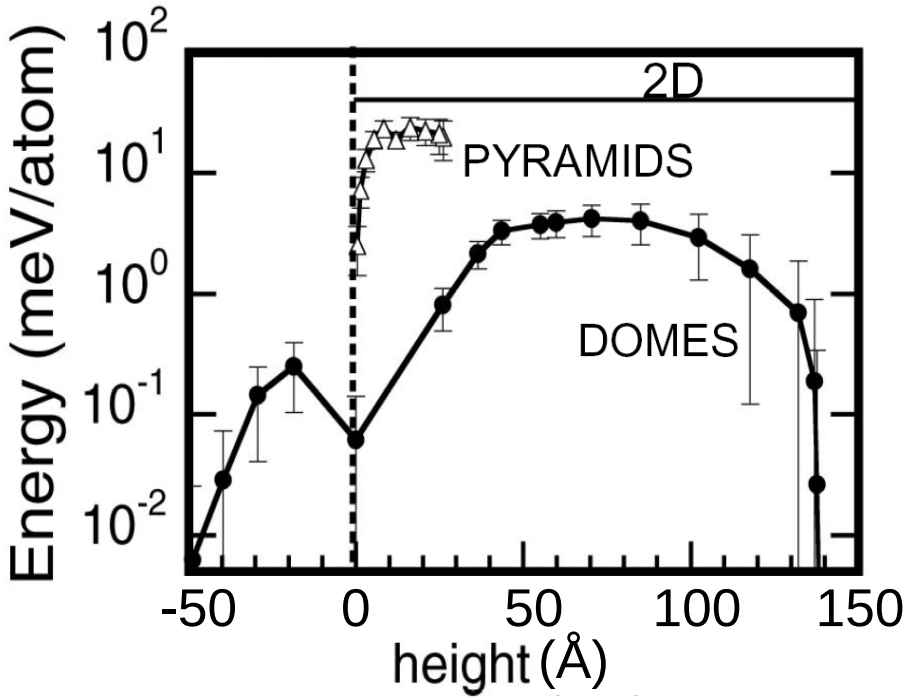

Fig. 2.13 – Energy on a per atom basis as a function of height for a uniformly strained 2D Ge layer (solid line), pyramids (triangles) and domes (filled circles).

Finally, fig. 2.14 shows the Ge concentration superimposed on the AFM topographic images, emphasizing the Si enrichment of the dome shaped islands. The higher Si content on domes can be initially assigned to the lower deposition rate (longer growth

time) used in this sample. This enrichment is crucial for the reduction of the per-atom elastic energy that leads to the island shape transition.

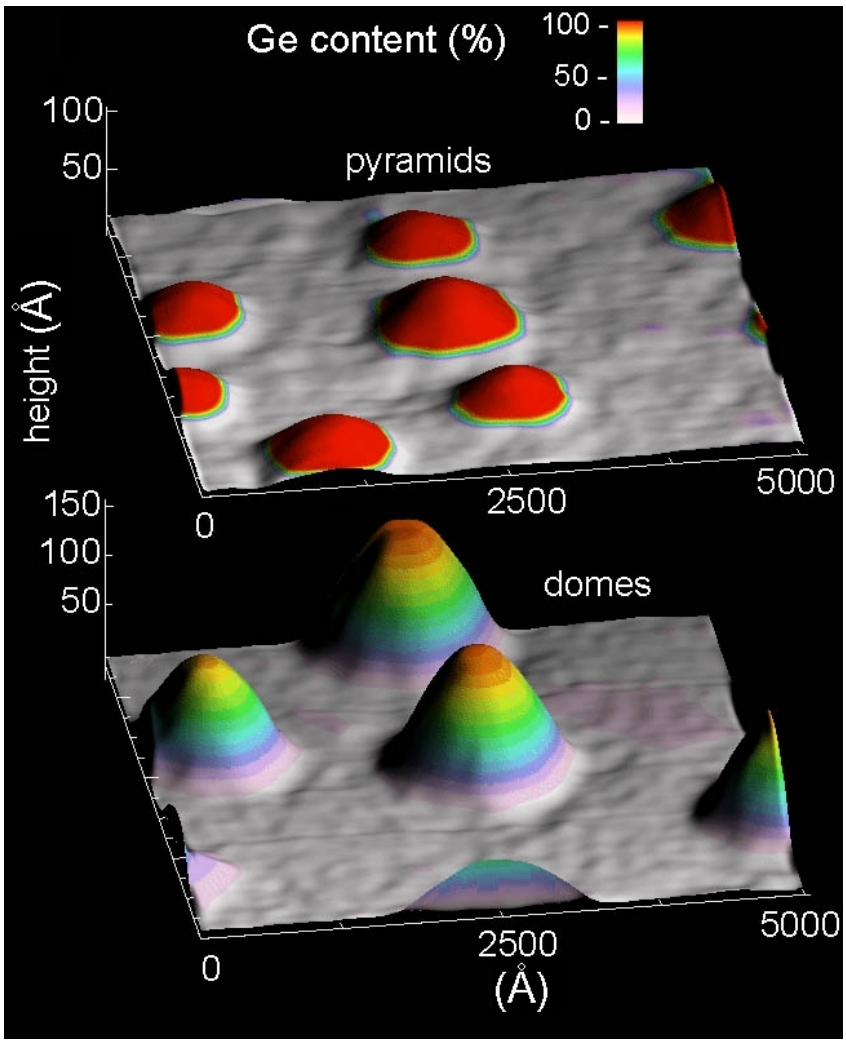

Fig. 2.14 – Ge concentration as a function of height composed with typical atomic force microscopy profiles for both pyramids and domes, showing the higher concentration of Ge in the pyramids.

2.7 Reciprocal space maps and vertical lattice parameter

A complete analysis of the strain inside the islands can be outlined by correlating the in-plane strain ($\varepsilon_{\parallel}$) and the out-of-plane strain ($\varepsilon_{\perp}$). In order to separate these strain contributions in reciprocal space and have a clear distinction of in-plane and out-of-plane strain status we have mapped the asymmetric reflection (2 0 2) [AlsNielsen01, Pietsch04].

Scattering measurements in the vicinity of the (2 0 2) Si Bragg peak were performed at the XRD2 beamline. The photon energy was set to 8KeV and the incident angle was fixed at 0.1°. In this section the results are shown in reciprocal lattice units using the HKL notation. This allows an easy conversion to both in-plane ($a_{\parallel}$') and out-of-plane ($a_{\perp}$') local lattice parameter since

$$a_{\parallel}' = \tfrac{1}{2}a_{Si} \times (H^2)^{-\frac{1}{2}} \quad \text{and} \quad a_{\perp}' = \tfrac{1}{2}a_{Si} \times (L^2)^{-\frac{1}{2}}. \qquad (2.19)$$

Fig. 2.15(a) shows the (2 0 2) reciprocal space map for the dome sample while fig. 2.15(b) shows a schematic drawing of in-plane and out-of-plane lattice parameter for this island. The map of fig. 2.15(a) consists of a collection of K-scans for different L's. By choosing coordinate pairs H-L inside the mapped region one can correlate in-plane and out-of-plane lattice parameters using eq. 2.19 [Zhang00, Malachias03b].

It is possible to distinguish different diffraction structures in this map. The Si(001) substrate Crystal Truncation Rod[3] (CTR) [Robinson86] is observed along the L direction for H = 2. Scattered intensity from Ge domes is observed around the D point of the map. As explained in section 2.1.1 the biaxial in-plane strain leads to a vertical (tetragonal) expansion of Ge unit cells. This distortion is shown in the blue region of fig. 2.15(b). At the islands basis, where the in-plane lattice parameter is close to Si ($H \approx 2$) the tetragonal distortion is stronger and the unit cells exhibit a bigger vertical lattice parameter ($L \approx 1.9$). Inversely, at the islands top ($H \approx 1.94$), the in-plane lattice parameter is closed to the bulk Ge for an essentially pure Ge composition obtained in the preceding section. This leads to lower distortions in the vertical unit cell dimension. No scattered intensity is found at the bulk (unstrained) Ge position, marked with a red X.

[3] In the case of an infinite three dimensional crystal the reciprocal lattice consists of delta function peaks. In the other hand, for a finite size crystal the scattering extends over a volume in reciprocal space inversely proportional to the size of the crystal and the reciprocal lattice peaks will present a broadening effect. If the crystal is cleaved and has a flat surface the scattering will no longer be isotropic and streaks of scattering will appear in the direction normal to the surface. Such streaks are known as Crystal Truncation Rods (CTR's) [Robinson86].

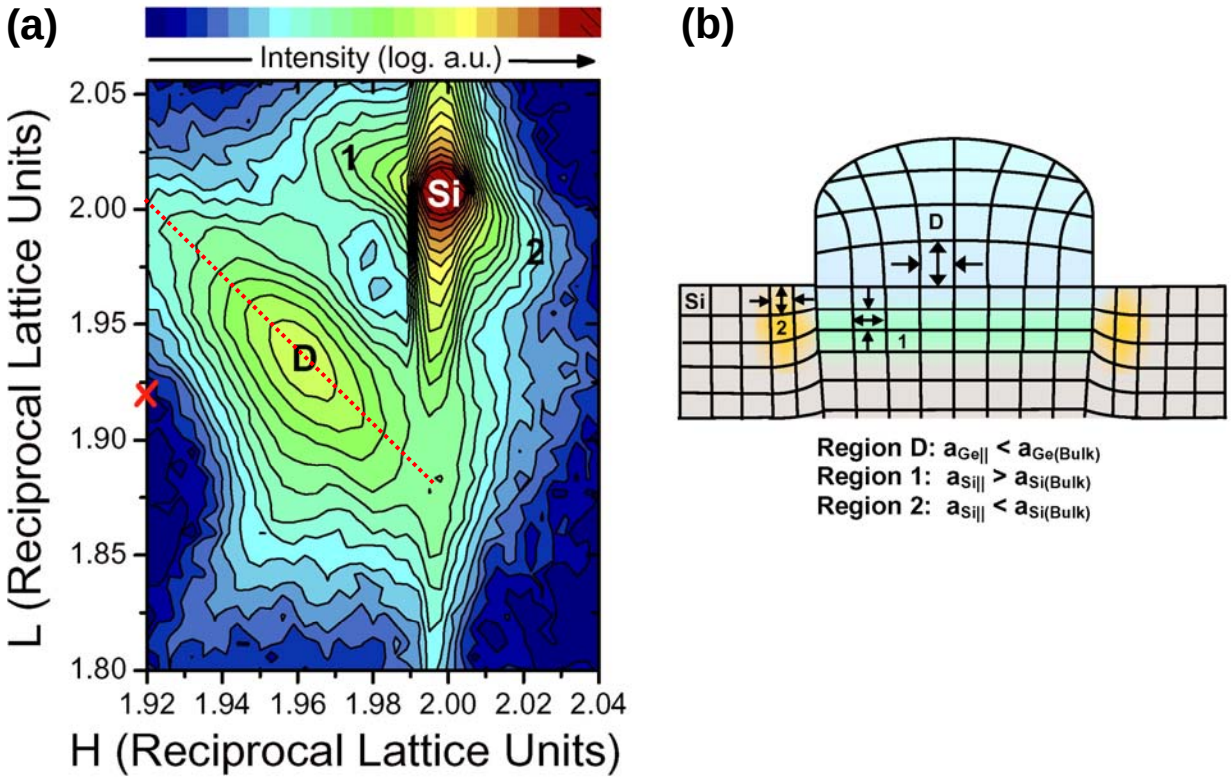

Fig. 2.15 – (a) Reciprocal space map in the vicinity of the (2 0 2) Si reflection. The structures labeled D, 1 and 2 are discussed in the text. The dashed red line indicates the relaxation of a $Si_{0.4}Ge_{0.6}$ alloy under the biaxial strain. The red X point is located at the Ge bulk position. (b) Sketch of the in-plane and out-of-plane lattice parameters and strains inside a Ge dome. Typical unit cell strain status correlated to regions D, 1 and 2 of (a) were labeled in (b).

A quantitative analysis of the region D cannot be directly performed as in references [Zhang00, Malachias03b]. These works were done in InAs/GaAs islands which have a simplified strain response to the pseudomorphic growth. As explained in section 2.1.1, the vertical lattice parameter depends on the applied strain and the island composition. Since the In concentration varies linearly from the bottom to the top of InAs islands, with no lateral variation, each region at a fixed height has only one in-plane and one out-of-plane lattice parameter [Malachias03b]. A L-cut in the (202) map of InAs islands exhibits one single scattering peak, indicating a monotonic relaxation of lattice parameter inside these islands from botton to top. In the case of Ge domes, a L-cut in the reciprocal space map that passes trough the region D generally presents more than one intensity peak. Moreover, the island peak width is always too broad to allow a direct correlation between in-plane and out-of-plane strain status inside domes. This suggests the existence of a lateral Ge

concentration in these islands since the same out-of plane lattice parameter is present in regions with distinct in-plane strain. The lateral variation in Ge concentration will be discussed quantitatively in chapter 3.

An alternative approach to evaluate the Ge composition qualitatively in these maps was done for MBE-grown Ge islands was suggested by Tobias Schülli et. al. [Schülli05, Schülli03b]. The red dashed line shown in the map of fig. 2.15(a) represents the pseudomorphic relaxation of a $Si_{0.4}Ge_{0.6}$ alloy under a biaxial strain. By using this method only an average Ge content is obtained. The exact composition and location of each strained region cannot be directly evaluated in this map since the scattered intensity distribution at the region D strongly depends on dynamical effects of the chosen incident angle [Kegel01].

Two additional regions in the map, corresponding to strained Si structures, were labeled as 1 and 2. In region 1 the scattered intensity comes from portions of the substrate where Si unit cells have a larger in-plane lattice parameter as compared to bulk Si. As discussed in the preceding sections this type of distortion is found in regions located below Ge islands (green region in the dome drawing of fig. 2.15(a)) that are constricted to a tensile strain, leading to a reduction of the vertical dimension of Si unit cells. Region 2 corresponds to compressed Si in the substrate close to the island edge (orange region of fig. 2.15(b)), forming a ring structure around the island (trenches). Both structures have been predicted by molecular dynamics [Raiteri02] and finite-element calculations [Tambe04] and observed by transmission electron microscopy (TEM) [Ide99].

A similar map was obtained for the pyramid sample. In this case, due to the higher in-plane strain in this kind of island, all scattered signal is restricted in the region between H = 2 and H = 1.98. In a (2 0 2) map the intensity measured in this region is essentially generated by the Si CTR. To reduce the influence of the CTR the pyramid mapping was performed in a slightly shifted K-plane. The result of the (2 0.007 2) mapping procedure is shown in fig. 2.16(a). Most of the scattering that comes from pyramids is seen close to the point P. This indicates that the material inside these islands is highly strained but has a constant-high Ge-concentration since the scattering is stronger at L = 1.96. The pseudomorphic relaxation line shown in fig. 2.15(a) for a $Si_{0.4}Ge_{0.6}$ alloy suggests that the maximum scattered intensity of a Ge rich pyramid may be observed below the actual region

P. This suggests that the scattered intensity around the region P is still partially influenced by the CTR. The structures 1 and 2 that were discussed for the dome map of fig. 2.15(a) are barely seen here due to the weak substrate distortion by the low aspect ratio and volume of pyramids. A sketch of lattice parameter and strain is shown in fig. 2.16(b).

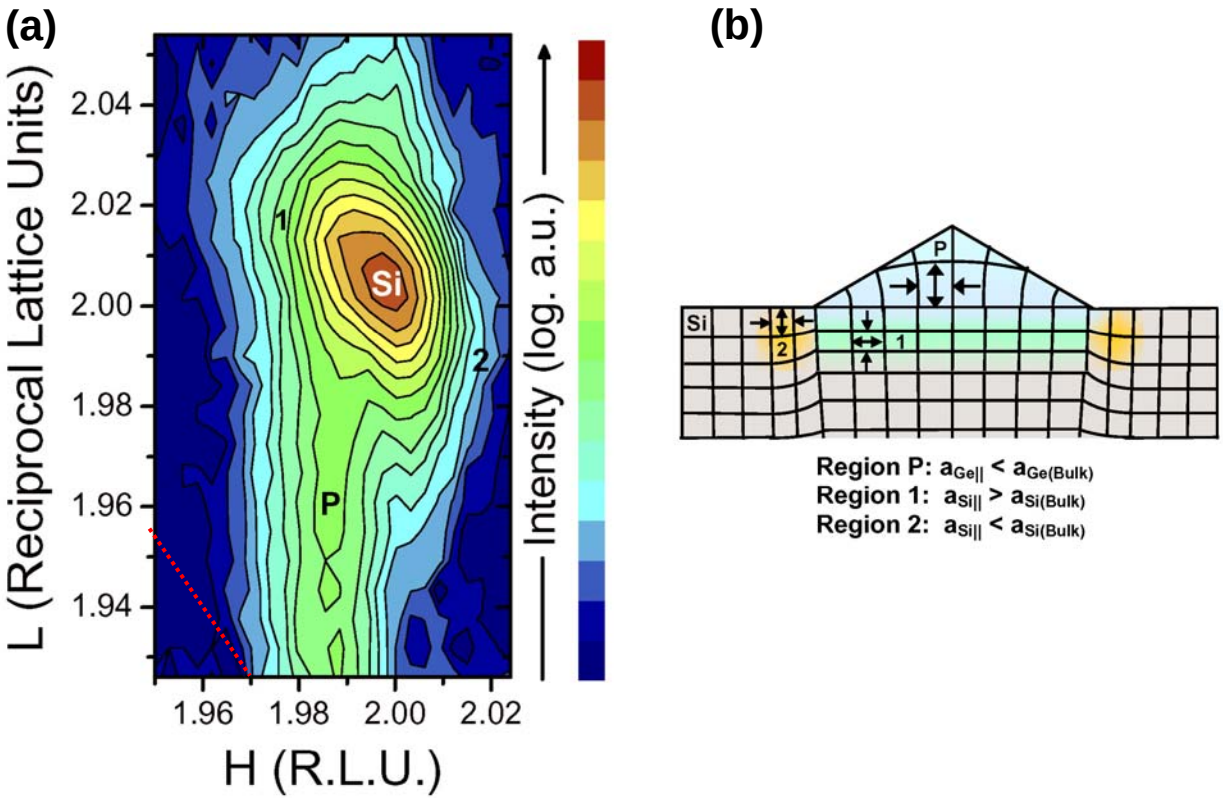

Fig. 2.16 – (a) Reciprocal space map of the (2 0.007 2) reflection for the pyramid sample. The x-ray scattering from pyramids is found close to the position labeled P. The red dashed line represents the pseudomorphic relaxation of a $Si_{0.4}Ge_{0.6}$ alloy. (b) Sketch of strain and lattice parameter in a pyramid.

2.8 Discussion

The strain relaxation inside Ge domes was mapped out in this chapter for pyramids and domes. The results of anomalous measurements close to the Ge K edge point at the fact that Si interdiffusion does take place at the temperatures used for island growth (600°C). By correlating strain and composition profiles inside these islands it was possible to directly quantify the reduction of elastic energy that occurs during the transition from pyramids to domes. This is probably the most significant driving force that governs shape

transition in this system. Although strain may aid, the precise mechanism assisting this interdiffusion process could not be clarified by these experiments and will be discussed in chapter 4. The asymmetric (2 0 2) reflection was mapped out for pyramids and domes in order to correlate in-plane and out-of-plane lattice parameters. These maps allow the observation of strained regions at the Si substrate, below and around the islands.

Chapter 3

3-Dimensional composition of Ge domes

3.1 Lateral Interdiffusion

Several independent studies using electron microscopy [Chaparro99, Liao02] and x-ray techniques – as seen in chapter 2 – have targeted the issue of Si interdiffusion into Ge islands grown on Si(001). Interdiffusion is a significant factor in determining the shape and size distribution of an island ensemble. All these experiments support the existence of a distinct SiGe vertical composition variation, with most of the Si concentrated at the base of the island. In addition, different growth conditions may produce distinct lateral profiles. A recent transmission electron microscopy study [Floyd03] reported no lateral composition variation in Ge:Si self-assembled domes. Evidence of lateral composition in annealed Ge:Si pyramids was inferred from selective etching indicating a Si-rich outer rim [Denker03], in agreement with the findings from buried InGaAs islands on GaAs(001) [Liu00, Cullis02].

The possibility of tuning a particular lateral composition profile via segregation, alloying, and enrichment [Tersoff98] is of great importance as it represents another degree of freedom in the design of self-assembled heteroepitaxial structures. Hence, the assessment of lateral composition profiles is important to identify the dominant growth mechanisms and model the confining potential of quantum dots. Understanding the contribution of kinetic and thermodynamic terms to island size and shape evolution is difficult to accomplish because the observed coarsening [Kamins99, Zhang03] could result from ripening or/and alloying.

Two samples were studied here. The growth parameters of sample A – CVD dome sample – were described in details in the precedent chapter. Sample B was grown by molecular beam epitaxy at a base pressure of 1×10^{-10} Torr at 700°C with 12 monolayers of Ge deposited in 12 min. Sample B has a monodisperse dome-shaped island ensemble with height 190±20Å and radius 510±40Å. The island densities of sample A and B are 7×10^{9} cm^{-2} and 2.1×10^{9} cm^{-2}, respectively. Figure 3.1 shows the island AFM height statistics for both samples, along with $1\mu m^2$ AFM scans (insets). The differences in the growth procedures were chosen so that alloying was enhanced for sample B.

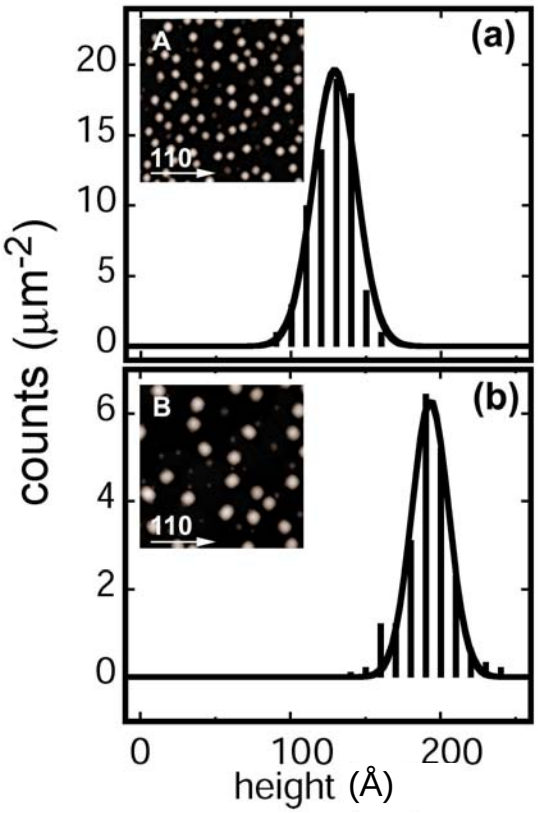

Fig. 3.1 – AFM statistics obtained from $1\mu m^2$ areas on (a) sample A and (b) dample B. The insets show $1\mu m^2$ AFM scans.

Following the method introduced in chapter 2 to evaluate the chemical composition, two x-ray photon energies were used. The first energy was at the Ge-K absorption edge (11103eV), where the complex atomic scattering factor of Ge is $f_{Ge} = 11.5 + 2i$. The second energy was 11005eV, far enough from the Ge edge to have a significantly different scattering factor $f_{Ge} = 16.2 + 0.5i$. The scattering factor for Si ($f_{Si} = 7.7 + 0.2i$) is essentially independent of x-ray energy in this region.

3.1.1 Complete analysis on sample A (CVD)

Initially the 3D composition mapping procedure was applied to sample A. As shown in figs. 3.2(a) and 3.2(b), complete diffuse scattering maps in q_r-q_a space near the (400) in-plane reflection were produced for this sample. In the two x-ray maps only the scattering power of Ge was changed; hence any intensity variation from one map to the other is associated with the presence of Ge atoms. The two reciprocal-space maps of figs. 3.2(a) and 3.2(b) allow several qualitative observations to be made. First, the broad profiles in the q_r direction of both maps indicate a large lattice parameter distribution within the domes. Second, the scattering intensity at 11005eV is significantly higher than at 11103eV, consistent with an energy dependent atomic scattering factor for Ge, i.e., anomalous scattering contrast. Finally, the subsidiary maxima present in both maps indicate a narrow island size distribution (see arrows), as expected from the AFM statistics.

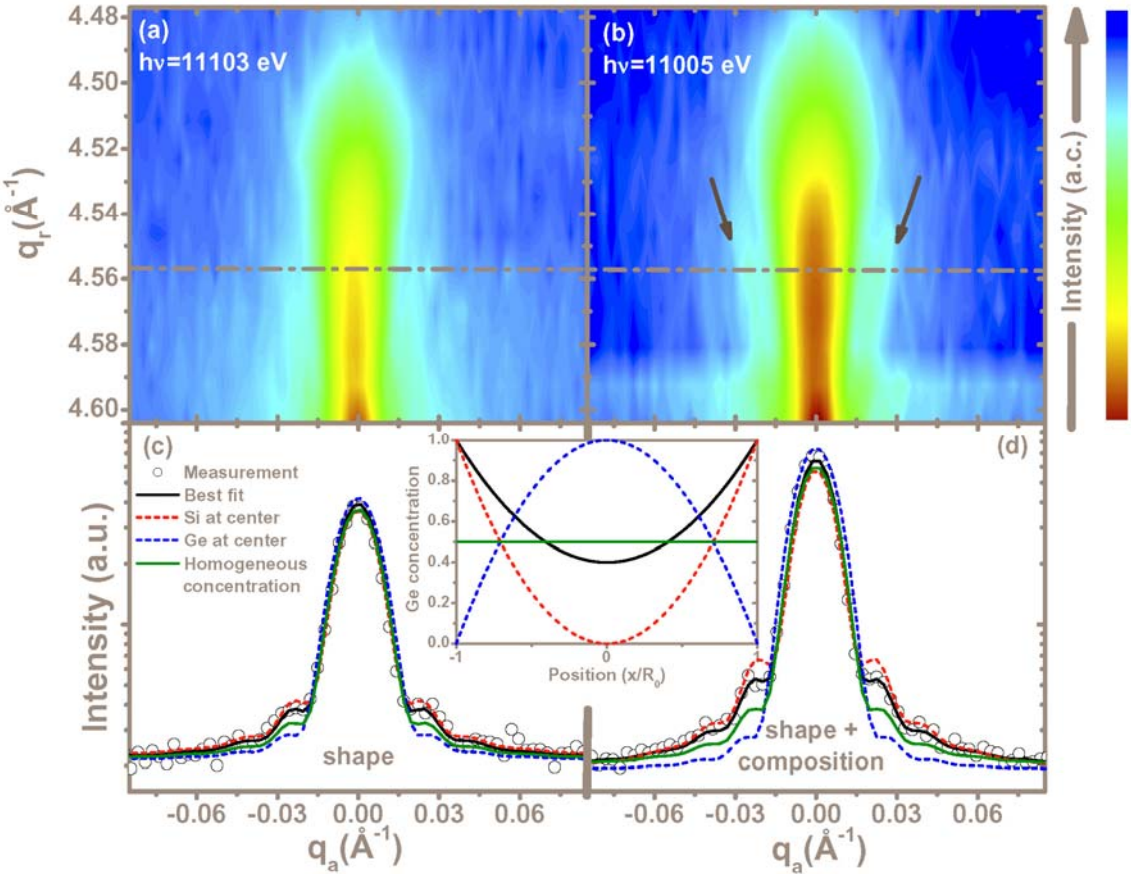

Fig. 3.2 – Diffuse scattering maps (400) surface reflection for Ge CVD domes (sample A) using two different x-ray photon energies (a) 11103eV (Ge K edge) and (b) 11005eV. The intensity color scale is logarithmic. (c) and (d) are angular scans at constant q_r corresponding to the dashed line in (a) and (b). Several fits corresponding to different lateral composition profiles are shown for the scans carried out at 11103eV (c) and 11005eV (d). The corresponding Ge concentration profiles are plotted in the inset.

Two angular scans corresponding to the horizontal dashed line marked in figs. 3.2(a) and 3.2(b) are shown in figs. 3.2(c) and 3.2(d). An analytical description of the shape of these equal-lattice parameter regions was used to reproduce the scattering profiles [Kegel01]. The form factor of discs (eq. 1.24) was chosen to fit the angular scans, revealing the cylindrical symmetry of this system (leading to a 3D reconstruction). This analysis is independent of a potential disk curvature [Kegel01], which is not assessed with the geometry used. The contribution of each Ge:Si disk with constant radius R to the x-ray scattering profile is given by

$$I(q_a,R)=\frac{I_0}{\pi^2 R^4\left|\langle f_{GeSi}\rangle\right|^2}\left|\int_0^{2\pi}\int_0^R e^{-iq_a r\cos\theta} f_{GeSi}(r)\,r\,dr\,d\theta\right|^2, \qquad (3.1)$$

where f_{Ge} and f_{Si} are the atomic scattering factors for Ge and Si, respectively, $f_{GeSi}(r) = C_{Ge}(r)f_{Ge} + [1 - C_{Ge}]f_{Si}$ is the effective scattering factor of the SiGe alloy at position r, and $\langle f_{GeSi}\rangle$ is the average atomic scattering factor. The form factor used in eq. 3.1 was modified with respect to eq. 1.24 to introduce the lateral composition. In an actual sample, equal lattice parameter regions of different islands may have different radii. The profile is then the sum of the intensities of independent scattering disks, $I(q_a) = A\int_{R_{min}}^{R_{max}} \pi R^2 I(q_a,R)\,dR$, where A is a constant independent of the x-ray energy, and R_{max}, R_{min} are the largest and smallest radii of equal-lattice parameter regions.

An angular scan at 11103eV (fig. 3.2(c)) is mostly sensitive to the shape of the equal-lattice parameter region, since it fits the cylindrical form factor with a homogeneous composition profile quite well and $f_{Ge} \approx f_{Si}$. In contrast, angular scans collected at 11005eV are chemically sensitive. At this energy, a Ge atom scatters approximately 4 times more effectively than a Si atom. The calculated profile for a uniform disk does not fit the angular scan data. The most likely reason for this difference is that the composition within the equal-lattice parameter region is non-uniform. Hence, a lateral variation of the composition profile was introduced into the fitting procedure. The simplest composition profile (i.e., fewest number of parameters) for an equal-lattice parameter disk that allowed the reproduction of the x-ray profiles was found to be

$$C_{Ge}(r) = C_{Ge}(0) + [C_{Ge}(R) - C_{Ge}(0)]r^2/R^2, \qquad (3.2)$$

where $C_{Ge}(0)$ is the Ge concentration at the disk center and $C_{Ge}(R)$ is the Ge concentration at its border, both varying between 0 and 1. A schematic representation of one disk with

lateral composition variation is shown in fig. 3.3. The profile was chosen to be Si-rich at the disk center and Ge-rich at its border.

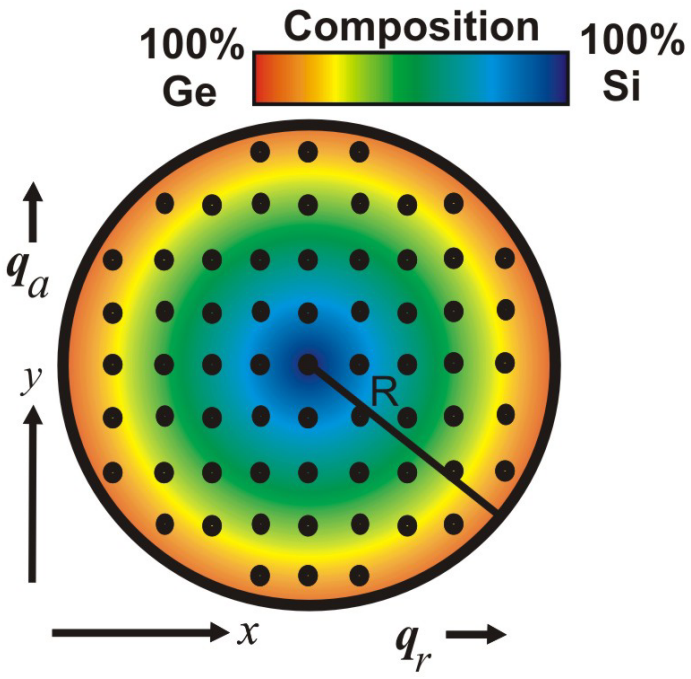

Fig. 3.3 – Skecth of a disk with lateral composition profile. In this case the disk center has pure Si and the border is pure Ge.

Several trial fits with different Ge profiles were performed for a selected pair of angular scans ($q_r \sim 4.56 Å^{-1}$), as shown in figs. 3.2(c) and 3.2(d). All homogeneous compositions produced nearly identical line shapes, as represented by the solid green curve in both figures. Although the calculated profile can be adjusted to match the central region well, there is a significant deviation at the subsidiary maxima. The sensitivity of this approach is demonstrated by comparing fits with a Si center and a pure Ge border, $C_{Ge}(R) = 0$, $C_{Ge}(0) = 1$; and with a Ge center and a pure Si border, $C_{Ge}(R) = 1$, $C_{Ge}(0) = 0$, which demonstrate how the lateral composition can change the calculated angular scan profiles. Although in the first case (dashed red line), the subsidiary maxima match the data well, the central peak is underestimated. The best fit was obtained for $C_{Ge}(0) = 0.4$ and $C_{Ge}(R) = 1.0$ and is represented by the black solid line.

Angular scans performed at different q_r positions, using the two selected x-ray energies, are presented in figs. 3.4(a) and 3.4(b). The minimum step size in q_r between angular scans can be estimated by $\delta q_r \approx 2\pi/R$, guaranteeing a small contribution from adjacent disks to the scattering intensity.

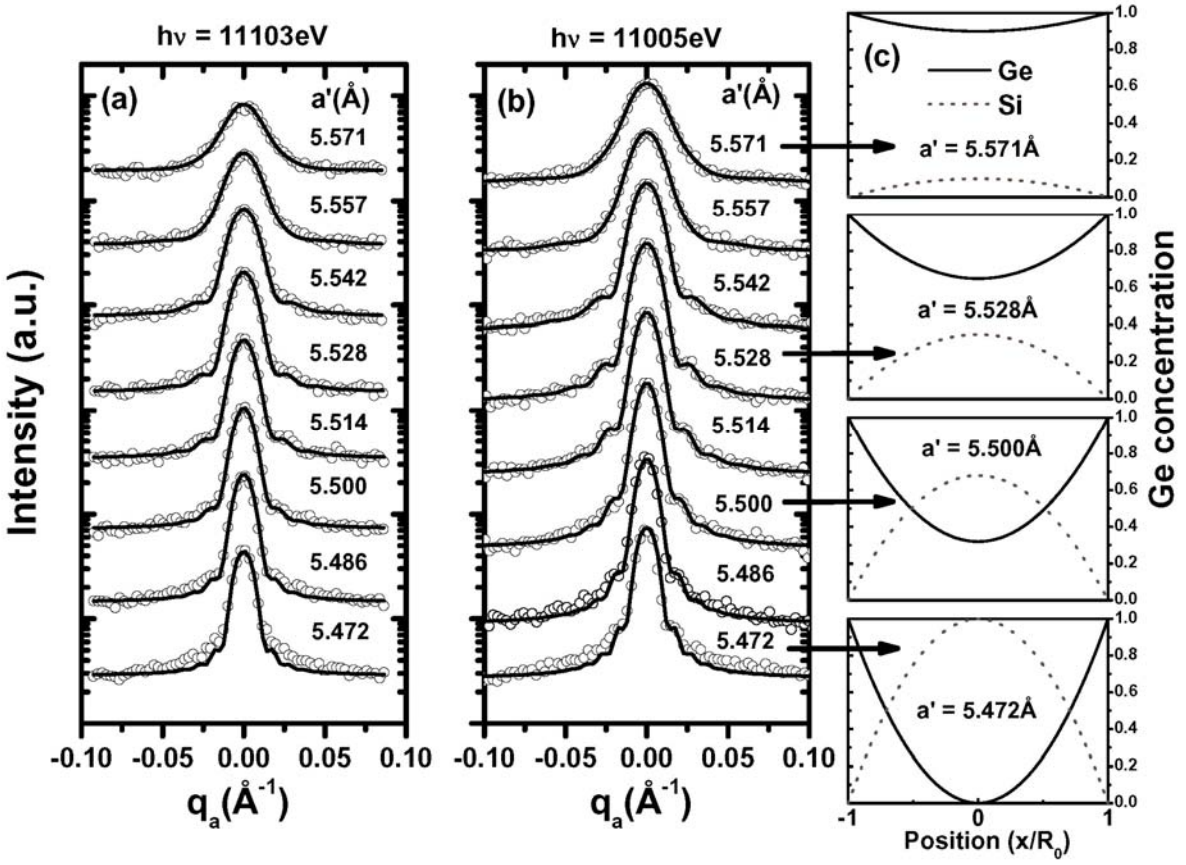

Fig. 3.4 – Angular scans performed on sample A Ge domes. In (a) and (b) the fits were done to extract the Ge composition profile suited to each equal-lattice parameter region. Some selected profiles are shown in (c).

The fits (solid lines) shown in figs. 3.4(a) and 3.4(b) were performed simultaneously for both energies using the $I(q_a)$ dependence on A, R_{min}, R_{max}, $C_{Ge}(R)$, and $C_{Ge}(0)$ as fitting parameters. In so doing the best chemical profile for each equal-lattice parameter region was extracted. Four selected Ge composition profiles corresponding to different lattice parameters (i.e., different heights within the islands) are shown in fig. 3.4(c).

All the profiles had a pure Ge border, while the Ge concentration at the center of the disks varied from 0 to 1 in moving from close to the base to the top of the domes. At the dome top, the smearing of the subsidiary maxima occurs because there, the equal-lattice parameter regions within the island ensemble have a broader range of radii. Towards the base, the subsidiary maxima sharpen, indicating a narrower range of radii, consistent with steeper facets. At the very base, we found the composition profile could not be fit by eq. 3.2. This is in part due to the overwhelming signal from the substrate scattering. Still a qualitative observation of a Si-rich core and non-pure Ge edge could be made. The

uniqueness of this method's ability to unambiguously determine the lateral chemical composition within a disk relies on the fact that once the x-ray photon energy is changed, only the atomic scattering factor of germanium changes. All other island structural parameters, i.e., the island local lattice parameter and radius, remain the same.

This 3D composition map must agree with the composition results obtained in chapter 2. Actually, the scattering intensity that is measured along the radial line ($q_a = 0$) corresponds to an average of contributions from all disks and the whole equal-lattice parameter regions located within them. Integrating the total Ge composition of each equal-lattice parameter region by taking the profiles that were used to fit angular scans of fig. 3.4 one obtains a vertical composition profile that matches very well the results of the last chapter. Fig. 3.5 shows a comparison between the 3D mapping method and the vertical interdiffusion obtained by radial scans analysis.

Figure 3.6(a) shows a side view of a central slice of the reconstructed 3D composition map for the domes of sample A. This map utilized an AFM profile of a typical island to provide the relationship between the equal-lattice parameter region height and radius to the parameters $C_{Ge}(R)$, $C_{Ge}(0)$, and R. A dashed line represents a 65% Ge composition alloy contour. To confirm the presence of the Si-rich core, a selective etching experiment designed to remove >65% Ge-rich alloys was performed, and AFM topographs were collected before and after the etch [Schmidt02]. Typical height versus length line scans over the center of the domes are shown in fig. 3.6(b), which qualitatively support the x-ray analysis.

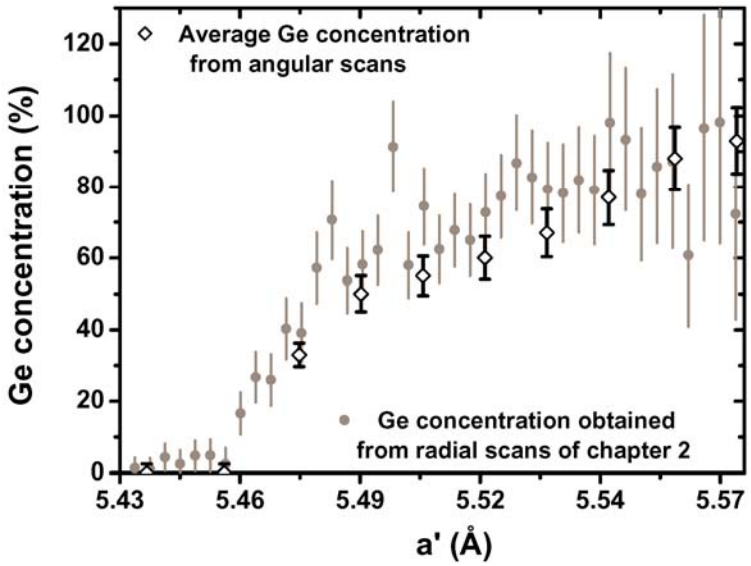

Fig. 3.5 –Vertical Ge concentration obtained by the 3D method (open symbols) and by radial scan analysis (solid dots – chapter 2).

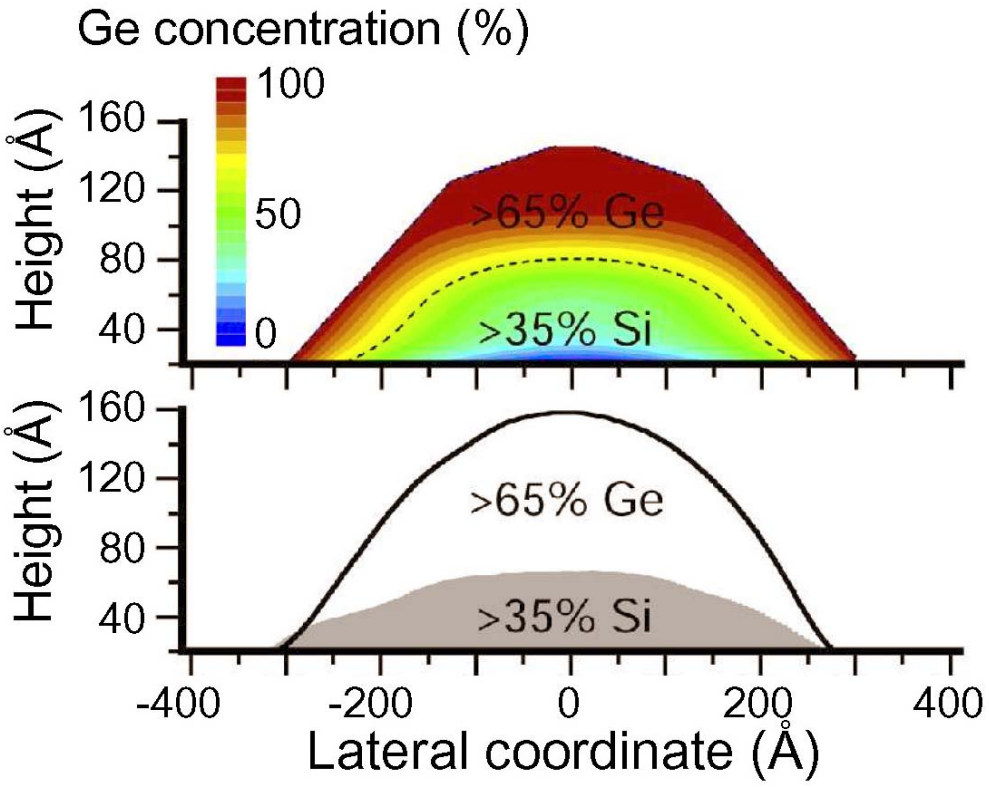

Fig. 3.6 – (a) Real space chemical composition map for Ge domes of sample A; (b) AFM line scans taken on two statistically average sample A Ge domes, before and after 31% H_2O_2 selective etch, evidencing the Si-rich core [Malachias03c].

3.1.2 3D composition analysis in sample B (MBE)

Figure 3.7 shows radial x-ray scans taken close to the (400) reflection for samples A and B [Magalhães-Paniago02] at the two different energies. It is clear that sample A contains a greater Ge fraction than sample B. The insets show angular scans are for samples A and B at the same Bragg condition ($q_r = 4.575 Å^{-1}$). Similarly to what has been done for sample A, the whole set of angular scans at the two energies was fitted using eq. 3.1. The result is shown in fig. 3.8.

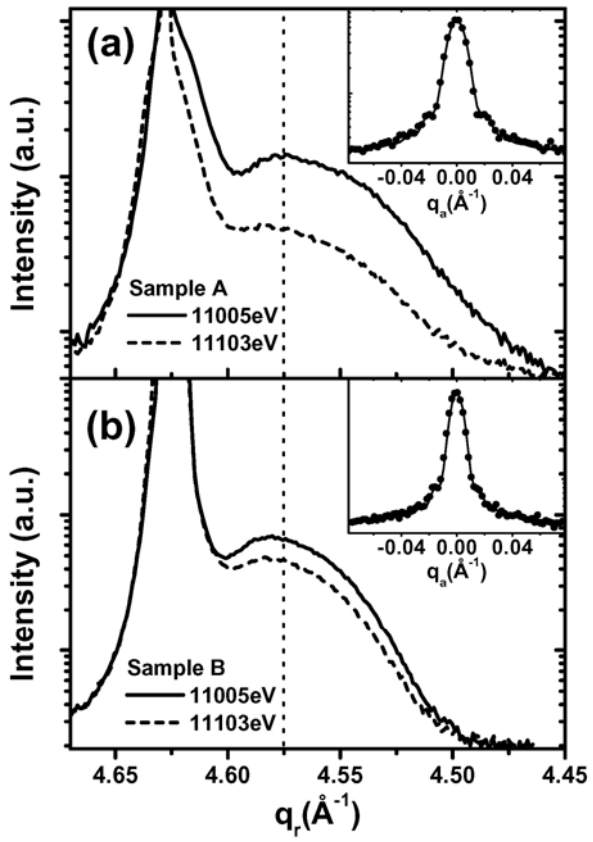

Fig. 3.7 – Radial and angular (insets) scans for (a) sample A and (b) sample B for 11005eV and 11103eV. The difference in amplitudes between the radial scans is related to the Ge content in the islands. Angular scans (insets) were fitted according to eq. 3.1 at $q_r = 4.575$Å^{-1}, corresponding to a constant lattice parameter of 5.494Å [MedeirosRibeiro05].

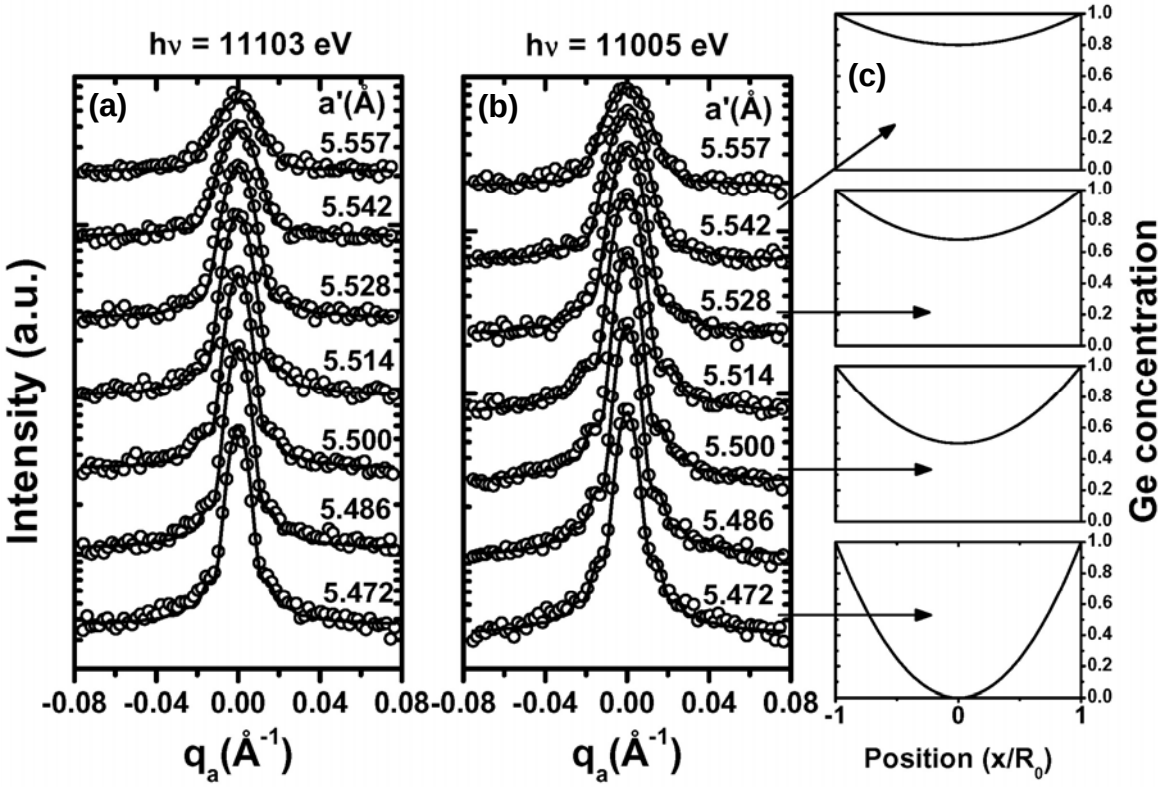

Fig. 3.8 – Angular scans performed on sample B Ge domes. In (a) and (b) the fits were done using eq. 3.1. Some selected profiles are shown in (c).

From the fits to angular scans of sample B a lateral composition profile was extracted for all layers [Malachias03c]. The composition map that results from this analysis is shown in fig. 3.9 together with the composition map of sample A. Sample B is significantly more alloyed than sample A, consistent with a lower growth rate and a higher growth temperature. A striking observation is the presence of the Ge-rich shell for both samples. The origin of this particular configuration may rise from two different processes: (a) bulk interdiffusion and (b) surface alloying and segregation during growth. Bulk interdiffusion as obtained for two-dimensional layers is a process that proceeds at a relatively long time scale [Zangenberg01]. Alloying during growth and segregation of Ge with the growth front are processes that can take place in times comparable to typical deposition times. In this case, the governing mechanism for mixing is surface diffusion (see chapter 4), which is much faster than bulk diffusion. The presence of a Ge-rich shell is related mostly to the lower Ge surface energy.

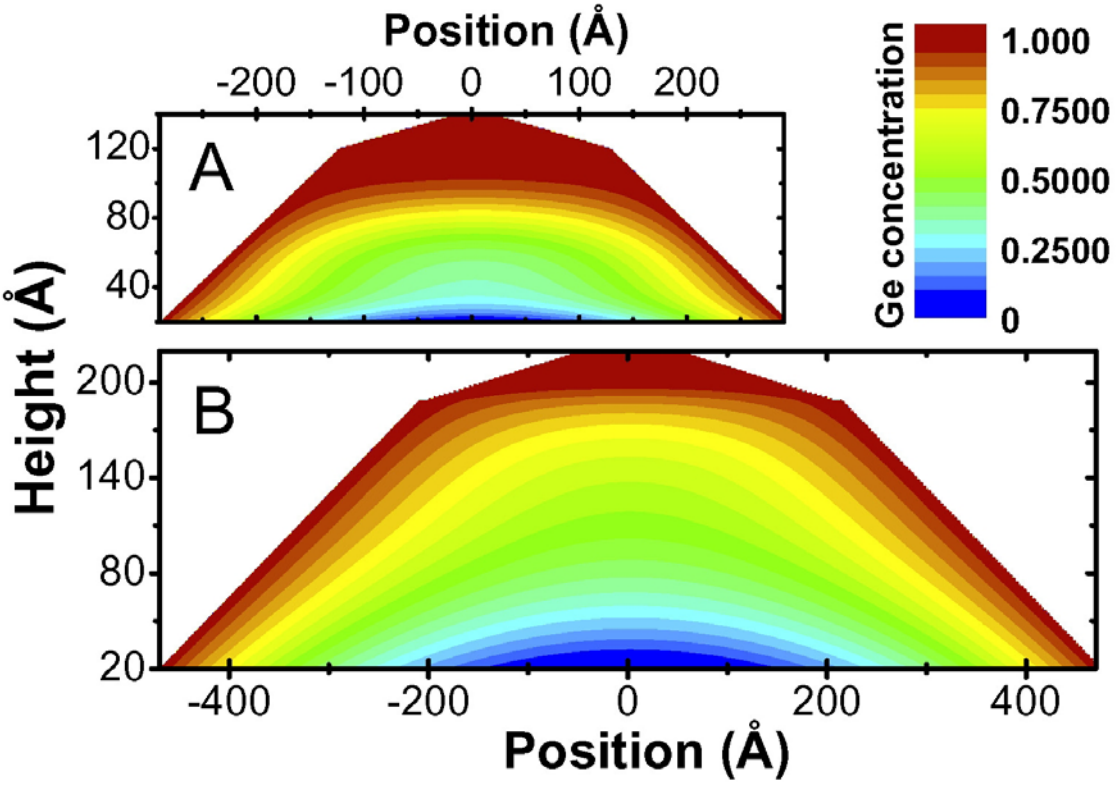

Fig. 3.9 – Composition maps for samples A and B.

3.2 Elastic energy maps

The elastic energy inside the islands can be evaluated at each point by [Tsao93] (see section 2.1.2, eq. 2.12)

$$u(r,z) = 2\mu\left(\frac{1+\nu}{1-\nu}\right)\varepsilon_{\parallel}(r,z)^2, \tag{3.3}$$

where μ and ν are the composition-dependent shear modulus and Poisson ratio of the SiGe alloy, and $\varepsilon_{\parallel}(r,z)$ is the in-plane strain for each point, defined by its distance r from the island center and its height z from the island base. The in-plane strain can be evaluated from the composition profile and the lattice parameter for each equal-lattice parameter layer, as done in chapter 2.

Figure 3.10 shows the elastic energy map for samples A and B. The first observation that can be readily made for sample B is the lowering of the average elastic energy due to enhanced alloying. The second observation is that, despite alloying, the elastic energy distribution within the islands is far from uniform. The Ge outer shell produces an elastic contribution that roughly scales with the surface area. The highest concentration of elastic energy is found at the island base edge, reaching values close to that of two-dimensional, uniformly strained pure Ge films on Si (about 30 meV/atom). We emphasize that for this particular region and for the technique utilized for the evaluation of the elastic energy, the lattice parameter was assumed to be constant, which is not correct when going from the island center to the island edge. Hence, the evaluated energy values represent a lower bound. Very close to the island edge, the substrate Si is compressively strained, having a smaller lattice parameter [Raiteri02]. Essentially, an average lattice parameter was used for each layer – a procedure that is quite accurate for regions distant from the substrate. For the layers close to the substrate, the lattice parameter near the island edge can differ from that near the center.

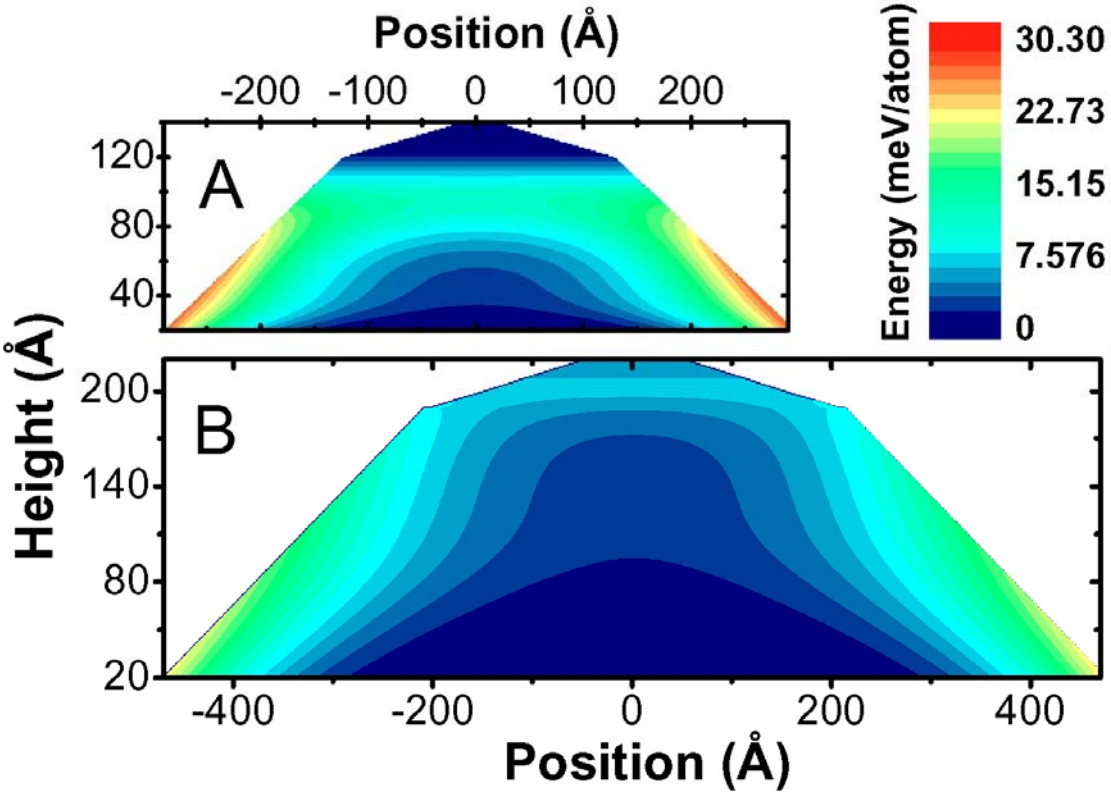

Fig. 3.10 – Elastic energy maps for samples A and B

The modeling of the thermodynamic equilibrium properties of island ensembles described by Shchukin et al. [Shchukin95] included energy terms that scale (per atom) with the island volume (constant), surface area ($V^{-1/3}$), and length ($V^{-2/3}$) which is related to the island edge. A preferred island size can exist depending only the volume and surface terms as shown in section 2.2 of the preceding chapter. However, the length term is the key for stability of a given island ensemble [Williams00]. The existence of this linear term has been questioned because of its supposedly negligible importance compared to the surface and volume terms. Having only the remaining two terms causes an island to ripen. The presence of the linear term can make the island ensemble stable against ripening. In order to have an optimum size of the islands (and a minimum size distribution) corresponding to the absolute minimum of the total energy per atom (u_{Total}) the surface term must be negative and the length term must be positive. u_{Total} is, then, written as [Williams00]

$$u_{Total} = u - \alpha^{4/3} \cdot V^{-1/3} + \beta \cdot V^{-2/3}. \quad (3.4)$$

In this case the appearing of high index facets causes u_{Total} to decrease proportionally to ($-V^{-1/3}$) while the highly strained belt around the island base, that scales linearly with the island circumference (i.e. proportional to $V^{-2/3}$). The behavior of the

surface and length terms is represented schematically in fig. 3.11(a). The total energy u_{Total} that corresponds to the sum of these terms and the constant per atom volume energy is shown in fig. 3.11(b); the minimum of energy can be seen in fig. 3.11(c).

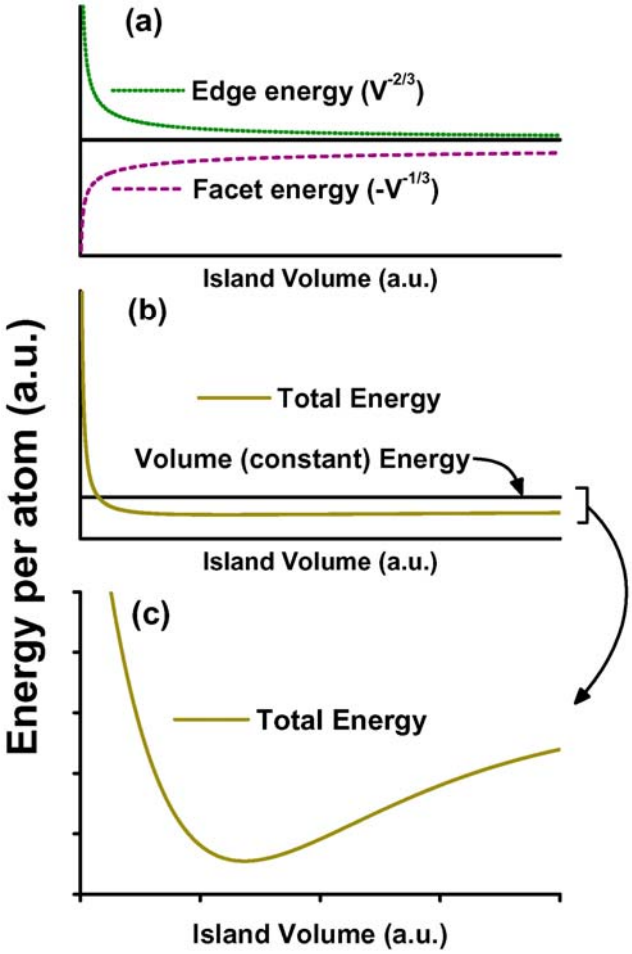

Fig. 3.11 – (a) Sketch of the edge and facet energy terms (per atom) of eq. 3.4 as a function of the island volume. (b) Variation of the total energy per atom (u_{Total} – eq. 3.4) with the island volume. (c) Expanded energy scale (zoom) of u_{Total} shown in (b); the minimum position defines the equilibrium size of the islands.

From the results presented in this work, we can infer that the strain belt around the island base provide dome islands with an equilibrium configuration that inhibits ripening. For the experimental conditions chosen for these experiments, we conclude that thermodynamics and kinetics can both provide the island ensemble with stability against ripening. The relative importance of each is difficult to evaluate, although the factors might be separated by experiments at varying deposition rates or by observations during growth.

As a final observation, we can compare the energy distribution for the two samples and that of the 2D Ge film. Figure 3.12 shows the energy histograms for samples A and B, which we can compare to the constant energy of 32meV/atom for the 2D Ge film. As

expected, the average energy on a per-atom basis decreases from sample A (12.8meV/atom) to sample B (8meV/atom). Only at the island edges does the stored elastic energy reach values close to the 2D limit, as seen from the maps of fig. 3.10.

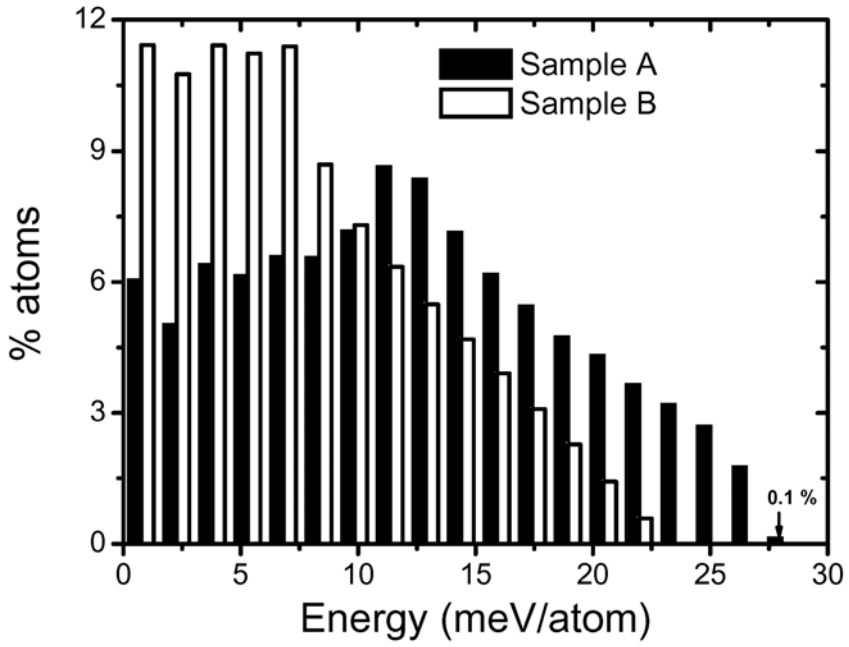

Fig. 3.12 – Elastic energy distribution within the domes for samples A and B

The total volumes and average Ge fractions for samples A and B are 7×10^5 and 3×10^6 atoms, and 77% and 70%, respectively. Taking into account the island densities, we conclude that the energy per unit area is about the same for both island samples and is lower than that of the 2D film, because of the significant alloying.

3.3 Discussion

In this chapter the three-dimensional Ge:Si composition profile was obtained in two dome samples. One possible explanation for the dome having a central Si-Ge alloy core and a nominally pure Ge shell can be given in the following way. Regions of the substrate under the island base (tensile stress) and at the island edge (compressive stress) exhibit maximum stress amplitudes, as shown by molecular dynamics simulations for pyramids [Yu97] and domes [Raiteri02]. Thus, the largest amount of stress relief occurs for the Si-Ge alloying in these regions. Since Ge is continually deposited during the growth of the

islands, the alloyed regions near the dome edges are continually buried under the newly arriving Ge as the edge moves radially outward. This gives rise to the shape of the alloyed region shown in figs. 3.6 and 3.9. In contrast, should one interrupt the Ge deposition while keeping the temperature constant, alloying at the edges takes place for both domes [Kamins99, Kamins98] and pyramids [Denker03].

The energy maps presented here provide clues to the reverse shape evolution of the system when Ge islands are capped with Si. It was found for this case that alloying start at the base edge, reducing the higher elastic energy portions of the islands. This behavior has been experimentally observed in initial stages of dome capping, with (105) facets forming at the island base upon Si deposition [Rastelli01].

Chapter 4

Atomic ordering in Ge islands on Si(001)

4.1 Ge/Si atomic ordering in thin films

The possibility of producing spontaneous order on a subnanometer scale has become one of the most important driving forces in nanoscience research during the last two decades. Stacked lipid membranes [Wong00], ordered arrays of quantum dots [Springholz98] and atomically ordered short-period alloy superlattices [Venezuela99, Li03] are examples of self-organization of atoms on very short length scales. In particular, for self-assembled quantum dots a variety of atomic-like behavior has been observed, like single electron charging and Pauli blocking. In order to further explore band structure engineering in these systems some crucial parameters have to be controlled. From the mesoscopic point of view, shown in the previous chapters, island shape and size distribution are the most important factors that must be managed. In the case of heteroepitaxial self-assembled islands, strain and composition may vary from one atomic layer to another. Hence, it is imperative to understand and control the growth conditions not only at the mesoscopic level but also at the atomic scale for rational quantum structures design.

Detailed near-surface studies have shown that spontaneous atomic ordering is observed in some semiconductor alloys [Venezuela99, Li03]. In particular, SiGe has been considered as a model for random alloys since long-range order cannot be produced by time-prolonged anneals in a wide temperature range (170ºC – 925ºC) [Hansen58]. The thermodynamical description of SiGe alloys considers that these two atomic species interact with each other in the same way as they do among

themselves [Tsao93]. This so-called “ideal solution” is extremely useful to understand SiGe alloy growth since it fits very well the solid-liquid alloy phase diagrams [Qteish88].

In 1985 *Ourmazd and Bean* [Ourmazd85] performed an electron diffraction experiment on $Si_{0.6}Ge_{0.4}$ superlattices grown by MBE at 550ºC on Si(001) and observed a clear evidence of atomic ordering. Besides the fundamental electron diffraction peaks they observed the occurrence of superstructure reflections such as (1/2 1/2 1/2), (3/2 1/2 1/2) and (3/2 3/2 1/2). Despite of trying different annealing procedures (at several temperatures, anneal times and cooling rates) the authors could not prevent ordering in the <111> direction. They deduced that the superposition of ordered domains with a pseudodiamond structure (later called RS1) could explain the width and shape of the superstructure reflections. The original electron diffraction pattern obtained by Ourmazd and Bean is shown in fig. 4.1(a). Figure 4.1(b) shows the pseudodiamod RS1 structure.

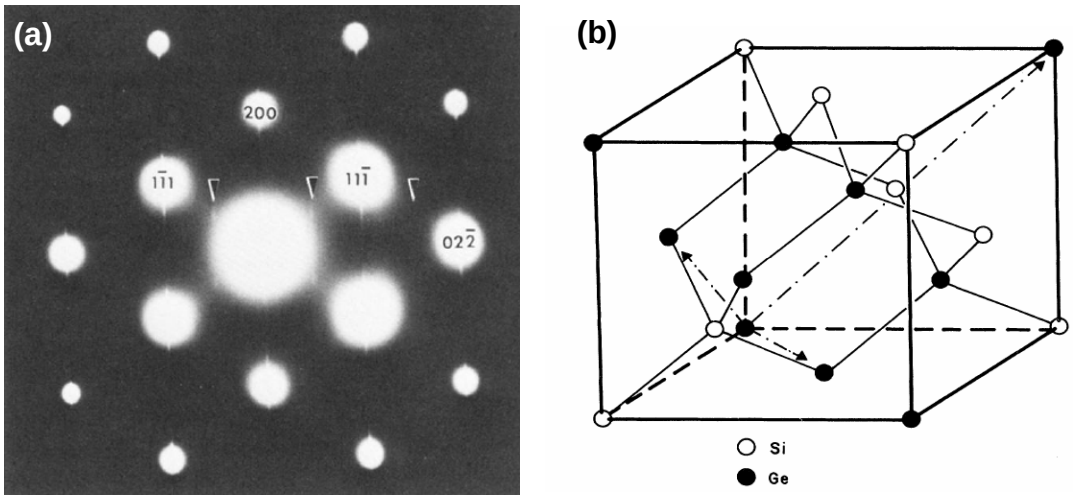

Fig. 4.1 – (a) Electron diffraction pattern of an ordered GeSi/Si superlattice near the [011] pole. Half-integral superstructure reflection peaks are indicated by arrows. (b) RS1 pseudodiamond structure of the ordered SiGe alloy as suggested by ref. [Ourmazd85].

After this first work several authors [Martins86, Littlewood86] tried to explain the ordering phenomena combining strain and thermodynamic arguments. While the hypotesis of strain driven ordering remained unclear, it was found that ordering should occur only for temperatures lower than ~150K. The proof that strain does not induce ordering appeared in a work by *Muller et al.* [Muller89]. Electron diffraction experiments were performed in a set of samples that were grown on alloy substrates, i.e. no strain, and superstructure reflections were also observed. This was also true for thick relaxed $Si_{0.5}Ge_{0.5}$ films [LeGoues90a]. In both works the growth temperature was in the

range between 400ºC and 500ºC and the substrates were oriented in the <001> direction. By analyzing and simulating the electron diffraction patterns they found a different pseudo-diamond structure (called RS2).

LeGoues et al. [LeGoues90b] showed unambiguously that ordering was not an equilibrium bulk phenomenon but it was tied to surface reconstruction. SiGe relaxed alloys films were grown on Si(001) with the typical 2x1 surface reconstruction and an artificially induced 1x1 reconstruction. No superstructure reflection was found at the 1x1 film although they had been observed at the 2x1 alloy. This result is shown in fig. 4.2. Films grown in Si(111) substrates also exhibited no ordering. They suggested an ordering mechanism that was linked to the lower energy of completely ordered <111> planes instead of reverting the registry by zigzagging. This <111> structure is energetically favorable over the arbitrary zig-zag domains by an energy difference of 80meV per dimmer.

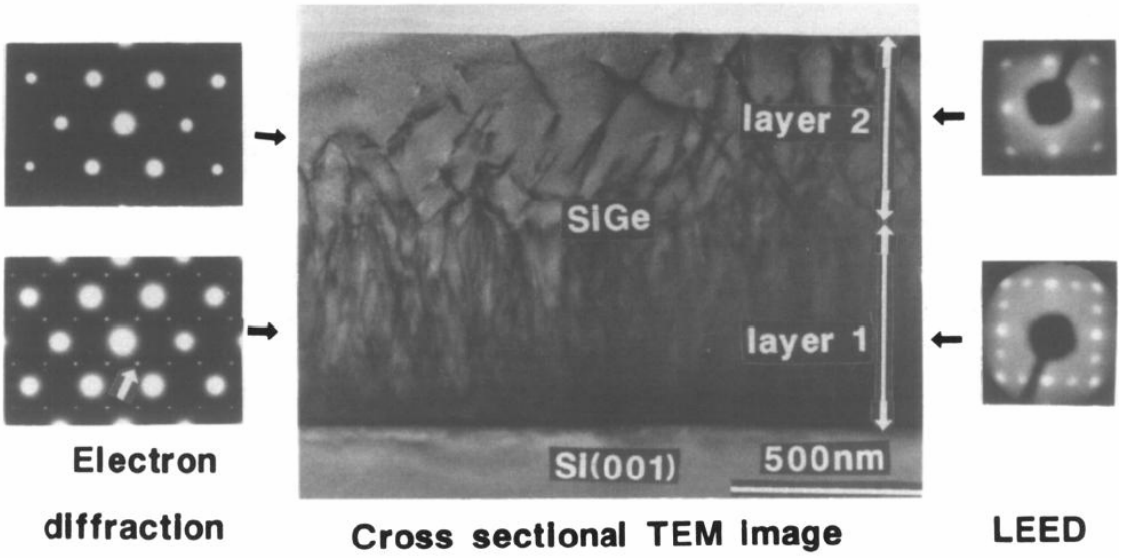

Fig. 4.2 – Cross sectional transmission electron microscopy (TEM) view of relaxed $Si_{0.5}Ge_{0.5}$ layers extracted from ref. [LeGoues90b]. Layer 1 was grown with 2×1 reconstruction while layer 2 was grown with 1×1 reconstruction. The low energy electron diffraction (LEED) patterns show the change in reconstruction. On the diffraction pattern the arrow indicates one of the extra spots due to ordering present in the bottom layer only.

A kinetic mechanism of SiGe ordering on Si(001) surfaces was later proposed by Jesson et. al. [Jesson91, Jesson92, Jesson93]. Since ordering is associated with dimmer formation a step-flow atomistic model was suggested to explain how SiGe order arises naturally at step edges during coherently 2D island growth without the need of atomic rearrangement after the deposition of a complete bilayer. Figure 4.3 shows a schematic view of a Si(001) substrate. In this [110] projection

the dimmers are oriented perpendicular to the picture plane, i.e. each point in fig. 4.3 corresponds to a Si or Ge dimmer in the [1 -1 0] direction. The growth will proceed in the [110] direction initially replacing the Si rebounded dimmer of (I) by a Ge dimmer in the perpendicular direction. The second Ge dimmer in this structure will be deposited between the two Si atoms of step (II). Despite of being kinetically frozen at low temperatures, the configuration shown in (III) is energetically unfavorable due to the high stress on the Si marked dimmer and the presence of unsaturated bounds at the step edge in the right. The next Si atom (in the right, just after the second Ge dimmer) is located in a suitable site for a possible adatom-substrate exchange mechanism driven by total-energy minimization. The interchange of Si and Ge atoms at this step edge (see arrow in step III) replaces a Si dangling bond by a less energetic Ge one. A driving force of the order of 0.5eV was estimated for this change [Jesson91], leading to the configuration shown in (IV) that is more stable than (III). Since this exchange has a probability to happen two different types of Ge-rich (α, β) and Si-rich (γ, δ) sites will arise. The first kind of sites – Ge-α and Si-γ – is related to originally preferential sites for substrate Si and deposited Ge dimmers. Ge-β and Si-δ sites correspond to dimmers that have been rearranged by the exchange mechanism. The growth front continues along the [110] direction, alternating Si and Ge atoms by repeating steps I-IV until the first ordered layer is complete. The next layers will grow following the <111> ordered direction which was proven to be less energetic over an arbitrary vertical ordering [LeGoues90b]. This model explains very well the beginning of the ordering process but the explanation of the mechanism of Si incorporation inside higher layers is still lacking. In order to clarify the complete ordering mechanism in-situ x-ray diffraction, electron diffraction or scanning tunneling microscopy measurements (that were not performed here) must be done during Ge growth.

A complete x-ray investigation about possible $Si_{0.5}Ge_{0.5}$ structures in thin films was performed by *Tischler et al.* [Tischler95]. The crystallographic measurements of the superstructure reflection intensities lead to a modified RS2 ordering model (called RS3), with two different structures: the main <111> ordered structure and a secondary structure ordered along the <100> direction. More recently, metastable ordered structures were discovered near the surface [Reichert99]. It is remarkable that all works were done in alloy samples and the kinetic origin of ordering has been continuously corroborated [Kinetic90, Jesson91, Jesson93, Kesan92, Reichert99].

Despite of all the work done the possibility of atomic ordering for deposition of pure Ge on Si(001) was neglected due to island formation. In this chapter basis forbidden reflections were

measured in Ge:Si(001) islands to unambiguously determine the existence of an ordered alloy phase inside these nanostructures and at the wetting layer (WL).

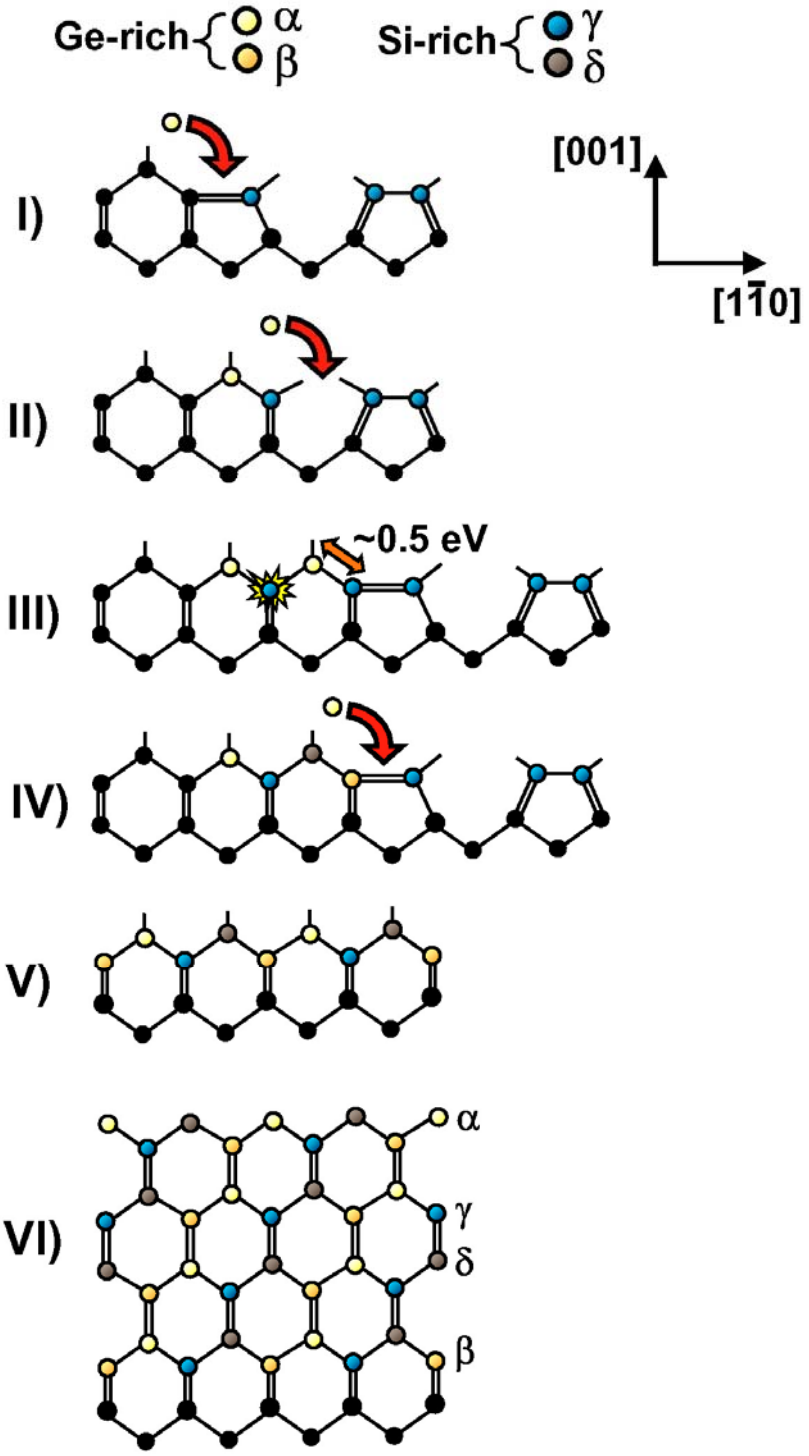

Fig. 4.3 – SiGe atomic ordering mechanism steps as proposed by ref [Jesson91]. Si rich sites are re presented by dark colors: Si-γ - blue and Si-δ - grey. Ge rich sites are denoted by Ge-α (yellow) and Ge-β (orange). The explanation of the order mechanism can be found in the text of the preceding page.

4.2 Sample characterization using Raman spectroscopy

The samples investigated in this chapter were grown on Si(001) substrates by solid source molecular beam epitaxy [Schülli05] at temperatures of 620ºC (sample A), 700ºC (sample B), 750ºC (sample C) and 840ºC (sample D). The amount of deposited Ge for samples A to D in monolayers (ML) is, respectively, 6.7ML (A), 11ML (B), 11ML (C) and 6ML (D). Atomic force microscopy measurements showed that dome islands were formed with monodisperse size distributions in all samples. The average Si interdiffusion inside these samples was studied by x-ray anomalous scattering in reference [Schülli05]. The Ge average content inside the islands for each sample was found to be 0.62 for sample A, 0.48 for sample B, 0.45 for sample C and 0.22 for sample D.

In order to qualitatively evaluate interdiffusion and short-range ordering in these samples a Raman scattering measurements were performed. The samples were excited by a 5145Å Ar laser set to a power of 8mW at the sample surface. The raman spectra were recorded with a triple grating spectrometer. This experiment essentially reveals the existence and relative abundance of Ge-Ge and Si-Ge bonds inside the islands. Fig. 4.4 shows the Raman signal in a range between 200 and 600 cm^{-1} from the four samples and a Si substrate. The Ge-Ge, Si-Ge and Si-Si vibrational modes are observed around 300, 400 and 500 cm^{-1}, respectively.

A qualitative analysis can be draw by comparing the intensities of the Si-Ge peak (around 415cm^{-1}) for all samples. This intensity is roughly proportional to: (a) interdiffusion that introduces Si atoms inside the Ge islands and; (b) short-range atomic ordering that maximizes the number of Si-Ge bonds [Lockwood87, Finkman2001]. From the measurements of fig. 4.4 one observes an increase in the Si-Ge mode intensity with the growth temperature comparing samples A and B essentially due to the larger coverage and higher degree of intermixing. However, the intensity of this raman peak decreases for growth temperatures higher than 700ºC, most notably by comparing samples B and C where the same amount of Ge (11ML) was deposited. This suggests a dependence of the short-range ordering degree with the growth temperature as observed by electron diffraction experiments [Kesan92]. Since sample B exhibited the strongest Si-Ge raman peak it was chosen for a complete analysis using x-rays.

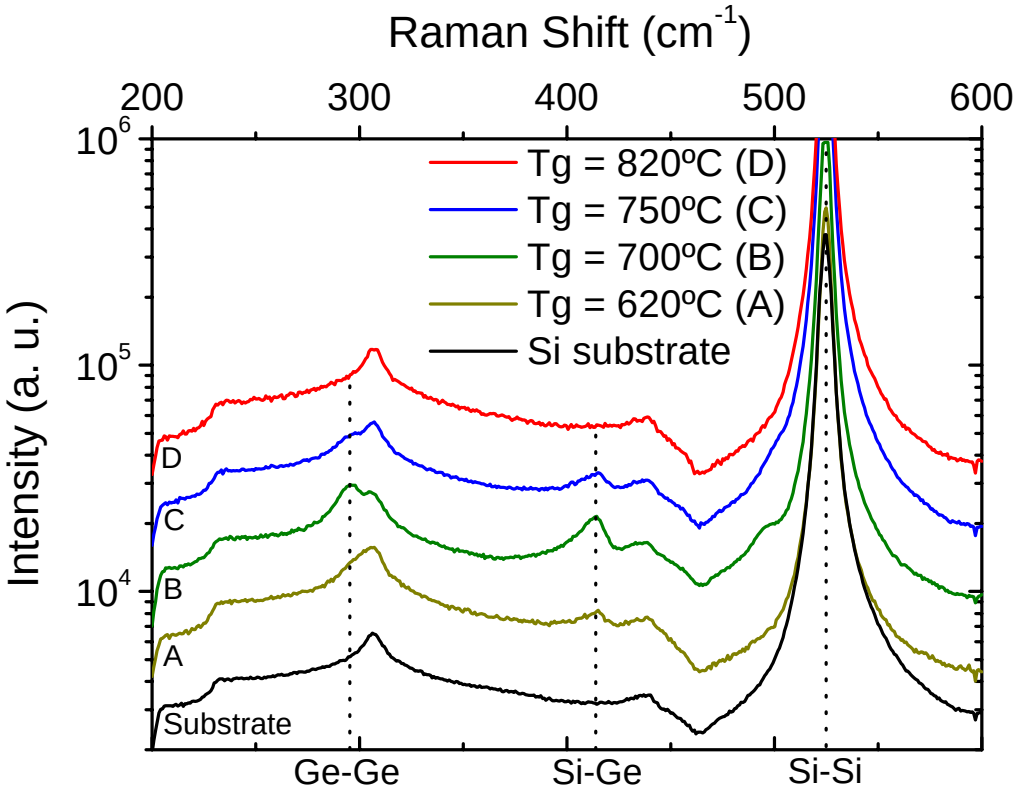

Fig. 4.4 – Raman spectra of a Si(001) substrate and samples A, B, C and D. The Ge-Ge and Si-Ge Raman peaks are indicated by dashed lines.

4.3 X-ray measurements in sample B

The X-ray measurements shown in this chapter were performed in grazing incidence geometry at Beamline ID1 of the European Synchrotron Radiation Facility. The incident angle was set to 0.17°. X-ray scattering was collected in a range of exit angles from 0 to 1.5° by a position sensitive detector. The X-ray photon energy was set to 8.0 KeV. Reciprocal space q_r-q_a maps were recorded next to surface fundamental and superstructure Bragg reflections.

A radial scan along the [100] direction near the (400) Si reciprocal lattice point is shown in fig. 4.5(a), where the q_r-axis was directly converted into the in-plane lattice parameter (upper scale). Next to the Si peak at 5.431Å one observes a broad intensity distribution up to 5.6Å indicating that the lattice parameter, which was initially constrained to the Si value, relaxes continuously with increasing height inside the islands. A rather unexpected result is obtained when the scattered intensity is measured in the vicinity of the (200) reflection, which is forbidden for pure Si and pure

Ge crystals. Under this Bragg condition, scattered intensity is expected only when the SiGe alloy is at least partially ordered. Fig. 4.5(b) thus represents the first evidence that long-range ordering is present in this system. While the total Ge relaxation reaches 5.60Å (fig. 4.5(a)), the ordered alloy is restricted to lattice parameters between 5.44 and 5.54Å. The narrow peak observed at 5.431Å is generated by the ordered SiGe wetting layer, which is pseudomorphically strained to the Si in-plane lattice parameter.

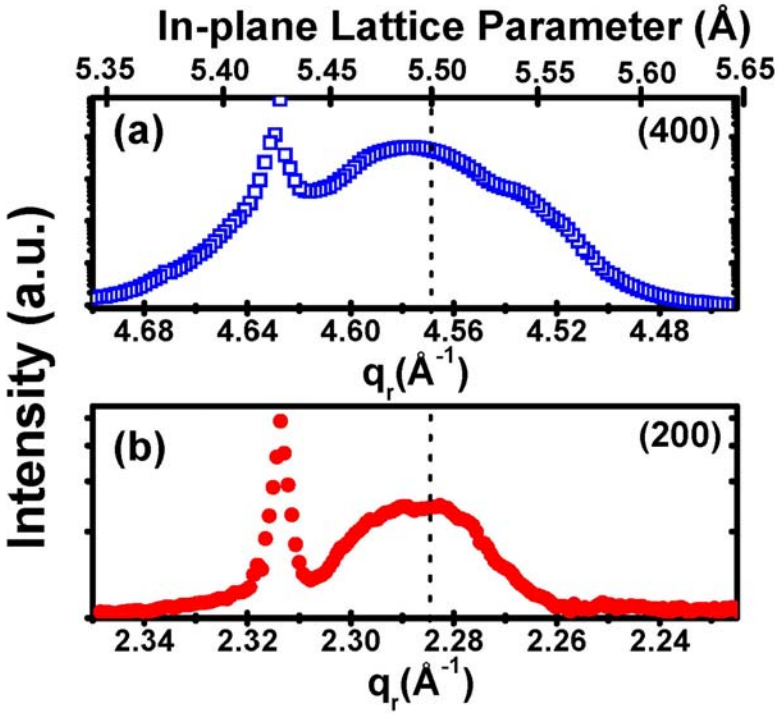

Fig. 4.5 – Radial scans along q_r in the vicinity of (a) Si (400) reflection (open squares) and (b) Si (200) reflection (solid circles) for sample B. The upper scale indicates the in-plane lattice parameter.

The strain information is only partially revealed by radial θ-2θ scans and a complete analysis relating the region which is constrained to a given lattice parameter and its position inside an island depends on the information of angular scans. In this case it is necessary to know the form factor of an iso-lattice parameter region of the island which is given by integrating the charge density inside the scattering object [Kegel99].

Performing an angular scan for a fixed lattice parameter (dashed lines in fig. 4.5(a) or 4.5(b)), one can probe the corresponding Fourier transform of a region with constant lattice parameter. One angular profile close to the (400) reflection is shown in Fig 4.6(a). It exhibits a broad peak centered at $q_a = 0$ and subsidiary maxima, indicating the finite size and narrow size

distribution of these constant-lattice parameter regions [Kegel99]. The lateral size of this region is evaluated from the q_a-peak width (using e.g. eq. 1.27), which is inversely proportional to the lateral size L of this region in real space.

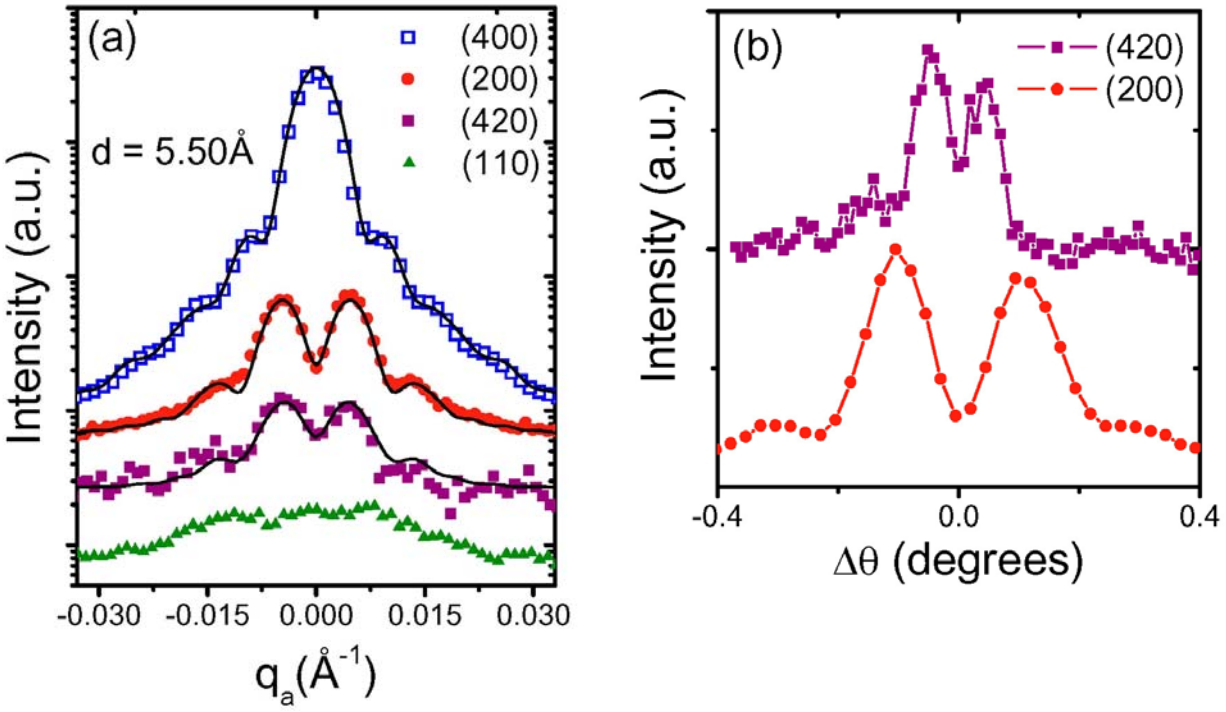

Fig. 4.6 – (a) Angular scans for sample B performed at 5.50Å at four reflections: (400) – open squares, (200) – solid circles, (420) – solid squares, and (110) – solid triangles. The (400) intensity was divided by a factor 100 when compared to the (200). (420) and (110) angular scan intensities were multiplied by 2 when compared to (200). (b) (200) and (420) angular scans seen in (a) plotted in angular space.

In contrast to the (400) reflection, an angular scan performed at the (200) reflection at q_r = 2*2π/(5.50Å) yields a very different profile as seen in figure 4.6(a). A pronounced minimum is observed at q_a = 0, which cannot be generated by structures that are interfering constructively, i.e., such a profile can only be modeled by introducing anti-phase boundaries between domains inside the islands (using e.g. eq. 4.3).

Other superstructure reflections consistent with reference [Tischler95] were also measured. Angular scans for three superstructure reflections at a fixed lattice parameter d = 5.50Å are shown in fig. 4.6(a). At the (420) and (200) reflections the anti-phase pattern is clearly observed. The angular scan at the (110) reflection reveals a superposition of lineshapes due to the contribution

from domains in in-phase and out-of-phase conditions. The angular scans at the (420) and (200) reflections have different angular distances in real space as shown in fig. 4.6(b), excluding the possibility of scattering by two or more rotated structures.

Two distinct form factors were used here. At the (400) fundamental reflection all material inside a Ge dome will scatter since its intensity is proportional to the square of the sum of the atomic scattering factors of Ge/Si atoms [Warren69, Malachias03c]. Since the surface diffraction technique used here is fairly unsensitive to the shape of the nanostructures one can consider, for simplicity, that the islands have a square-shaped section. In this case the scattered intensity for an island with M planes parallel to the surface is given by eq. 1.22 [Warren69]

$$I(q_r, q_a, q_z) = \frac{I_0}{M^2 N^4} \left| \sum_{j=0}^{M-1} \left[\sum_{m=1}^{N_j} e^{imd_j q_r} \cdot \sum_{n=1}^{N_j} e^{ind_j q_a} \right] \cdot e^{ih_j q_z} \right|^2 , \tag{4.1}$$

where N_j, d_j and h_j are the number of atomic lines, lattice parameter and height of layer j. Thus, the side length L_j of one layer is given by $L_j = N_j d_j$.

The result of eq. 1 in the angular direction (constant q_r) at a fixed q_z can be simplified into e.g. eq. 1.23 [Warren69, Kegel99]

$$I(q_a) = \frac{I_0}{L^2} \left| \frac{\sin\left(L/2\, q_a\right)}{\sin(q_a)} \right|^2 . \tag{4.2}$$

In contrast to the (400) reflection, the shape of an angular scan performed at the superstructure (200) reflection will depend on the existence of an ordered SiGe alloy. If the iso-lattice parameter region is completely ordered the anguler scan will exhibit an intensity profile given by equation 2. However, an atomic layer may be divided into smaller ordered regions separated by anti-phase boundaries. These boundaries are generated by mistakes in the in-plane atomic sequence. Instead of a layer with an atomic sequence such as …Si-Ge-Si-Ge-Si-Ge…, a broken sequence of atoms (e.g., …Si-Ge-Si-Si-Ge-Si…) is formed. Considering that the lattice parameter is nearly constant for a plane parallel to the substrate, the Si-Si or Ge-Ge stacking faults lead to phase inversions in the x-ray wave [Li03, Warren69]. To calculate the scattering amplitudes in this case one must introduce an inversion term $e^{i\pi}$ at each boundary, describing the phase shift between one domain and its neighbor. For an island with M atomic planes divided in four domains the scattered intensity can be calculated from [Li03, Warren69]

$$I(q_r,q_a,q_z) = I_{Max}\frac{2sin^4\left(\pi/4N\right)}{3}\left|\sum_{j=0}^{M-1}\left\{\sum_{m=0}^{N_j-1}e^{imd_jq_r}+e^{i\pi}\cdot\sum_{m=N_j}^{2N_j-1}e^{imd_jq_r}\right\}\cdot\left\{\sum_{n=0}^{N_j-1}e^{ind_jq_a}+e^{i\pi}\cdot\sum_{n=N_j}^{2N_j-1}e^{ind_jq_a}\right\}\cdot e^{ih_jq_z}\right|^2, \quad (4.3)$$

where N_j is the number of atoms within each domain at layer j.

The presence of anti-phase boundaries in islands is evident only in angular scans since in the radial direction the measured intensity results from a convolution between strain, domain size and antiphase relation between them. This effect produces the well-known broadening of the superstructure peaks [Li03, Warren69]. Similarly to eq. 4.1, at a fixed q_r and q_z, eq. 4.3 can be simplified to [Warren69]

$$I(q_a) = I_{Max}sin\left(\frac{\pi}{2Nd}\right)\left|sin(Ndq_a)\cdot\frac{sin(Ndq_a)}{sin(q_a)}\right|^2. \quad (4.4)$$

Eqs. 4.3 and 4.4 were normalized by the maximum measured intensity (I_{Max}) at $q = \pi/(2Nd)$ since $I(q = 0) = 0$ for an ordered crystal with anti-phase boundaries.

The resulting function of eq. 4.4 represents a layer of atoms with local lattice parameter d divided into two domains with the same domain size Nd. The angular intensity shape resulting from equations (4.2) and (4.4) are shown in fig. 4.7.

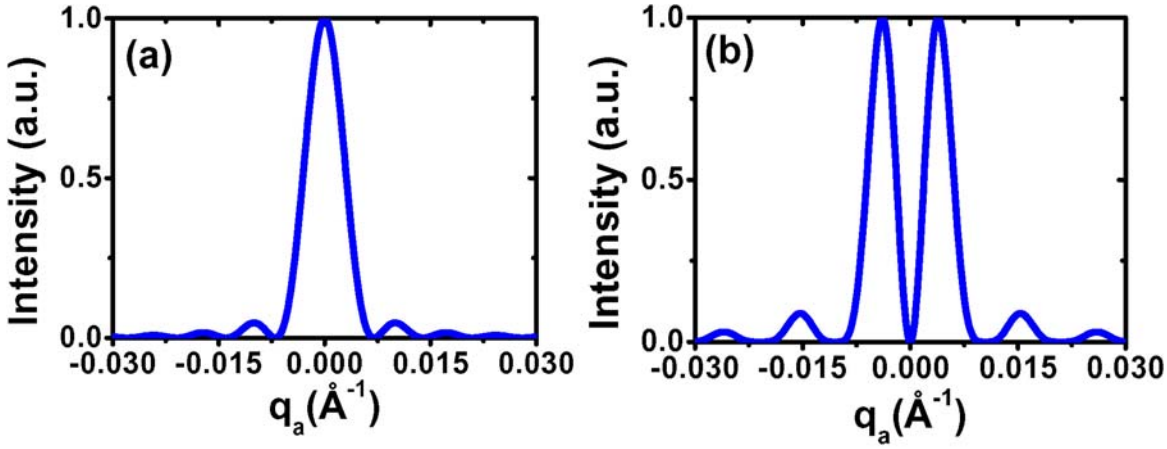

Fig. 4.7 – Form factors for (a) a 900Å atomic layer (eq. 4.2) and (b) two domains with 300Å each one (eq. 4.4).

In order to explain angular scans observed at the superstructure reflections discussed above it is necessary to understand the atomic arrangement for a SiGe ordered alloy. The schematic crystal structure of figure 4.8 follows the RS3 model of Ge-rich (α, β) and Si-rich (δ, γ) sites proposed in references [Jesson91, Jesson93] and [Tischler95]. According to these references, Ge atoms

deposited on a (2×1) reconstructed Si(001) select specific sites and produce rows with the same atomic species along the [1 1 0] or [1 -1 0] direction. Anti-phase boundaries are formed when they are shifted by one atomic distance in the direction perpendicular to these rows. At this intersection an anti-phase boundary in the [010] direction can be created, as represented by the red lines in fig. 4.8. The model used to fit the (200) and (420) angular scans in fig. 4.6(a) is described by eq. 4.3 and represented as four square-shaped domains with opposite phases. The model is consistent with this 4-fold symmetry, since the scattering pattern measured for reflections (200) and (020) exhibited the same intensity distribution. Each ordered domain is then surrounded by domains with opposite phases. Anti-phase boundaries are always located in between domains since only two atomic species are involved. Changing one atom from Si to Ge (or vice-versa) in an ordered atomic row will always generate an anti-phase configuration. In this structural model the anti-phase walls are always located along the <100> directions. For this reason the angular scans that have anti-phase profiles are always found along these directions while angular scans performed in the <110> directions result in a sum of scattering intensities from in-phase and out-of-phase atomic domains.

Superstructure reflections such as (100), (210) and (300) – that would indicate the presence of different ordered alloy phases – were not observed. Half-integral reflections such as (1/2 1/2 1/2) and (3/2 3/2 3/2), which could indicate ordering along the <111> direction as observed in 2D SiGe alloy layers [Tischler95], were also not observed. *LeGoues et. al.* [Kinetic90] have found that, at high growth temperatures such as the one used in our experiment, the vertical registry is lost since there are 4 possible <111> ordering directions.

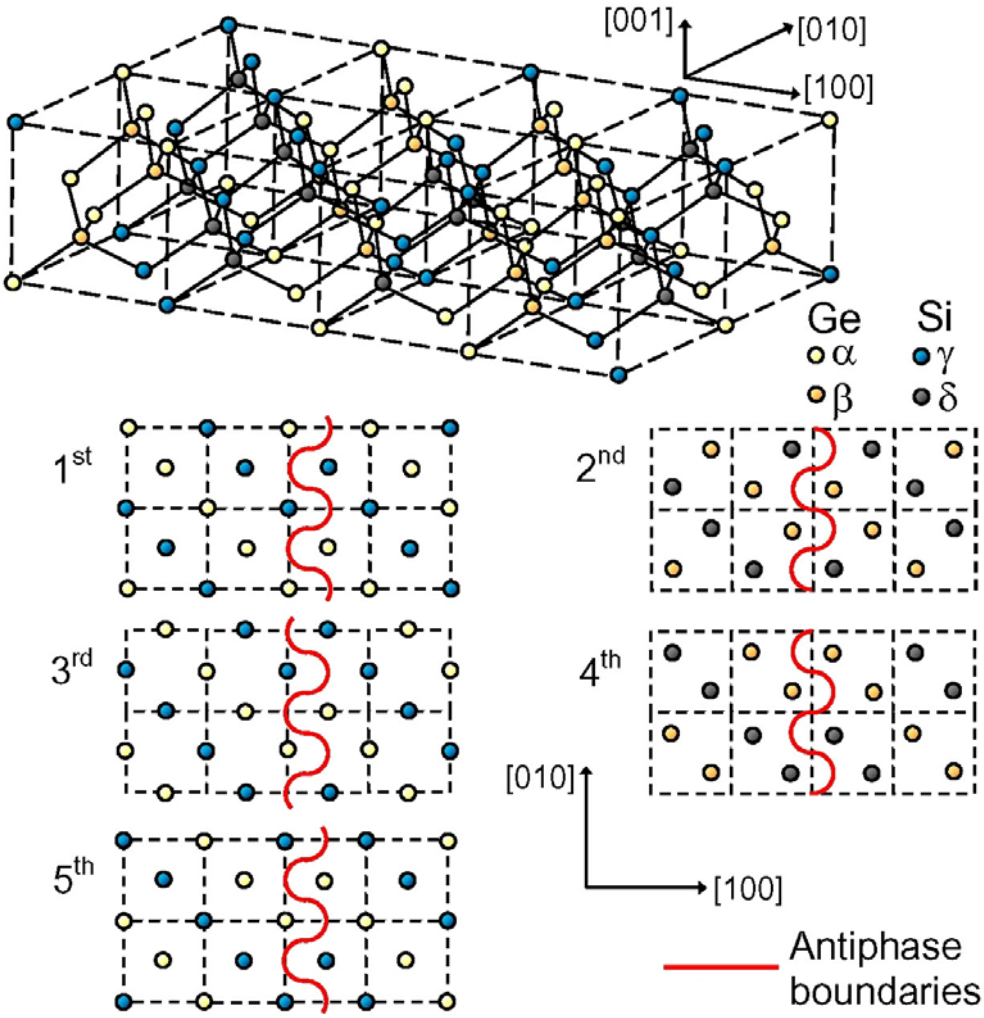

Fig. 4.8 – Schematic representation of the Si/Ge atomic ordering arrangement in the RS3 model. Ge-rich sites (α and β) correspond to yellow and orange atoms while Si-rich sites (δ and γ) are represented by gray and blue atoms. Five atomic layers along [001] are shown to indicate anti-phase boundaries in each layer. For all layers the darker atoms are Si-rich sites. This structural model is consistent with measurements of fig. 4.6(a).

The complete q_r/q_a measured intensity map in the vicinity of the Si (200) reflection is shown in fig. 4.9(a). Spanning from q_r values higher than the Si position (q_r= 2.314Å^{-1}) up to q_r=2.27Å^{-1} two different structures are seen. In the region of the strained alloy (q_r<2.31Å^{-1}) the double peak structure along q_a is always present. For lower q_r the width of this profile slightly increases, indicating a decreasing lateral size of the domains in real space. A weak narrow peak is seen exactly at the Si (200) position, indicating that the wetting layer (WL) is partially ordered, but without establishing anti-phase boundaries. This evidences that alloying and ordering begin as soon as Ge is

deposited. Si atoms are incorporated into the WL in the initial phase of growth and into the islands after the beginning of their nucleation.

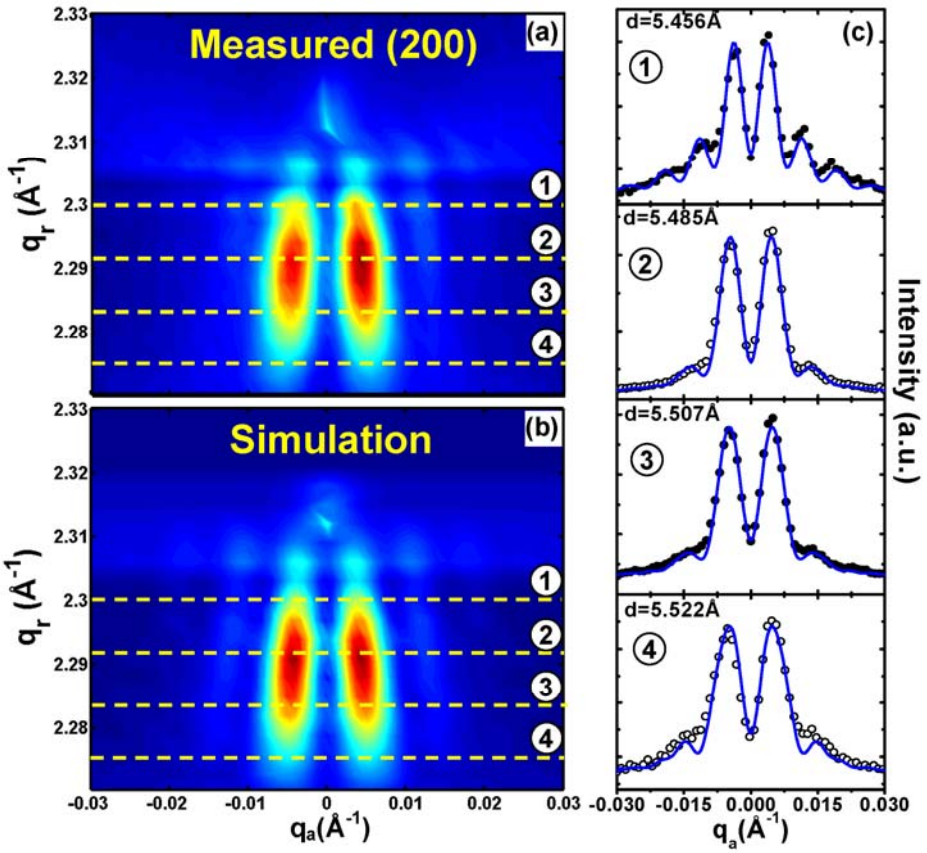

Fig. 4.9 – (a) Measured q_r,q_a intensity map for sample B in the vicinity of the Si (200) reflection. (b) Fitted intensity map based on selected angular scans. Four numbered q_a scans (dashed lines in maps (a) and (b)) are shown in (c). In these cuts the dots represent the measured data of (a) and the solid lines are the fits obtained from (b).

The map shown in Fig. 4.9(b) was obtained using Eq. 4.3, consisting of the ordered domain distribution inside the islands, taking into account the interference between neighboring layers with different lattice parameters, square shaped domains and corresponding composition profiles. The WL peak was included in the simulation describing the scattering from a thin SiGe film at the surface, strained to the Si bulk lattice parameter. Selected angular cuts from the experimental and calculated maps are shown in Fig. 4.9(c). The possible interference between anti-phase domains belonging to different islands was ruled out by performing simulations using correlation functions, which could not reproduce the scattering data.

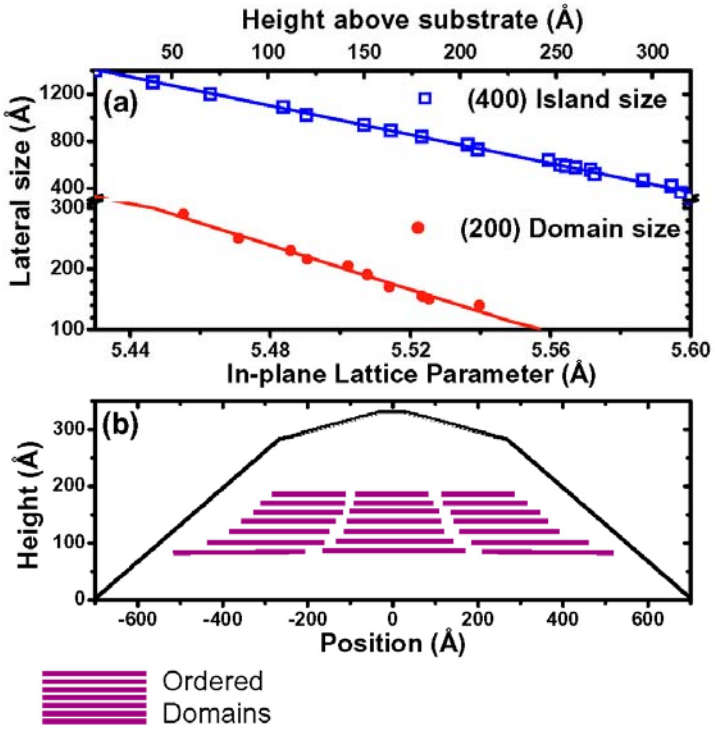

Fig. 4.10 – (a) Size of the islands and domains of sample B as a function of in-plane lattice parameter. (b) Schematic map for the islands of sample B, showing the location of the ordered domains.

A comparison between the island and domain size in sample B is shown in fig. 4.10(a), where the domain size was obtained from fits of the (200) map and the island size from scans at the (400) reflection (not shown here). The height information was introduced by correlating the size of an iso-lattice parameter region in the (400) reflection with a height inside the island obtained from AFM profiles [MagalhãesPaniago02, Schülli03a]. Assuming that the strain status of the ordered alloy at the (200) reflection follows the strain relaxation of the whole island this association was extended to the ordered regions. For both island and domain there is an approximate linear variation of size with lattice parameter and height. It can be inferred that 9 ordered domains could fit inside each constant lattice parameter layer. There is a clear variation of domain size with increasing lattice parameter and height, suggesting the existence of a stress-mediated mechanism that determines the domain size. Fig. 4.10(b) depicts schematically what should be the distribution of domains inside the islands of sample B.

Finally, the Ge content in sample B ordered domains was determined by X-ray anomalous scattering (chemical contrast) near the Ge K-edge using two photon energies: E_1=11040eV and

E_2=11102eV [MagalhãesPaniago02]. Since $I_{(200)} \propto V_{200}(C_{Ge}f_{Ge} - C_{Si}f_{Si})^2$ [Warren69], experimental integrated intensities I_1 and I_2 measured for the two energies were used to infer the Ge concentration, given by

$$C_{Ge}=[f_{Si}(\sqrt{I_1}-\sqrt{I_2})]/[\sqrt{I_1}(f_{Ge2}+f_{Si})-\sqrt{I_2}(f_{Ge1}+f_{Si})], \quad (4.5)$$

where f_{Ge1} and f_{Ge2} are the two Ge scattering factors [MagalhãesPaniago02]. Eq. 4.5 is similar to eq. 2.18 that was used to obtain the total Ge concentration in chapter 2 by using measurements performed at the (400) reflection. Fig. 4.11(a) shows angular scans performed at the two energies E_1 and E_2 for one specific lattice parameter d=5.47Å. The Ge concentration was calculated from the integrated q_a-intensities of these two curves and it was found to be C_{Ge}=0.53±0.08. This analysis was repeated for all angular scans of the (200) q_r-q_a map and a nearly constant Ge concentration of 0.5±0.1 was found. In order to locate these domains inside the islands a 3-dimensional concentration map of the domes was obtained from similar anomalous scattering measurements of the (400) reflection (see chapter 3) [Malachias03c], and compared to the (200) q_a-scans. Fig. 4.11(b) shows the composition/ordering map for sample B islands. The ordered regions are present mainly in parts of the island where the Ge concentration reaches approximately 0.5.

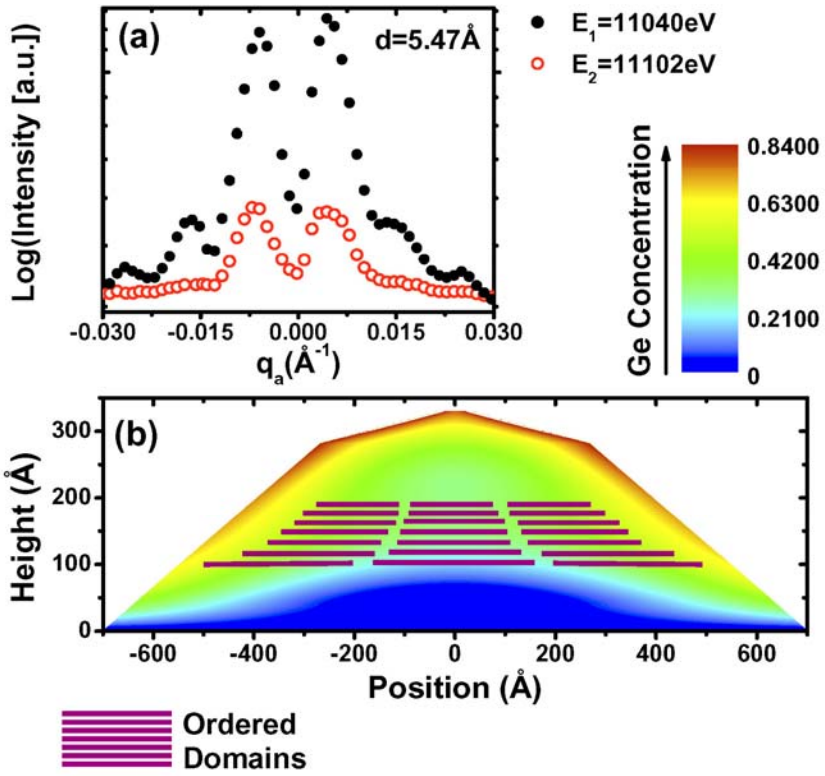

Fig. 4.11 – (a) (200) anomalous X-ray angular scans, from which the integrated intensities were used to determine the domain Ge concentration. (b) Ge concentration map for sample B islands, with the location of the ordered domains.

4.4 Bragg-Williams Order Parameter of samples grown at different temperatures

The influence of the growth temperature on ordering was evaluated for the whole temperature sample series. Fig. 4.12 shows q_r-q_a maps in the vicinity of the (400) reflection (maps a, c, e, g) and the (200) reflection (maps b, d, f, h) for samples A (a, b), B (c, d), C (e, f) and D (g, h). The equivalent lattice parameter region is the same in both reflections for each sample. Intensity scales are logarithmic in the (400) maps and linear in the (200) maps for a better visualization of their profiles. Reciprocal space regions that were not measured appear in white at the (200) maps.

In all samples the (200) scattered intensity is observed up to 60% of the island total relaxation that is measured in the (400) maps. This indicates that ordering is possibly strain stabilized. In all (200) maps the scan step is larger than the width of a (200) multiple scattering peak that usually observed exactly at the Si (200) position. Hence, the structures observed at the Si (200) position in fig 4.12 (b, d, f) are due to the presence of partially ordered alloys in the WL. In the (200) map of fig. 4.12(f) (Sample C) one observes a broad peak at the Si position. At this temperature range the (200) ordering starts to be inhibited due to the annealing that takes place at the equivalent sample growth time [Reichert99]. For sample D that was grown at 840°C the (200) ordering at the WL disappears.

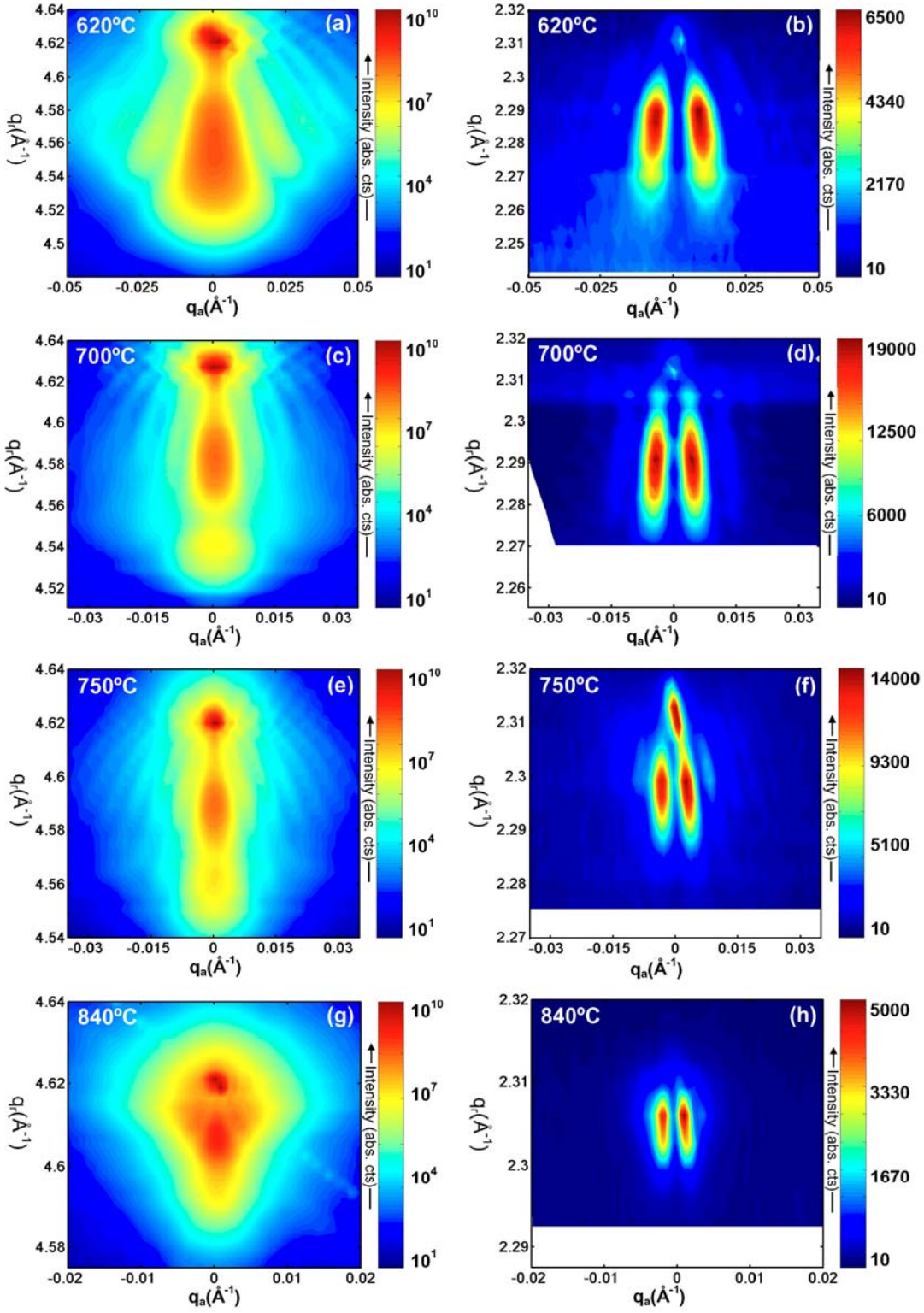

Fig. 4.12 – Measured q_r-q_a (400) and (200) maps for samples A (a, b), B (c, d), C (e, f) and D (g, h). The color scale is logarithmic in the (400) maps and linear in the (200) maps for better visualization. The q_r axis are the same for both reflections in each sample. Intensities are shown in absolute counts. The white regions in the (200) maps correspond to reciprocal space positions that were not measured

Figure 4.13 shows the relationship between islands/domains strain, size and height for samples A (a), C (b) and D (c). The height position of ordered domains starts always after a minimum height of 50Å due to the Si-rich island basis [Malachias03c, Schülli05].

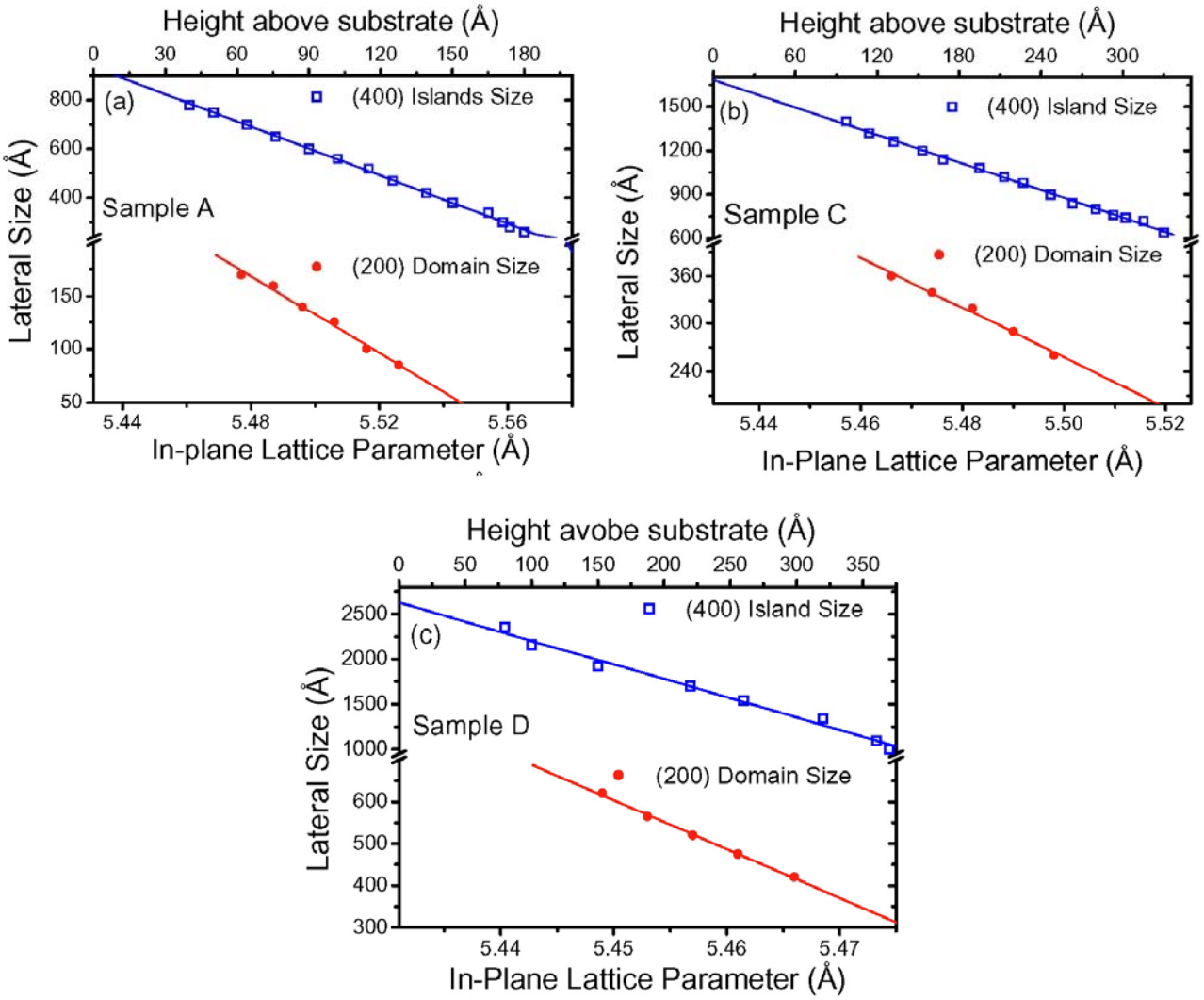

Fig. 4.13 – Island and domain size as a function of lattice parameter end height for samples A (a), C (b) and D (c).

The degree of ordering inside Ge islands can be estimated by comparing the intensities of fundamental and superstructure reflections [Warren69]. For the Ge islands this comparison was done between the in-plane (400) and (200) reflections. The intensity of the (400) reflection is proportional to the square of the sum of atomic scattering factors of Si (f_{Si}) and Ge (f_{Ge}), i.e. (eq. 1.39),

$$I_{(400)} = c4V_{400}(C_{Ge} f_{Ge} + C_{Si} f_{Si})^2, \quad (4.6)$$

where C_{Ge} and C_{Si} are the concentrations of Ge and Si respectively and V_{400} is the volume of the region at the Bragg condition. In contrast, the intensity measured at the (200) reflection is proportional to the square of the *difference* of the atomic scattering factors and depends on the degree of ordering expressed by the Bragg-Williams order parameter *S* [Warren69], i.e. (eq. 1.38),

$$I_{(200)} = cV_{200}S^2(f_{Ge} - f_{Si})^2. \quad (4.7)$$

Following the steps of chapter 1 S is obtained from eq. 1.41:

$$S = \sqrt{\frac{I_{200}}{I_{400}}} \frac{2(f_{Ge}C_{Ge} + f_{Si}C_{Si})}{(f_{Ge} - f_{Si})}. \quad (4.8)$$

For one atomic in-plane layer with two types of sites α (Ge) and γ (Si) the ordering parameter *S* is defined as $S = r_\alpha + r_\gamma - 1$ [Warren69], where r_α and r_γ are fractions of α and γ sites occupied by the right atom. The value *S* = 0 indicates that 50% of the atoms are in their wrong sites, denoting a completely random alloy, while *S* = 1 represents a perfectly ordered arrangement.

Comparing the measured q_a-integrated intensities of (200) and (400) reflections of sample B an order parameter S = 0.40 ± 0.03 was obtained, which represents a lower bound for the degree of ordering, since $V_{400} > V_{200}$. This value indicates a high degree of ordering when compared to S = 0.18, obtained for $Si_{0.5}Ge_{0.5}$ alloy layers [Tischler95]. The stress caused by the deposition of pure Ge on Si is higher than for an alloy layer, possibly increasing the efficiency of the ordering mechanism [Jesson91, Jesson92, Jesson93]. According to *Jesson et al.* and *Tischler et al.* [Jesson91, Jesson93, Tischler95] each atomic plane parallel to the substrate has only one type of Ge-rich site (α or β) and only one type of Si-rich site (γ or δ) as shown in fig. 4.8. Thus, S can be considered an average value over the whole crystal (all domains). Using the definition $S = r_\alpha + r_\gamma - 1$ [Warren69], where r_α and r_γ are fractions of α and γ sites occupied by the right atoms, we obtain that at least 70% of the atoms inside the islands of sample B are in their correct positions. Bragg-Williams ordering parameters for all samples were calculated comparing the experimental intensities of (400) and (200) maps.

Order parameter results for all samples are shown in fig. 4.14 together with the ratio of the integrated intensities of the Si-Ge and Ge-Ge Raman peaks. As mentioned before this Raman intensity ratio (I_{SiGe}/I_{GeGe}) between the 295cm^{-1} and 414cm^{-1} vibrational modes reveals the relative abundance of Si-Ge bonds inside the islands [Finkman2001, Dvurechenskii2004] and can be semi-

quantitatively compared with the ordering parameter S. The growth-temperature dependence of these parameters seen in fig. 4.14 exhibits an excellent agreement between these techniques, indicating that Raman measurements indirectly support the x-ray results.

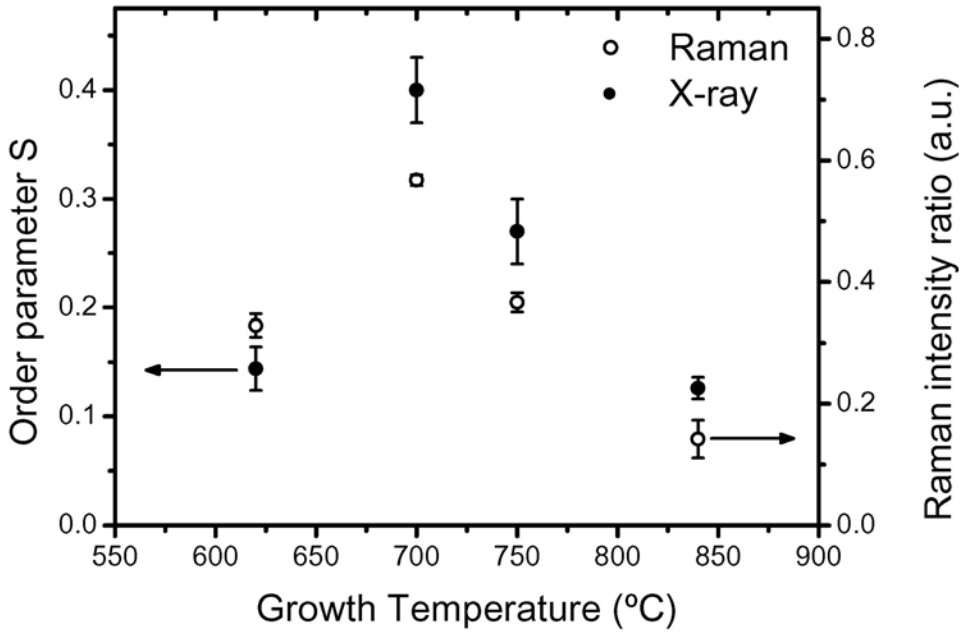

Fig. 4.14 – Order parameter S and Raman integrated intensity ratio between Si-Ge and Ge-Ge peaks (I_{SiGe}/I_{GeGe}).

4.5 Discussion

It is worth noting that ordered domains may influence the electronic/optical properties of these islands. The presence of ordered domains may result in a shift of the phonon frequency, band edge alignment and even the semiconductor gap [Ahrenkiel99]. Thus, any realistic calculation of quantum dot properties should take this into account. Changing the growth temperature it is possible to favor or avoid the formation of ordered alloy regions inside Ge domes. The ordering efficiency maybe also modified by tuning the growth rate, which was fixed for the sample series used here.

In summary, by measuring basis-forbidden x-ray reflections of self-assembled Ge:Si(001) islands we have demonstrated the existence of atomically ordered regions inside these nanostructures. X-ray scattering maps evidenced that these small ordered domains are separated by anti-phase boundaries. Order parameters were calculated to all samples and corroborated by Raman measurements.

Chapter 5

Conclusion

Ge islands on Si(001) have been extensively studied as a model for Stranski-Krastanov island growth since only two chemical species are involved. In this work x-ray scattering techniques were employed to depict the most relevant structural features of these islands that may influence their final optoeletronic response.

The technique of Grazing Incidence Diffraction has proved to be highly sensitive to strain variations inside the islands as well as to their size and shape. Chemical contrast was achieved by use of anomalous x-ray scattering contrast. By correlating composition and strain measurements it was possible to directly observe the reduction of the elastic energy during Wetting-Layer–Pyramid and Pyramid–Dome transitions, which is probably the crucial driving force for these morphological transitions. These methods were extended to a complete 3D mapping of strain, Ge content, and elastic energy inside the domes. Finally, superstructure reflections revealed the formation of ordered SiGe alloys in a set of samples grown at different temperatures. This result, independently supported by Raman measurements, implies that a strong kinetic mechanism also influences (and may rule) Si interdiffusion. Figure 5.1 summarizes the methods and results that were described in this thesis.

Three final remarks have to be pointed out here. First, the precise rule of thermodynamics and kinetics on Ge growth still remains unclear. On one hand it has been shown that thermodynamic arguments can explain quite well the phenomena of shape transitions, bimodal size distribution and faceting in these islands. On the other hand the observation of trenches and ordered alloys are clear evidence of the presence of a kinetic component.

Secondly, one has to keep in mind that a complete *tomography* method can only be achieved by mapping all possible x-ray reflections. Such set of measurements allows a reconstruction of shape as well as strain and composition in all directions inside the islands.

Finally, all results obtained by x-ray methods lie on statistical averaging over a wide region of the sample that generally contains thousands of islands. One cannot rely on the structural parameters given by x-ray results to develop single quantum dot devices.

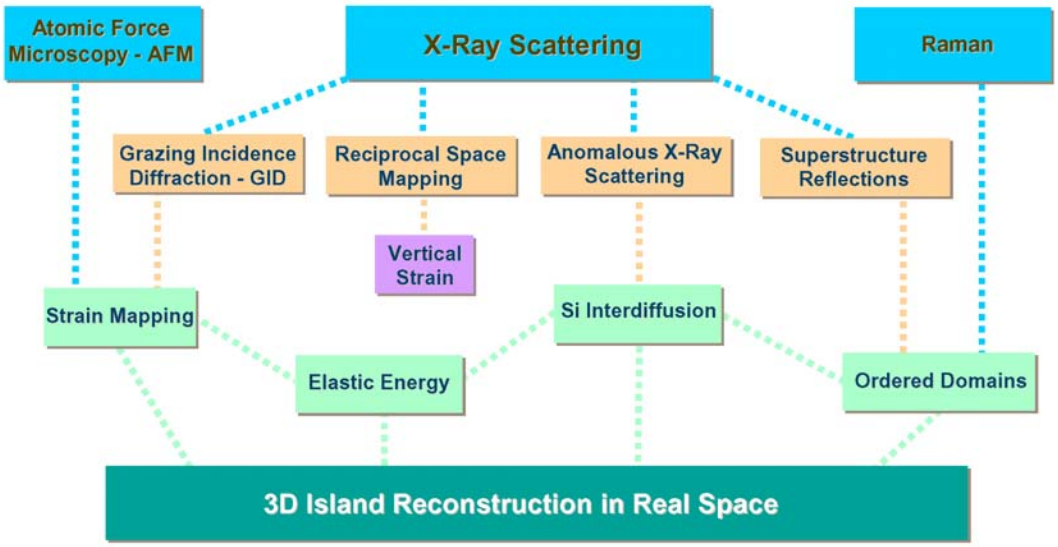

Fig. 5.1 – Summary of methods used in this thesis and experimental results.

Chapter 6

Síntese do trabalho em português

6.1 – Introdução aos métodos experimentais

O objetivo deste resumo estendido em português é mostrar um conjunto mínimo e coerente de técnicas e resultados que permitam a compreensão geral dos principais resultados dos capítulos precedentes. A informação contida nas páginas anteriores não pode ser transferida integralmente a este resumo e, por isso, foi adotada uma abordagem mais descritiva e sucinta.

6.1.1 – Difração por incidência rasante (GID)

O estudo de superfícies através de técnicas de espalhamento de raios-x teve um grande crescimento a partir da década de 80 [Vineyard82]. Com a crescente utilização de radiação síncrotron – de maior intensidade em relação a fontes convensionais – o uso da técnica de difração de raios-x por incidência rasante (GID) tornou-se viável. Esta técnica baseia-se no fato do índice de refração para sólidos ser inferior ao índice de refração do ar ou do vácuo [Dosch92]. Esta diferença, da ordem de 10^{-5}, gera um ângulo crítico de reflexão externa total α_c de aproximadamente 0.5º. Fótons de raios-x que incidem sobre a amostra sob ângulos menores que α_c são refletidos. Entretanto, neste caso, uma onda evanescente propaga-se paralelamente à superfície e com penetração restrita a poucas camadas atômicas para dentro do sólido (tipicamente 100Å) [Dosch92].

Em uma geometria típica de GID a amostra cristalina é iluminada pelo feixe de raios-x sob um ângulo de incidência rasante α_i ($\alpha_i < \alpha_c$). O cristal é girado em torno do eixo normal à superfície até que um plano atômico perpendicular a este eixo obedeça a condição de Bragg. Neste caso é possível medir os parâmetros de rede no plano da superfície do cristal. Um detector sensível à posição (PSD) orientado perpendicularmente à superfície da amostra é utilizado para coletar todos os vetores de onda espalhados na direção vertical [Metzger98, Malachias02].

O sistema de coordenadas relativo (radial-angular) utilizado para as medidas pode ser visto esquematicamente na fig. 6.1. A componente radial q_r da transferência de momento define a distância da origem do espaço recíproco. A componente angular q_a está relacionada ao desvio $\Delta\omega$ da condição de Bragg $\omega = 2\theta/2$. q_z é a componente vertical da transferência de momento e define a distância do plano q_r-q_a.

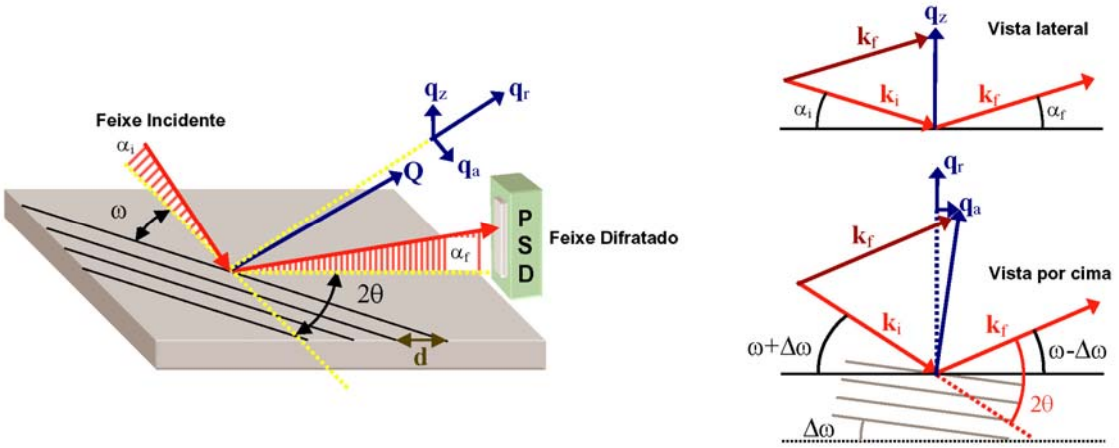

Fig. 6.1 – Geometria de difração por incidência rasante (GID). As componentes radial (q_r), angular (q_a) e vertical (q_z) do vetor transferência de momento são vistas em detalhe à direita.

6.1.2 – Espalhamento anômalo (ressonante) de raios-x

O fator de espalhamento atômico *f* de um átomo é dado por:

$$f = f_0(Q) + f'(E) + f''(E). \qquad (6.1)$$

onde $f_0(Q)$ é um termo que inclui a distribuição espacial dos elétrons (fator de forma atômico) [Warren69] e *f'* e *f"* são correções ao valor total de *f* que dependem da energia do raio-x utilizada. Para que uma medida de raios-x seja sensível à composição de um dado

cristal é necessário alterar o valor do fator de espalhamento atômico de um (ou mais) elementos que o compõem. Isto é feito alterando-se os valores de *f'* e *f"* na eq. 6.1 através de uma escolha da energia do fóton de raio-x incidente.

Para descrever o comportamento ressonante próximo à energia de uma borda de absorção é necessário pensar nos níveis de energia de um átomo. Os elétrons mais fortemente ligados encontram-se na camada K, cuja borda de absorção para o fósforo (Z = 15) e todos os elementos de maior número atômico é acessível para energias de raios-x acima de 2 keV. Se a energia do fóton de raios-x é muito menor que a energia K de ligação a resposta destes elétrons ao campo externo é reduzida (fator *f'* muito pequeno). Se a energia do fóton incidente é muito maior que a energia de ligação os elétrons podem ser tratados como "quase-livres" e *f'* vale zero. Para energias entre esses limites *f'* apresenta um comportamento ressonante e os elétrons ligados podem ser descritos por um modelo de oscilador harmônico forçado. A mudança da fase deste oscilador a energias próximas a ressonância dá origem ao fator i*f"* da eq. 6.1.

A fig. 6.2 mostra a variação das correções *f'* e *f"* do fator de espalhamento atômico do Ge próximo à borda de absorção K deste átomo. Comparando-se medidas feitas com as duas energias assinaladas na fig. 6.2 é possível determinar a quantidade de Ge existente dentro de um cristal, pois a redução da intensidade espalhada próximo a borda K (11103eV) indicará a presença de átomos de Ge [AlsNielsen01].

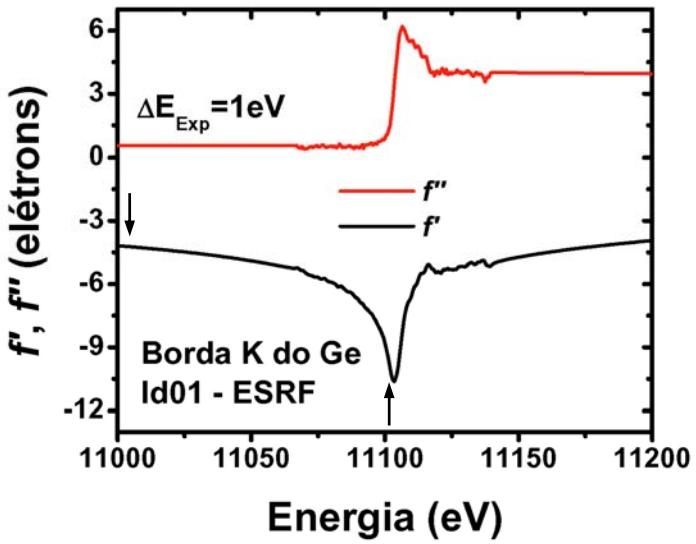

Fig. 6.2 – Correções *f'* e *f"* do fator de espalhamento atômico do Ge próximo à borda de absorção K. Comparando-se medidas feitas nas energias assinaladas por setas é possível obter, através do contraste de intensidades espalhadas, a concentração de Ge no material estudado.

6.1.3 – Fator de estrutura e parâmetro de ordem S

O fator de estrutura de uma célula unitária depende das posições dos átomos $\mathbf{r_n} = x_n\mathbf{a_1} + y_n\mathbf{a_2} + z_n\mathbf{a_3}$. Essa posição é definida em função das coordenadas fracionárias x_n, y_n, z_n na base de vetores da rede $\mathbf{a_1}$, $\mathbf{a_2}$ e $\mathbf{a_3}$. Para uma reflexão de índices (h k l) o fator de estrutura é dado por [Warren69]

$$F_{hkl} = \sum_n f_n e^{2\pi i(h\mathbf{b_1}+k\mathbf{b_2}+l\mathbf{b_3})(x_n\mathbf{a_1}+y_n\mathbf{a_2}+z_n\mathbf{a_3})} = \sum_n f_n e^{2\pi i(hx_n+ky_n+lz_n)}, \qquad (6.2)$$

onde f_n é o fator de espalhamento atômico do átomo n e $\mathbf{b_1}$, $\mathbf{b_2}$, $\mathbf{b_3}$ são a base de vetores do espaço recíproco. Para descrever a estrutura de diamante, na qual Si e Ge bulk se cristalizam, deve-se considerar duas sub-redes de face centrada (FCC) contendo átomos de Si (Ge) deslocadas de ¼ em todas as direções. Neste caso os átomos de Si estarão nas posições fracionárias

$$Si_{(1)} \rightarrow \begin{matrix} 0 & 0 & 0 \\ ½ & ½ & 0 \\ ½ & 0 & ½ \\ 0 & ½ & ½ \end{matrix} \qquad Si_{(2)} \rightarrow \begin{matrix} ¼ & ¼ & ¼ \\ ¾ & ¾ & ¼ \\ ¾ & ¼ & ¾ \\ ¼ & ¾ & ¾ \end{matrix}. \qquad (6.3)$$

Substituindo as posições dadas em 6.3 na eq. 6.2 é possível encontrar as famílias de reflexões listadas na tabela abaixo [Warren69].

Reflection	Intensity
$h+k+l = 4n$	$F_{hkl}^2 = 16(2f_{Si})^2$
hkl odd	$F_{hkl}^2 = 16(2f_{Si}^2)$
hkl mixed	$F_{hkl}^2 = 0$
$h+k+l = (2n+1)2$	$F_{hkl}^2 = 0$

A última reflexão da tabela é de particular interesse para este trabalho. Apesar de não ser observada em cristais puros de Ge e Si este tipo de reflexão pode ter valor não nulo para a rede cristalina de uma liga onde as posições das duas espécies atômicas estão ordenadas. Ao substituir os átomos de Si na segunda sub-rede de 6.3 por átomos de Ge obtém-se a estrutura *zincblend* mostrada na fig. 6.3

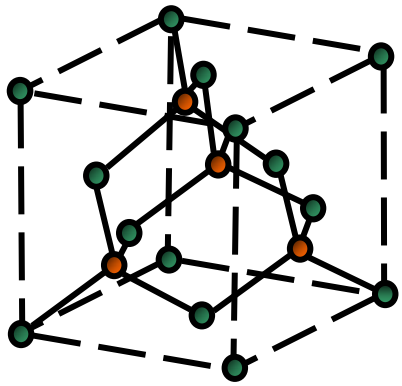

Fig. 6.3 – Célula unitária de uma estrutura *zincblend* de SiGe. Os átomos de Ge aparecem na cor laranja.

Para a estrutura mostrada em 6.3 podem ser medidas reflexões do tipo (200) e (420), com fator de estrutura proporcional ao quadrado da diferença dos fatores de espalhamento atômico de Si e Ge

$$F_{hkl}^2 \propto (f_{Ge} - f_{Si})^2 \qquad \text{para} \qquad h+k+l = (2n+1)2. \tag{6.4}$$

Este valor para o fator de estrutura depende, entretanto, da estequiometria da liga e do ordenamento das posições atômicas dentro do cristal. É necessário que Si e Ge ocupem posições alternadas em uma ou mais direções ao longo do cristal para que uma reflexão de superestrutura deste tipo possa ser medida. A intensidade de uma reflexão de superestrutura dependerá, então, de um parâmetro que especifique o grau de ordenamento da liga SiGe. A eq. 6.4 deve ser corrigida pelo parâmetro de ordem S, que vale 1 para a liga completamente ordenada e zero para uma liga onde os átomos ocupam posições aleatórias [Warren69].

Assim, a intensidade integrada de uma reflexão de superestrutura do tipo (200) será dada por

$$I_{(200)} = cV_{200}S^2(f_{Ge} - f_{Si})^2, \tag{6.5}$$

onde c é uma constante que inclui todos os parâmetros de espalhamento (como fluxo de fótons, área iluminada da amostra, etc) e V_{200} é o volume da região que satisfaz a condição de Bragg. A intensidade integrada de uma reflexão permitida como a (400) é dada por

$$I_{(400)} = c4V_{400}(f_{Ge}n_{Ge} + f_{Si}n_{Si})^2. \tag{6.6}$$

O parâmetro de ordem S pode ser, portanto, obtido experimentalmente através da razão das intensidades $I_{(200)}$ e $I_{(400)}$ comparando-se regiões do espaço recíproco de mesmo volume ($V_{400} = V_{200}$). Deste modo [Warren69]

$$\frac{I_{200}}{I_{400}} = \frac{S^2(f_{Ge} - f_{Si})^2}{4(f_{Ge}n_{Ge} + f_{Si}n_{Si})^2} \quad \rightarrow \quad S = \sqrt{\frac{I_{200}}{I_{400}}}\frac{2(f_{Ge}n_{Ge} + f_{Si}n_{Si})}{(f_{Ge} - f_{Si})}. \tag{6.7}$$

6.2 – Composição e strain em ilhas de Ge:Si

6.2.1 – Crescimento de ilhas de Ge em Si (001)

Ilhas de Ge em Si(001) são um modelo para o estudo de crescimento heteroepitaxial. Os dois elementos possuem propriedades estruturais e eletrônicas semelhantes e apresentam um descasamento de parâmetro de rede de 4.2%. Três etapas distintas de crescimento podem ser destacadas para a formação de ilhas de Ge:Si. Inicialmente observa-se um crescimento camada por camada até uma espessura de 3.5 monocamadas atômicas (MLs). Para filmes mais espessos a energia elástica é parcialmente liberada através da formação de ilhas piramidais de baixa razão de aspecto e facetas {105} (que serão designadas aqui como pirâmides). Finalmente, para uma cobertura de Ge maior que 6 MLs ocorre uma transição da forma das ilhas de pirâmides para domos, que são ilhas de maior volume, maior razão de aspecto e facetas mais complexas [Medeiros-Ribeiro98].

Os resultados discutidos nesta seção (6.2) referem-se a duas amostras crescidas por CVD a 600ºC. Um total de 5.9ML de Ge foi depositado na amostra de pirâmides a uma taxa de deposição de 0.1ML/s enquanto para a amostra de domos foram depositados 11.2ML de Ge com taxa de deposição de 0.05ML/s. Medidas de Microscopia de Força Atômica (AFM) foram feitas nas duas amostras, revelando uma distribuição de tamanhos monodispersa para os dois conjuntos de ilhas. Para cada tipo de ilha as dimensões (médias) encontradas foram: (a) Pirâmides – 30±10Å de altura e 240±60Å de raio; (b) Domos – 140±20Å de altura e 320±40Å de raio [Magalhães-Paniago02].

A fim de avaliar a deformação do parâmetro de rede (strain) dentro das ilhas de Ge medidas de Difração por Incidência Rasante (GID) foram realizadas nas linhas XRD1 e XRD2 para as duas amostras. A energia dos raios-x foi mantida constante a 11keV e o ângulo de incidência fixado em 0.35º, essencialmente o ângulo crítico de reflexão externa total do substrato de Si. Dois tipos de varreduras podem ser feitas na geometria GID. Uma varredura radial é feita variando-se $q_r = (4\pi/\lambda)\sin(2\theta/2)$. Experimentalmente isso equivale a acoplar os ângulos ω e 2θ com a condição $\omega = 2\theta/2$. De acordo com a lei de Bragg $\lambda = 2d\sin(2\theta/2)$ uma varredura radial é sensível ao parâmetro de rede no plano do substrato e,

conseqüentemente, ao estado de deformação (strain) dentro das ilhas. Para cada valor de 2θ o espalhamento origina-se de regiões da ilha com diferentes parâmetros de rede a' = $2\pi/q_r$.

Varreduras radiais ao longo da direção (400) são vistas na fig. 6.4 para as amostras de pirâmides e domos. Estas varreduras estendem-se do parâmetro de rede do Si (pico fino do substrato) até regiões que correspondem a parâmetros de rede maiores (q_r menores). As setas indicam as posições de Si e Ge bulk. Para as pirâmides o relaxamento de strain é observado apenas até 1.5% devido à reduzida razão de aspecto desse tipo de ilha. Para os domos, que possuem uma maior razão de aspecto, um maior relaxamento de strain é observado (3,8%). Esta é a primeira indicação de que a energia elástica armazenada nas pirâmides é parcialmente liberada durante a transição para domos [Malachias03a].

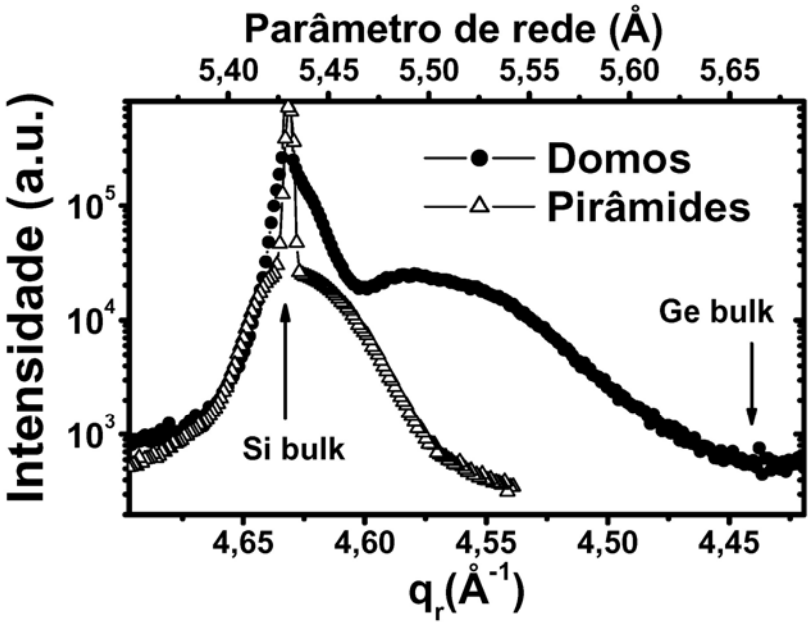

Fig. 6.4 – Varreduras radiais mostrando a distribuição de parâmetros de rede próximo à reflexão (400) do Si para pirâmide e domos. A escala superior indica diretamente o parâmetro de rede no plano [Malachias03a].

A relação entre tamanho da ilha e parâmetro de rede é determinada através de varreduras angulares ω (q_a) com ângulo 2θ fixo (q_r). Varreduras angulares na vizinhança da reflexão (220) do Si são vistas na Fig. 6.5(a) e 6.5(b) para pirâmides e domos, respectivamente. A largura do perfil deste tipo de varredura (centrado em $q_a = 0$) é inversamente proporcional ao tamanho do objeto analisado [Cowley81, Kegel99]. A origem da intensidade espalhada pode ser facilmente entendida: à medida que o parâmetro de rede aumenta, o máximo central se alarga, indicando uma redução das dimensões dos objetos

espalhadores. Então, as ilhas de Ge são largas em regiões em que o parâmetro de rede tem valor próximo ao do Si bulk – ou seja a base das ilhas – e estreitas em regiões próximas ao topo.

A fim de quantificar a dependência do tamanho de uma dada região dentro da ilha com seu parâmetro de rede utilizou-se um modelo em que as ilhas têm seções quadradas de lado L com parâmetro de rede local dado por a' = $2\pi/q_r$. A intensidade espalhada para q_r fixo pode ser calculada pela expressão [Kegel99, MagalhãesPaniago02]

$$I(q_a) = \frac{I_0}{L^2}\left|\frac{sen\left(L/2\, q_a\right)}{sen(q_a)}\right|^2 , \qquad (6.8)$$

onde I_0 é a intensidade de espalhamento em $q_a = 0$ ($I_0 = I(q_a = 0)$).

As linhas contínuas nas figuras 6.5(a) e 6.5 (b) são ajustes feitos utilizando a equação 6.8 onde o único parâmetro é a dimensão lateral L. Os resultados de raio-x (parâmetro de rede versus tamanho lateral) podem ser associados aos de AFM (altura versus perfil lateral) para identificar a altura em relação ao substrato de cada região deformada. Esta associação é vista diretamente na fig. 6.6 [MagalhãesPaniago02].

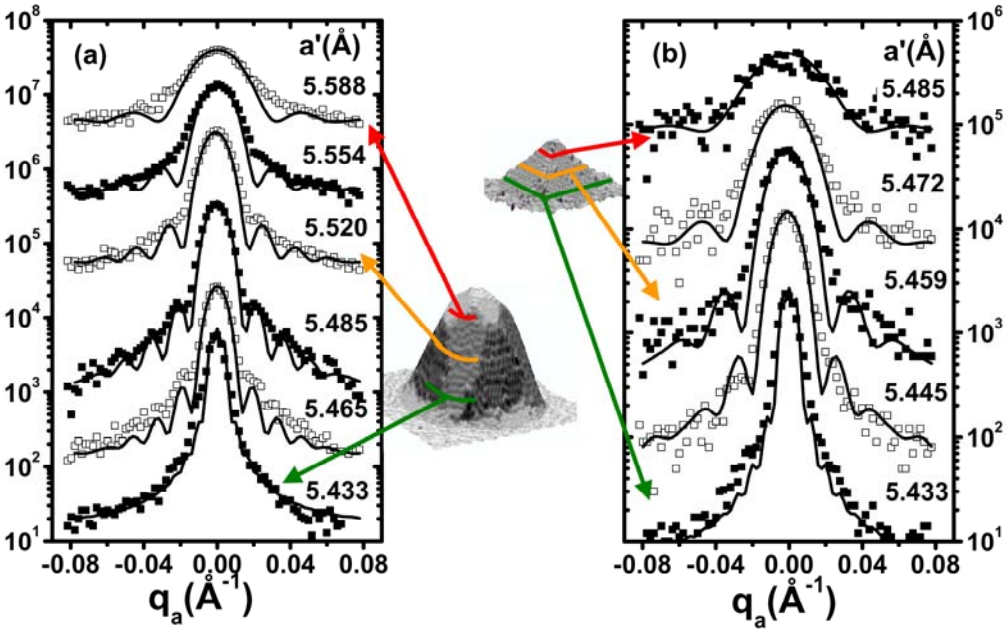

Fig. 6.5 – Varreduras angulares ao longo da direção [1-10] em diferentes parâmetros de rede locais para as amostras de domos (a) e pirâmides (b). As linhas contínuas são ajustes utilizando a eq. 6.8. As figuras que indicam esquematicamente a localização de cada região com parâmetro de rede fixo foram obtidas por microscopia de varredura por tunelamento [Rastelli02].

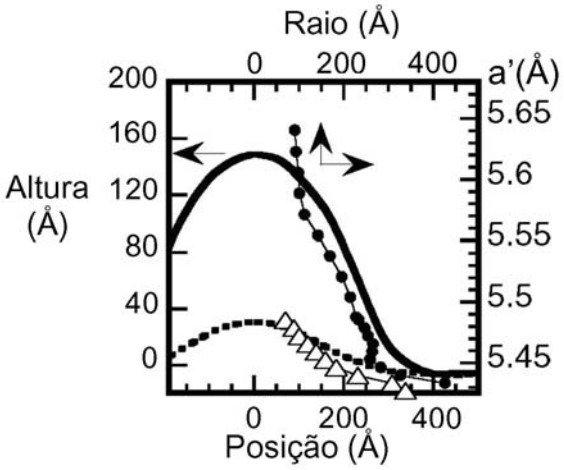

Fig. 6.6 – Comparação entre perfis de AFM para pirâmides e domos e a relação entre parâmetro de rede e tamanho lateral obtida por raios-x. Círculos referem-se aos domos e triângulos são resultados das pirâmides.

6.2.2 – Análise da composição média nas ilhas de Ge:Si

Para a determinação da composição média de Ge dentro de pirâmides e domos foram realizadas medidas de espalhamento anômalo de raios-x em duas energias próximas à borda K do Ge, conforme discutido na seção 6.1.2. As duas energias utilizadas (11003 eV e 11103eV) estão assinaladas na fig. 6.7. A redução do fator de espalhamento atômico do Ge f_{Ge} para 11103eV acarreta uma diminuição da intensidade espalhada para regiões das ilhas onde é possível encontrar átomos de Ge (para regiões contendo Ge puro a intensidade espalhada torna-se 35% menor) [MagalhãesPaniago02, Schülli03a].

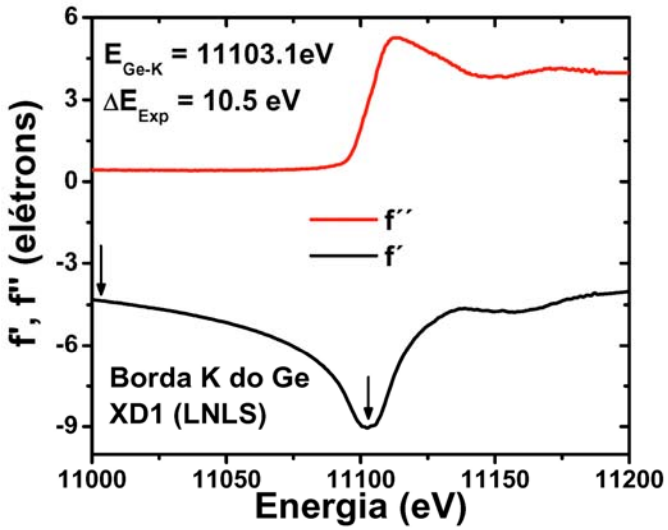

Fig. 6.7 – Variação da parte real (f') e imaginária (f") do fator de espalhamento atômico do Ge próximo à sua borda K. O fator de espalhamento atômico é dado por $f_{Ge} = f_0(Q) + f'(E) + if''(E)$.

A fig. 6.8 mostra a mudança na intensidade espalhada para varreduras radiais utilizando as duas energias na amostra de pirâmides (a) e domos (b). Observando a fig. 6.8 (a) é possível dizer que existe uma considerável quantidade de Si dentro dos domos, principalmente próximo à base deste tipo de ilha. Por sua vez, as pirâmides exibem um maior contraste de intensidade para parâmetros de rede próximos ao Si, indicando uma elevada concentração média de Ge.

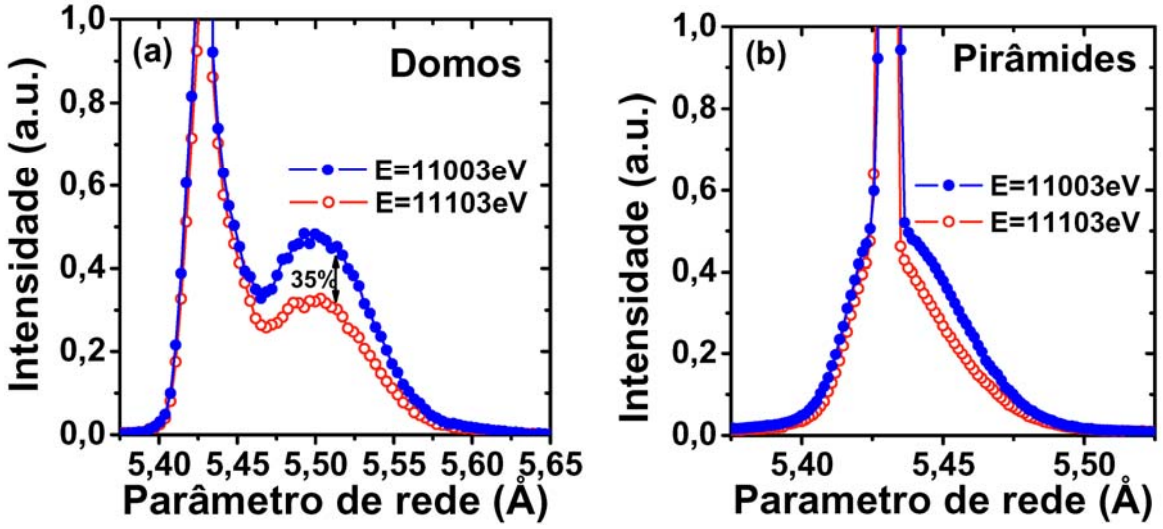

Fig. 6.8 – Varreduras radiais ao longo da direção (220) usando duas energias diferentes próximas à borda K do Ge para a amostra de domos (a) e pirâmides (b). O eixo q_r foi convertido em parâmetro de rede.

Como as ilhas são compostas por apenas dois elementos a intensidade da reflexão (220) é proporcional ao quadrado da soma das concentrações de cada elemento multiplicadas pelo fator de espalhamento atômico correspondente de Si ou Ge

$$I_1 = \text{Constante}\left|C_{Ge} f_{Ge} + C_{Si} f_{Si}\right|^2 , \qquad (6.9)$$

onde C_{Ge} e C_{Si} são as concentrações de Ge e Si dentro das ilhas ($C_{Ge} + C_{Si} = 1$), f_{Ge} e f_{Si} são os fatores de espalhamento atômico de Ge e Si, respectivamente, e todos os parâmetros de espalhamento (como fluxo de fótons, área da amostra, etc) estão incluídos na Constante. Variando-se a energia do raio-x próximo à borda de absorção de um elemento (neste caso o Ge) o fator de espalhamento muda drasticamente. Partindo da razão entre as intensidades medidas é possível obter a concentração de Ge [MagalhãesPaniago02]:

$$\frac{I_1}{I_2} = \left|\frac{C_{Ge} f_{Ge1} + C_{Si} f_{Si}}{C_{Ge} f_{Ge2} + C_{Si} f_{Si}}\right|^2 \rightarrow C_{Ge} = \left(1 + \frac{f_{Ge2}\sqrt{I_1} - f_{Ge1}\sqrt{I_2}}{f_{Si}\left(\sqrt{I_2} - \sqrt{I_1}\right)}\right)^{-1} , \qquad (6.10)$$

onde I_1 e I_2 são as intensidades de raios-x medidas nas duas diferentes energias (fator de espalhamento atômico f_{Ge1} e f_{Ge2}).

A concentração de Ge nos dois tipos de ilhas é visto na fig. 6.9. Em 6.9 (a) a composição é dada em função do parâmetro de rede enquanto em 6.9 (b) o mesmo resultado é mostrado em função da altura dentro da ilha.

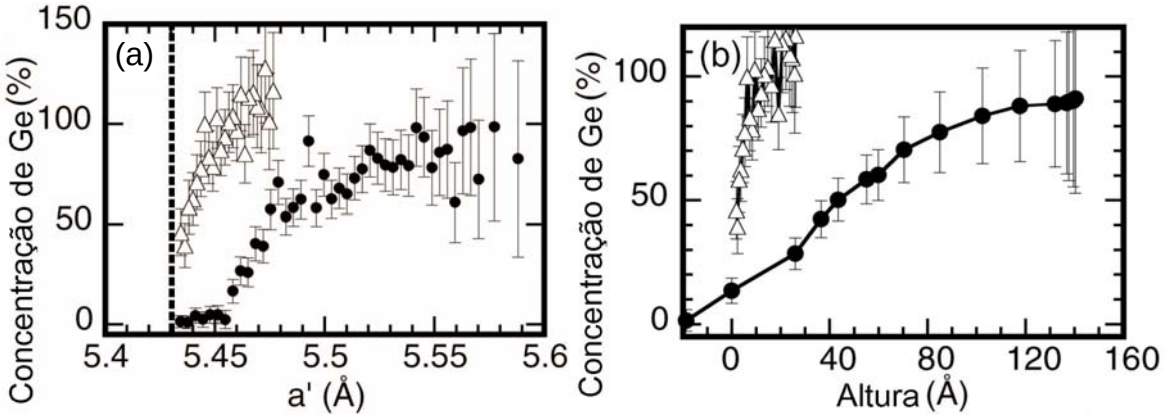

Fig. 6.9 – (a) concentração de Ge em função do parâmetro de rede local para pirâmides (triângulos) e domos (círculos). (b) concentração de Ge em função da altura, obtida com o auxílio de resultados de AFM (fig. 6.8).

6.2.3 – Energia elástica média

Como visto na seção anterior, a concentração média de Ge nas pirâmides é maior que nos domos embora nestes últimos o parâmetro de rede esteja mais próximo ao valor do Ge bulk. Para determinar a energia elástica armazenada nessas ilhas é necessário correlacionar as informações de parâmetro de rede e composição. O valor correto do strain local em cada região da ilha com composição Si_yGe_{1-y} é obtido comparando-se o parâmetro de rede medido e o parâmetro de rede de uma liga não deformada com a mesma composição química [MagalhãesPaniago02]. A fig. 6.10 mostra o valor do strain local (corrigido) em função do parâmetro de rede medido dentro das ilhas.

Para quantificar a energia elástica armazenada em cada tipo de ilha deve-se utilizar os valores de strain da fig. 6.10 na seguinte equação [Tsao93]:

$$u = 2\mu\left(\frac{1+\nu}{1-\nu}\right)\varepsilon_{\|}^2 . \qquad (6.11)$$

A energia elástica u é então obtida para a liga em função da sua constante de cisalhamento μ, razão de Poisson ν e strain local $\varepsilon_{\|}$. Desta relação podemos extrair o resultado visto na

fig. 6.11. Essa figura mostra a energia elástica média por átomo para um filme bidimensional de Ge (puro) deformado por um substrato de Si (linha contínua), para pirâmides (triângulos) e domos (círculos). O resultado desta análise mostra que a energia por átomo de um filme bidimensional de Ge é cerca de duas vezes maior que a das pirâmides e dez vezes maior que a dos domos. A transição de pirâmides para domos está, portanto, claramente relacionada a uma redução acentuada da energia elástica por átomo armazenada em cada tipo de ilha.

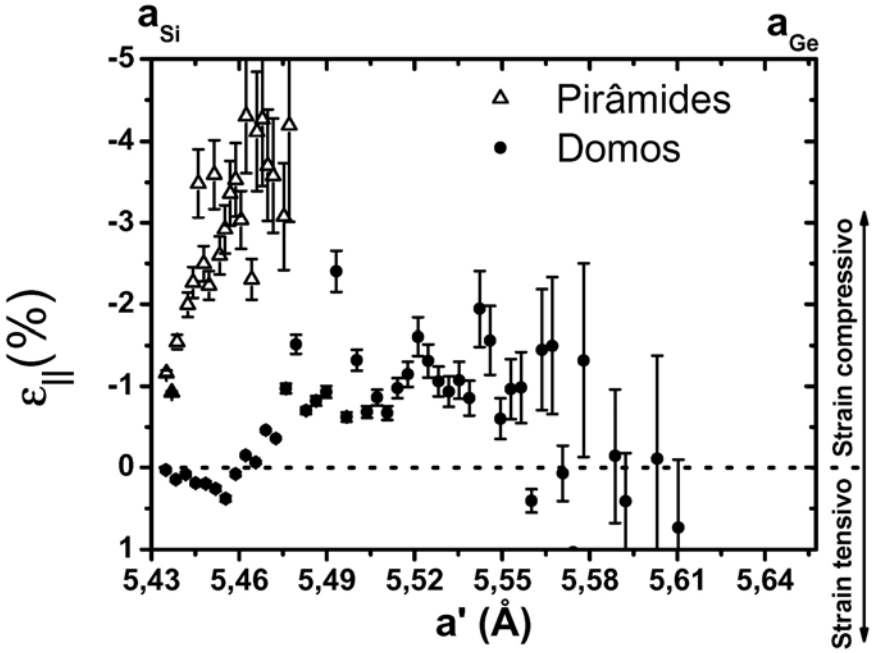

Fig. 6.10 – Strain no plano do substrato $\varepsilon_{||}$ em função do parâmetro de rede medido a'.

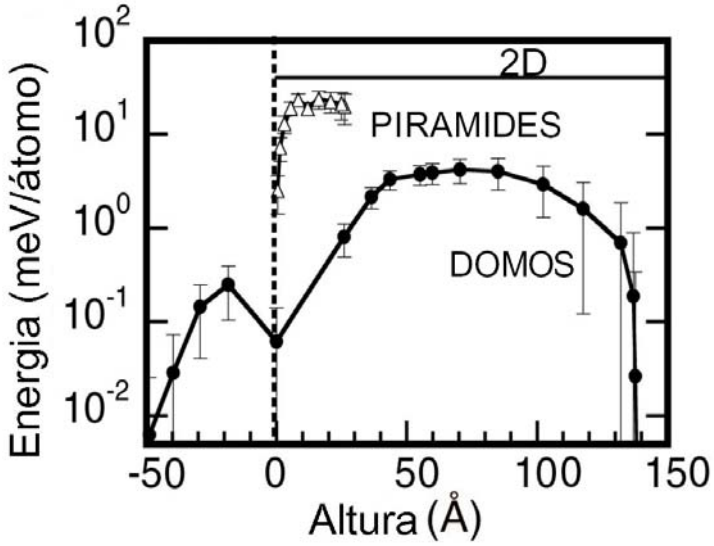

Fig. 6.11 – Energia elástica por átomo para: filme de Ge (linha), pirâmides (triângulos) e domos (círculos).

6.2.4 – Mapa de composição 3D para domos

Através do método descrito nas sub-seções anteriores foi possível encontrar um perfil de concentração média de Ge para domos e pirâmides. Entretanto, tal análise se restringiu às varreduras radiais nas duas amostras. Seguindo as mesmas linhas gerais é possível analisar todo o mapeamento (q_r-q_a) para a amostra de domos.

Mapas completos na vizinhança da reflexão (400) para a amostra de domos podem ser vistos nas figs. 6.12(a) e 6.12(b). Energias diferentes (próximas à borda K do Ge) foram utilizadas em cada mapa. No mapa 6.12(a) (E = 11103eV) o fator de espalhamento atômico do Ge é dado por f_{Ge} = 11.5 + 2i enquanto em 6.12(b) (E = 11005eV) este valor é consideravelmente maior[1], f_{Ge} = 16.2 + 0.5i.

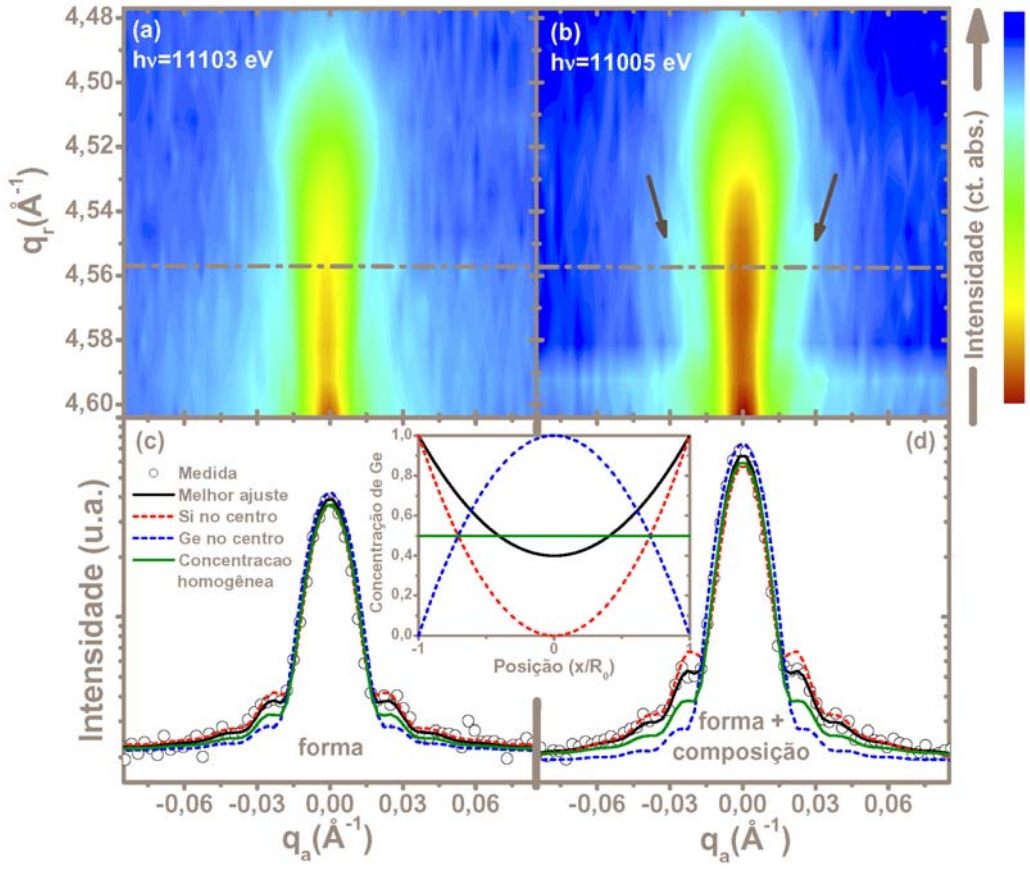

Fig. 6.12 – Mapas de espalhamento difuso (q_r-q_a) para a amostra de domos, próximos a reflexão (400) do Si utilizando-se duas energias diferentes: (a) 11103eV e (b) 11005eV. A escala de intensidades (cores) é logarítmica. (c) e (d) são varreduras angulares com q_r constante correspondendo às linhas pontilhadas em (a) e (b). Vários ajustes utilizando diferentes perfis de concentração lateral são vistos para 11103eV(c) e 11005eV(d). Os perfis de concentração lateral utilizados nos ajustes aparecem no gráfico entre (c) e (d).

[1] O fator de espalhamento atômico do Si (f_{Si} = 7.7 + 0.2i) é essencialmente constante para as duas energias.

Algumas observações quantitativas diretas podem ser feitas acerca dos dois mapas. Primeiramente, os perfis alargados na direção q_r provém da distribuição de parâmetros de rede dentro dos domos. Por fim, o fato de a intensidade espalhada a 11005eV (fig 6.12(b)) ser consideravelmente maior que a 11103eV (fig. 6.12(a)) é consistente com a diminuição do fator de espalhamento atômico do Ge nesta última energia (devido ao contraste do espalhamento anômalo).

Duas varreduras angulares correspondendo às linhas horizontais das figs. 6.12(a) e 6.12(b) são vistos em 6.12(c) e 6.12(d). Uma descrição analítica do formato das regiões de iso-parâmetro de rede foi utilizada para reproduzir estes perfis de espalhamento [Kegel01]. O fator de forma de discos, que revela a simetria cilíndrica do sistema [Kegel99], foi escolhido para ajustar as varreduras angulares. A contribuição de cada disco de Ge:Si com raio R para o perfil de espalhamento de raio-x é dada por [Malachias03c]

$$I(q_a,R)=\frac{I_0}{\pi^2R^4\left|\langle f_{GeSi}\rangle\right|^2}\left|\int_0^{2\pi}\int_0^R e^{-iq_a r\cos\theta}f_{GeSi}(r)\,r\,dr\,d\theta\right|^2, \qquad (6.12)$$

onde f_{Ge} e f_{Si} são os fatores de espalhamento atômico para Ge e Si, respectivamente, $f_{GeSi}(r) = C_{Ge}(r)f_{Ge} + [1 - C_{Ge}]f_{Si}$ é o fator de espalhamento efetivo para a liga de SiGe na posição r, e $\langle f_{GeSi}\rangle$ é o fator de espalhamento atômico médio. Na amostra utilizada as regiões de iso-parâmetro de rede de diferentes ilhas podem ter raios distintos. O perfil de espalhamento é, então, a soma de vários discos independentes $I(q_a) = A\int_{R_{min}}^{R_{max}}\pi R^2 I(q_a,R)dR$, onde A é uma constante independente da energia dos raios-x e R_{max}, R_{min} são o maior e menor raios possíveis para regiões de iso-parâmetro de rede.

Uma varredura angular a 11103eV é essencialmente sensível ao formato da região de iso-parâmetro de rede, visto que o fator de forma cilíndrico com composição homogênea ajusta-se bem ao perfil da fig. 6.12(c). Entretanto, varreduras angulares feitas a 11005eV (fig. 6.12(d)) são sensíveis à composição. Nesta energia os átomos de Ge espalham aproximadamente 4 vezes mais raios-x que os átomos de Si. O perfil calculado para um disco de concentração homogênea não se ajusta mais à varredura angular medida. A explicação mais provável para este fato é uma variação da estequiometria dentro de cada região de mesmo parâmetro de rede. Deve-se, então, introduzir uma variação lateral da composição no procedimento de ajuste das varreduras angulares. O perfil de composição

lateral mais simples (com o menor número de parâmetros) para um disco de parâmetro de rede fixo que permite reproduzir os perfis de espalhamento angulares pode ser escrito como

$$C_{Ge}(r) = C_{Ge}(0) + [C_{Ge}(R) - C_{Ge}(0)]r^2/R^2, \quad (6.13)$$

onde $C_{Ge}(0)$ é a concentração de Ge no centro do disco e $C_{Ge}(R)$ a concentração de Ge na borda, ambas com valor variando entre 0 e 1. Algumas tentativas de ajustes com diferentes perfis de composição foram feitas para o par de varreduras angulares selecionado ($q_r \sim 4.56 Å^{-1}$), conforme visto nas figs. 6.12(c) e 6.12(d). Os perfis de composição homogênea produziram formas de linha idênticas, representadas pelas linhas contínuas verdes nas duas figuras. Embora o perfil calculado ajuste-se bem à região central da varredura angular existe um desvio considerável nos máximos laterais. A sensibilidade química deste método é observada comparando-se os ajustes com Si no centro e puro Ge na borda, $C_{Ge}(R) = 0$, $C_{Ge}(0) = 1$; e com Ge no centro e puro Si na borda $C_{Ge}(R) = 1$, $C_{Ge}(0) = 0$, que demonstram como a composição lateral pode afetar os perfis angulares calculados. Embora no primeiro caso (linha pontilhada vermelha) os máximos laterais ajustem-se bem aos dados experimentais o pico central tem apresenta intensidade inferior à medida. O melhor ajuste é obtido para $C_{Ge}(0) = 0.4$ e $C_{Ge}(R) = 1.0$ como representado pela linha contínua preta.

Varreduras angulares realizadas para diferentes valores de q_r são vistas nas figs. 6.13(a) e 6.13(b). A diferença entre os valores de q_r é da ordem de $2\pi/R$, minimizando a contribuição de discos adjacentes (com parâmetro de rede diferente) para a intensidade de cada varredura angular. Os ajustes vistos em 6.13(a) e 6.13(b) foram feitos simultaneamente para as duas energias utilizando-se a dependência de $I(q_a)$ em relação aos parâmetros A, R_{min}, R_{max}, $C_{Ge}(R)$, e $C_{Ge}(0)$. Desta maneira o melhor perfil de concentração lateral para cada região de iso-parâmetro de rede foi obtido. Quatro destes perfis são vistos na fig. 6.13(c).

Todos os perfis examinados possuem uma borda de Ge puro enquanto a concentração de Ge no centro dos discos varia entre 0 para regiões próximas à base da ilha e 1 para regiões próximas ao topo. O desaparecimento dos máximos laterais para a' > 5.50Å ocorre devido ao alargamento da distribuição de tamanho das regiões de iso-parâmetro de rede que correspondem ao topo da ilha. Para regiões muito próximas à interface substrato-ilha não é possível ajustar os perfis angulares devido à superposição dos sinais de espalhamento da ilha e do substrato.

A fig. 6.14 mostra um corte lateral da reconstrução de composição 3D para os domos. Para construir este mapa foi utilizado um perfil de AFM de uma ilha média que permitiu associar parâmetro de rede de uma região dentro da ilha, tamanho e altura da mesma bem como os parâmetros $C_{Ge}(R)$, $C_{Ge}(0)$, e R. A linha pontilhada representa o limite de 65% de Ge na liga. Para confirmar a presença de um núcleo rico em Si foi realizado um etching seletivo capaz de remover ligas de Ge com concentração superior a 65%. Perfis de AFM feitos para a mesma ilha antes e após o etching [Schmidt02] corroboram independentemente a análise de raios-x.

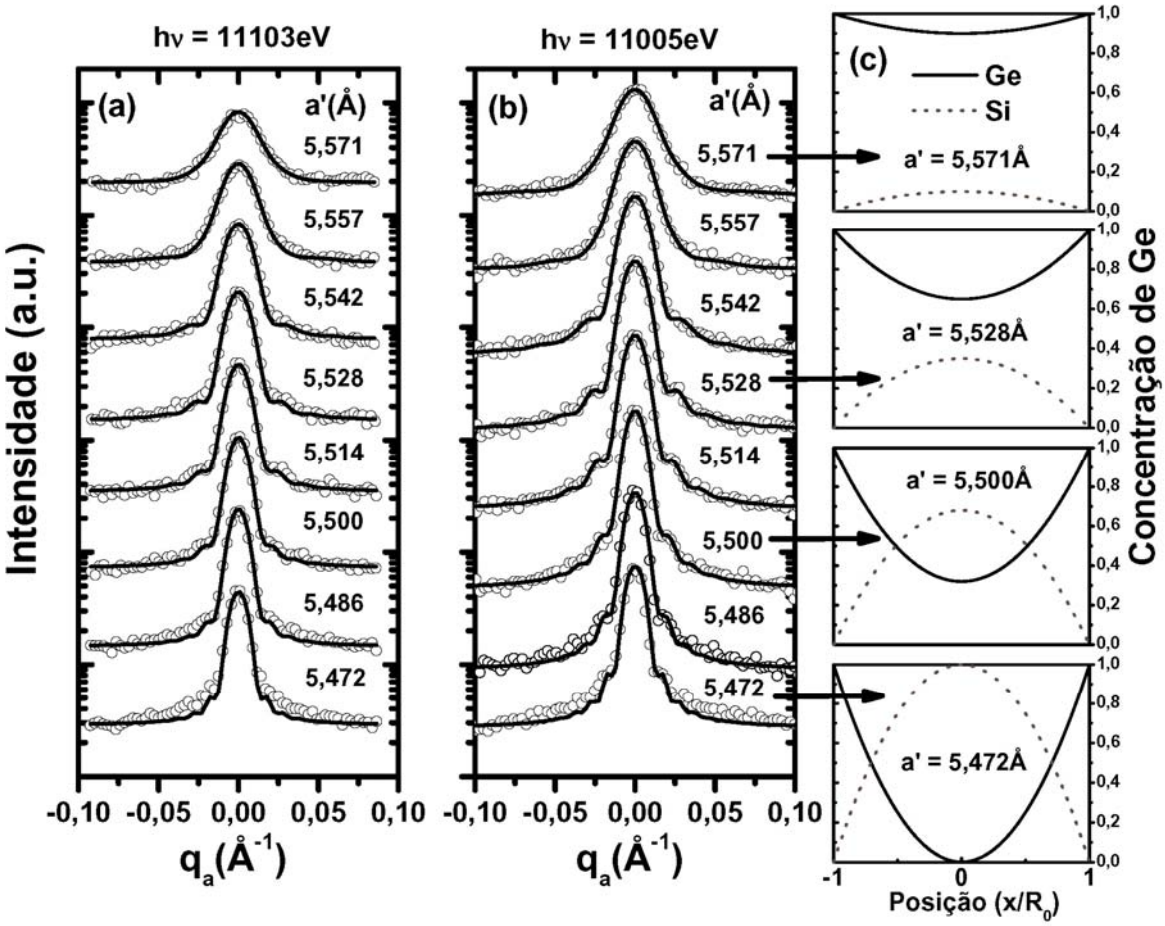

Fig. 6.13 – Varreduras angulares para a amostra de domos. Os ajustes (linhas contínuas) vistos em (a) e (b) foram utilizados para obter os perfis de composição mais adequados para cada região de parâmetro de rede fixo. Alguns perfis de composição são vistos em (c).

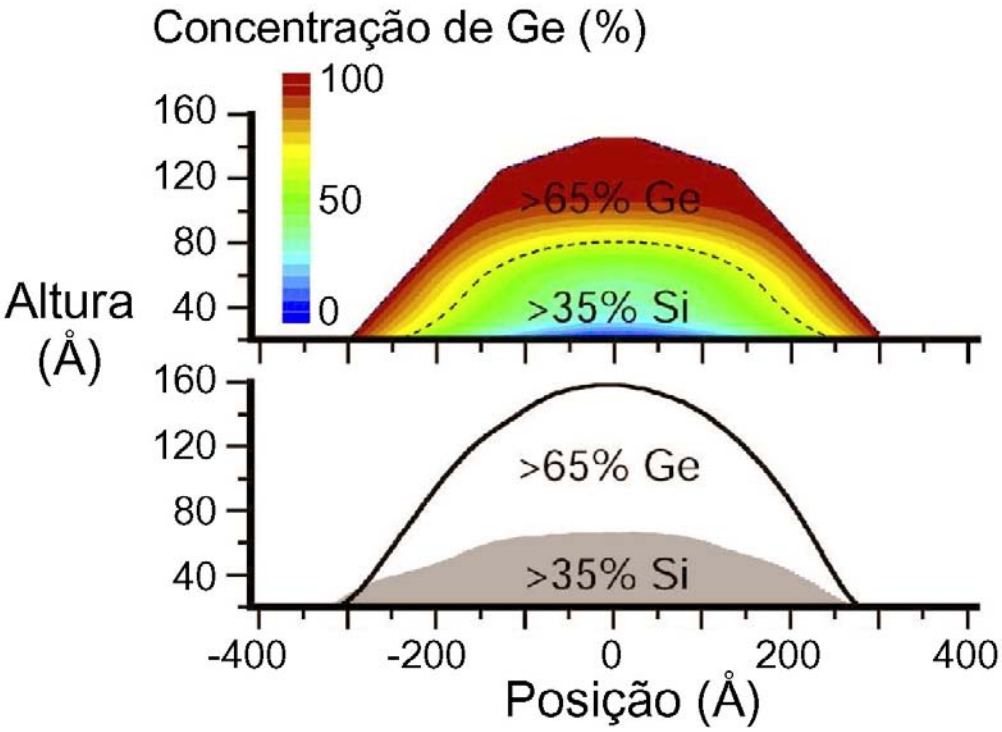

Fig. 6.14 – (a) Mapa de composição em espaço real para os domos de Ge; (b) perfis de AFM para domos de tamanho típico antes e depois do etching seletivo em solução de 31% H_2O_2, evidenciando o núcleo rico em Si.

6.2.5 – Mapeamento 3D da energia elástica para domos

A energia elástica dentro dos domos pode ser obtida para cada ponto através da eq. 6.11. Para isso basta substituir os valores de μ, ν e $\varepsilon_{\parallel}$ encontrados para cada concentração do mapa da fig. 6.14(a). A fig. 6.15 mostra o mapa de energia elástica para a amostra de domos. Como pode ser visto, a distribuição de energia elástica dentro dos domos não é uniforme. A borda exterior de Ge produz uma contribuição para a energia elástica cujo valor máximo é encontrado na base da ilha, aproximando-se do valor obtido para um filme de Ge puro em Si (cerca de 30meV/átomo). Este cinturão de energia ao redor da base da ilha pode ser um dos fatores responsáveis pela estabilidade do conjunto de ilhas em relação a um alargamento da distribuição de tamanhos [Shchukin95, Williams00].

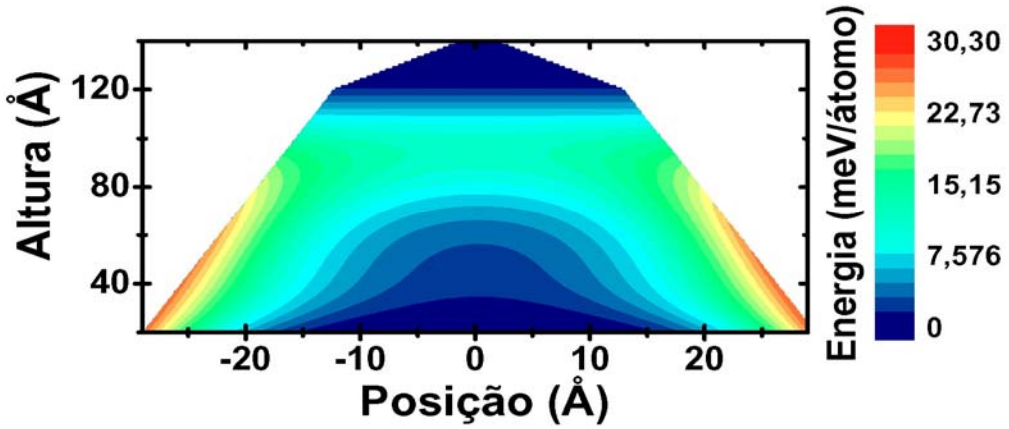

Fig. 6.15 – Mapa de energia elástica para a amostra de domos.

6.3 – Ordenamento atômico

Os resultados das seções anteriores demonstram a existência de interdifusão de Si nas ilhas de Ge. Embora os perfis de interdifusão tenham sido determinados com grande precisão (mapeamento 3D), não é possível atribuir a origem do Si dentro das ilhas a um processo termodinâmico e/ou cinético. A busca por ordenamento atômico nas ilhas pode auxiliar na solução desta questão.

6.3.1 – Ordenamento atômico em filmes de Ge:Si

Antes de 1985 filmes bidimensionais de Si:Ge eram considerados modelos para ligas aleatórias pois não era possível produzir ordem de longo alcance (como em $CuAu_3$) através de recozimentos (annealings) prolongados em uma grande faixa de temperaturas (170ºC – 925ºC) [Hansen58]. A descrição termodinâmica aplicada a esse sistema era o de "solução ideal" [Tsao93]. Em 1985 *Ourmazd* e *Bean* [Ourmazd85] observaram, por difração de elétrons, o ordenamento atômico em uma super-rede de $Si_{0.6}Ge_{0.4}$ crescida em Si(001). Tal ordenamento, na direção <111> não podia ser destruído por qualquer procedimento de recozimento/resfriamento a temperaturas de até 900ºC.

Após esse primeiro trabalho muito se especulou acerca da influência termodinâmica e do strain para o ordenamento atômico. *LeGoues* e colaboradores [LeGoues90b] mostraram de maneira unívoca a relação entre ordenamento e reconstrução da superfície durante a deposição de Ge. Em uma série de experimentos o ordenamento atômico foi observado apenas para uma reconstrução de superfície 2x1 na deposição da liga de Ge:Si sobre substrato de Si(001). Crescimentos realizados em substratos de Si(111) e/ou Si(001) com reconstrução 1x1 não produziram ordem entre as espécies atômicas. Essa origem cinética do ordenamento foi comprovada por outros grupos, que sugeriram mecanismos cinéticos condizentes com os resultados observados [Jesson91, Jesson93].

6.3.2 – Espectroscopia Raman e ordem de curto alcance

Embora o estudo de ordenamento tenha sido amplamente aplicado à ligas estequiométricas de GeSi nada foi feito em relação à possibilidade de ordenamento para o crescimento de Ge puro sobre Si(001). Nesta seção foram investigadas amostras onde Ge nominalmente puro foi depositado por epitaxia de feixe molecular (MBE) em substratos de Si(001) a temperaturas de 620ºC (amostra A), 700ºC (amostra B), 750ºC (amostra C) e 840ºC (amostra D). A quantidade de Ge depositada para as amostras A – D foi, em monocamadas (ML): 6.7ML (A), 11ML(B), 11ML(C) e 6ML(D). Em todas as amostra as medidas de AFM mostraram a existência de um conjunto monodisperso de domos. O grau de interdifusão médio nestas ilhas foi estudado por espalhamento anômalo de raios-x na referência [Schülli05]. A concentração média de Ge encontrada para cada amostra foi: 0,62 para a amostra A, 0,48 para a amostra B, 0,45 para a amostra C e 0,22 para a amostra D.

Para uma avaliação qualitativa de interdifusão e ordem de curto alcance medidas de espectroscopia Raman foram realizadas com um laser de Ar^+ (λ = 5145Å) com potência fixa em 8mW na superfície da amostra. Este experimento revela essencialmente a existência e abundância relativa de ligações de Ge-Ge e Si-Ge dentro das ilhas. A fig. 6.16 mostra o sinal Raman numa região entre 200 e 600 cm^{-1} para as quatro amostras e um substrato de Si. Os modos de vibração Ge-Ge, Si-Ge e Si-Si são observados em torno de 300, 400 e 500 cm^{-1}, respectivamente.

Uma análise qualitativa pode ser realizada comparando-se as intensidades do pico Si-Ge para todas as amostras. Essa intensidade é, grosso modo, proporcional a: (a) interdifusão, que introduz átomos de Si dentro das ilhas de Ge e; (b) ordenamento atômico de curto alcance, que maximiza o número de ligações Si-Ge. As medidas da fig. 6.16 revelam uma dependência da ordem de curto alcance com a temperatura. Como a amostra B possui o pico Si-Ge mais intenso, foi escolhida para uma análise completa por raios-x.

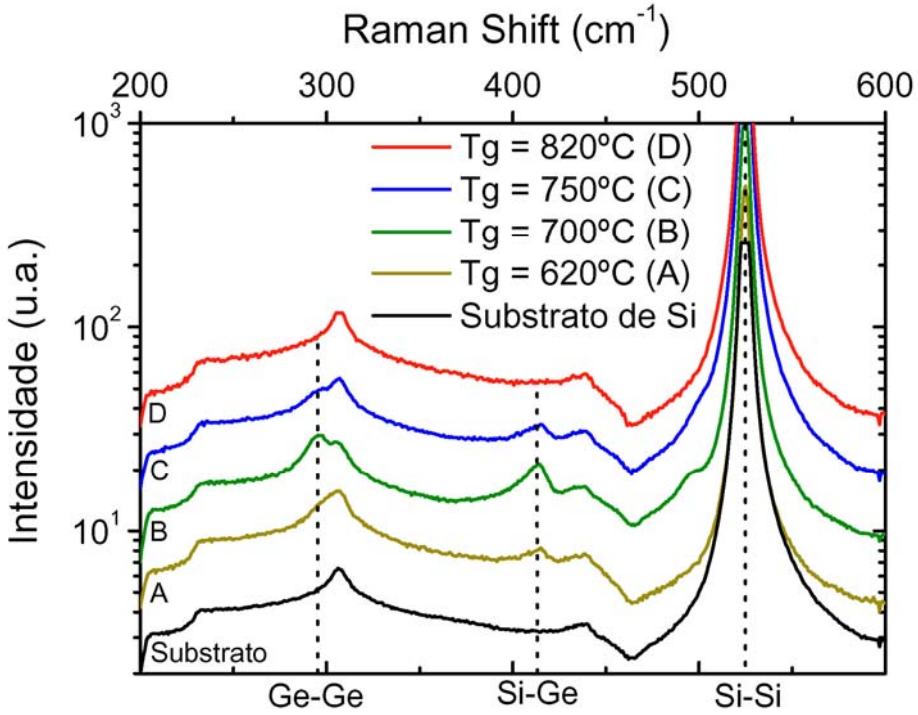

Fig. 6.16 – Espectro Raman para um substrato de Si(001) e amostras A, B, C e D. A posição dos picos Ge-Ge e Si-Ge são indicadas por linhas pontilhadas.

6.3.3 – Análise de ordenamento para a amostra B

As medidas de raios-x mostradas nesta seção foram realizadas na linha ID1 do síncrotron europeu ESRF. Foi utilizada a geometria GID com ângulo de incidência fixo em 0.17º e energia de 8keV. Mapas q_r-q_a no espaço recíproco foram medidos próximos a reflexões permitidas e de superestrutura.

Uma varredura radial ao longo da direção [100] nas vizinhanças do pico (400) do Si é vista na fig. 6.17(a), onde o eixo q_r foi diretamente convertido em parâmetro de rede (eixo horizontal superior). A distribuição alargada de intensidade que vai de 5,431Å a 5,60Å indica a relaxação do parâmetro de rede dentro das ilhas. Um resultado inesperado (a

princípio) é obtido quando o espalhamento é medido nas proximidades da reflexão (200), fig. 6.17(b), que é proibida para Si e Ge puros. Nesta condição de Bragg a intensidade espalhada só é observada caso a liga de SiGe esteja parcialmente ordenada. Esta é a primeira evidência de que ordem de longo alcance pode ser encontrada neste sistema. Enquanto a relaxação total das ilhas de Ge alcança um parâmetro de rede máximo de 5,60Å a liga ordenada encontra-se restrita a uma faixa de parâmetros de rede entre 5.44Å e 5.54Å.

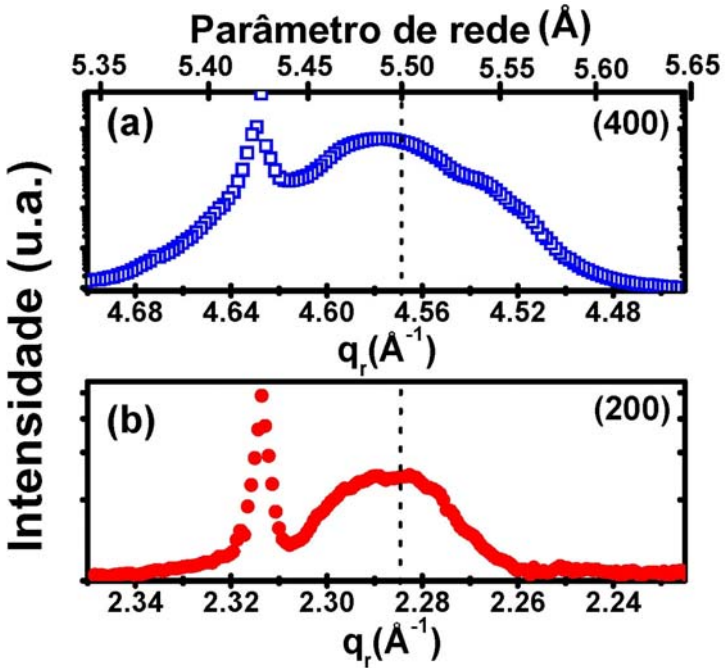

Fig. 6.17 – Varreduras radiais ao longo de q_r nas vizinhanças de (a) reflexão (400) – quadrados e (b) reflexão (200) – círculos. A escala superior indica o parâmetro de rede no plano.

Para efetuar uma análise completa do strain é necessário utilizar a informação proveniente de varreduras angulares. Neste caso é necessário conhecer o fator de forma de cada região de parâmetro de rede fixo dentro das ilhas. Efetuando-se varreduras angulares para um parâmetro de rede fixo (na posição marcada pelas linhas pontilhadas na fig. 6.17) pode-se observar os perfis mostrados na fig. 6.18. Uma varredura angular (fig. 6.18(a)) próxima à reflexão (400) exibe um máximo central em $q_a = 0$ e máximos laterais que indicam a estreita distribuição de tamanho das regiões de iso-parâmetro de rede. Todavia, para a reflexão (200), um corte angular medido com $q_r = 2\pi/(5.50Å)$ gera um perfil muito diferente. Um mínimo de intensidade bastante pronunciado é observado para $q_a = 0$ e não

pode ser gerado por estruturas com interferência construtiva. Esse perfil só pode ser ajustado introduzindo-se fronteiras de anti-fase entre domínios ordenados dentro das ilhas.

Outras reflexões de superestrutura, como (420) e (110) também foram medidas e perfis de espalhamento consistente com o modelo cristalográfico da referência [Tischler95] foram encontrados. Para descartar a possibilidade de espalhamento por estruturas "giradas" as varreduras angulares das reflexões (200) e (420) foram representadas na fig. 6.18(b) em função do ângulo $\omega = \Delta\theta$ em espaço real.

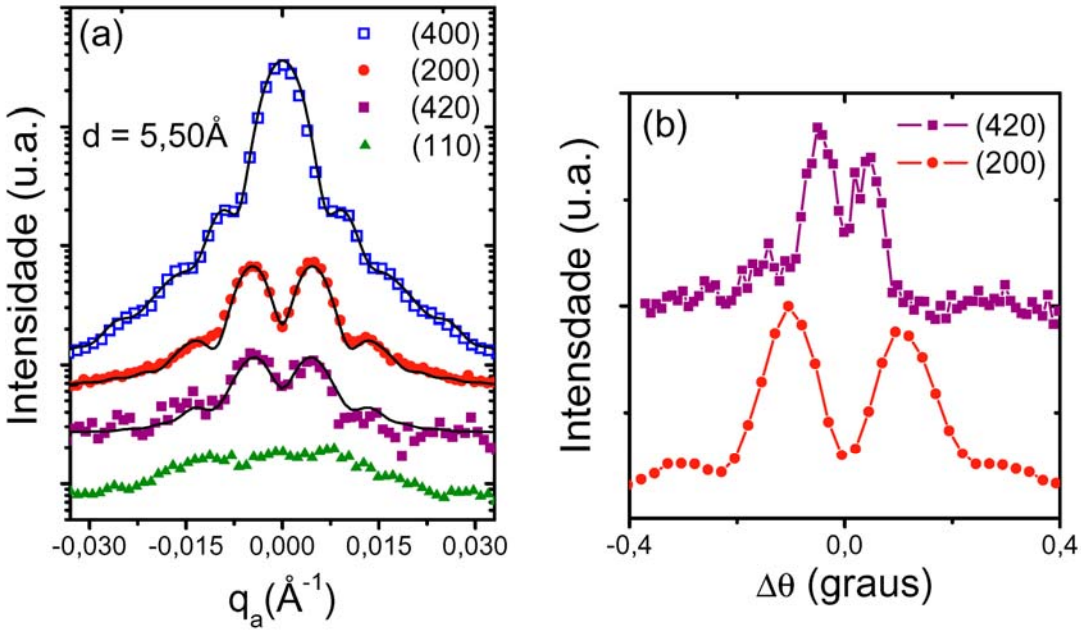

Fig. 6.18 – (a) Varreduras angulares na a amostra B com $q_r = 2\pi/(5.50\text{Å})$ em quatro reflexões: (400) quadrados vazados; (200) círculos; (420) quadrados cheios e (110) triângulos. (b) Varreduras angulares próximas às reflexões (200) e (420) de (a) em função do ângulo em espaço real.

Dois fatores de forma distintos serão utilizados aqui. Para a reflexão (400) todo o material dentro de um domo de Ge contribui para a intensidade espalhada. Nesse caso o perfil na direção angular pode ser representado (de maneira simplificada) por [Warren69, Kegel99]

$$I(q_a) = \frac{I_0}{L^2}\left|\frac{sen\left(L/2\, q_a\right)}{sen(q_a)}\right|^2, \qquad (6.14)$$

onde L é a dimensão lateral da região de parâmetro de rede fixo.

No caso da reflexão (200) existe uma dependência da intensidade espalhada com relação ao grau de ordenamento do material dentro da ilha. Se a região de iso-parâmetro de rede é perfeitamente ordenada a varredura angular terá o perfil descrito pela eq. 6.14. Contudo, uma camada atômica pode estar dividida em pequenas regiões ordenadas separadas por fronteiras de anti-fase. Estas fronteiras são geradas por defeitos na seqüência atômica. Pode haver uma quebra em uma seqüência perfeita de átomos da forma …Si-Ge-Si-Ge-Si-Ge… onde um átomo de Si ou Ge estaria fora do lugar, formando a nova seqüência …Si-Ge-Si-Si-Ge-Si…. Considerando-se que o parâmetro de rede é aproximadamente constante para um plano paralelo à superfície do substrato a quebra de seqüência causada por ligações Si-Si ou Ge-Ge causa uma inversão na fase da onda de raio-x [Li03, Warren69]. O novo fator de forma para este caso, semelhante à eq. 6.14, deve incluir um termo de inversão de fase. A função resultante (simplificada) para o caso de domínios separados por uma fronteira de anti-fase pode ser escrita como:

$$I(q_a) = \frac{I_0}{N^2 d^2} \left| sin(Ndq_a) \cdot \frac{sin(Ndq_a)}{sin(q_a)} \right|^2 , \qquad (6.15)$$

onde Nd é o tamanho do domínio ordenado (N é o número de átomos em um domínio e d o parâmetro de rede). Os perfis angulares que resultam das eqs. 6.14 e 6.15 são vistos na fig. 6.19.

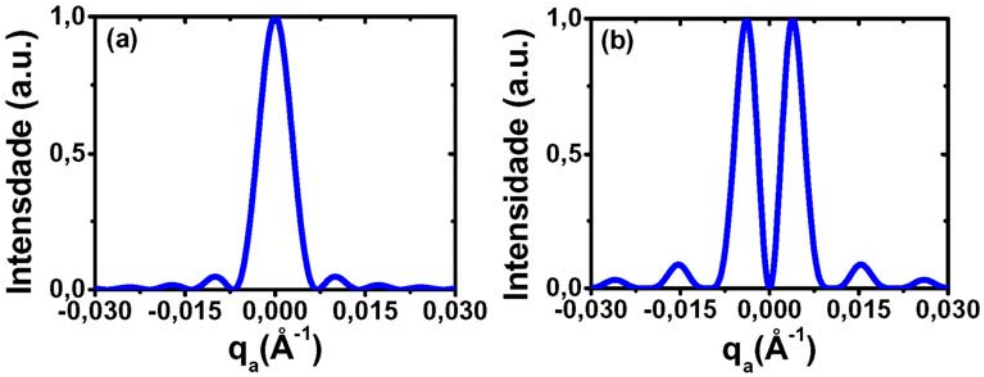

Fig. 6.19 – Fatores de forma para (a) uma camada atômica de 900Å (eq. 6.14) e (b) dois domínios em anti-fase com 300Å cada um (eq. 6.15).

O mapeamento completo nas vizinhanças da reflexão (200) do Si é mostrado na fig. 6.20(a). A estrutura de pico duplo é observada na região da liga deformada, de $q_r = 2.31Å^{-1}$ a $q_r = 2.27Å^{-1}$. A largura da estrutura de pico duplo aumenta para valores menores de q_r,

indicando uma redução das dimensões laterais dos domínios ordenados em espaço real para parâmetros de rede mais próximos ao Ge.

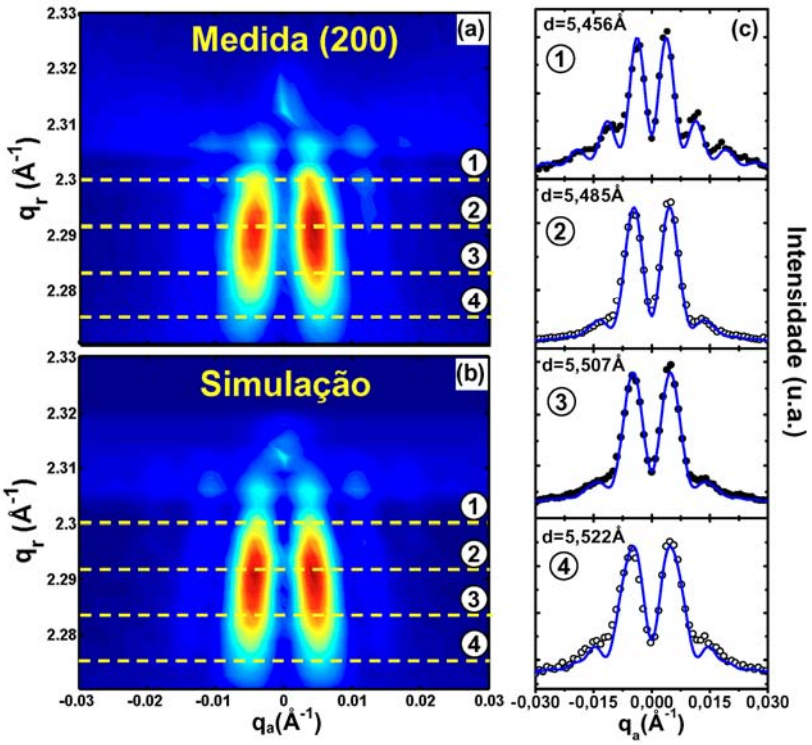

Fig. 6.20 – (a) Mapa q_r-q_a medido para a amostra B nas vizinhanças da reflexão (200) do Si. (b) Simulação do mapa experimental baseada em ajuste para todo o conjunto de varreduras angulares. Quatro varreduras angulares, correspondentes às linhas pontilhadas em (a) e (b) aparecem em (c). Os pontos representam as medidas extraídas de (a) enquanto as linhas sólidas são ajustes retirados do mapa (b).

O mapa visto na fig. 6.20(b) foi obtido utilizando a eq. 6.15 de modo a ajustar os perfis angulares que compõem a fig. 6.20(a). Algumas varreduras angulares aparecem com seus respectivos ajustes na fig. 6.20(c). A possível interferência entre domínios em anti-fase pertencentes a ilhas distintas foi excluída por meio de uma simulação com funções de correlação, que não puderam reproduzir os perfis observados.

Uma comparação entre o tamanho da ilha e o tamanho dos domínios na amostra B é vista na fig. 6.21(a). A informação acerca do tamanho do domínio foi obtida através da análise da reflexão (200), vista na fig. 6.20, sendo que o tamanho das seções laterais da ilha foi extraído dos perfis angulares da reflexão (400) (dados experimentais não são mostrados aqui) [Malachias01, Schülli03a]. Considerando que uma região ordenada sofre a mesma relaxação de strain que uma região de mesmo parâmetro de rede dentro da ilha foi possível

associar strain e altura a partir dos resultados da reflexão (400) e dados de AFM (como visto na seção 6.2). A posição dos domínios ordenados dentro dos domos de Ge é representada esquematicamente na fig. 6.21(b).

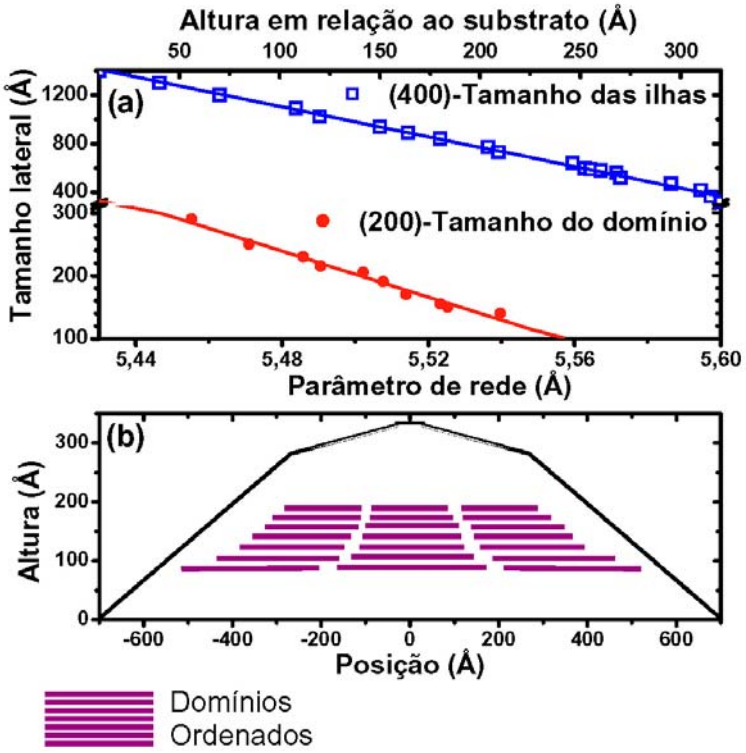

Fig. 6.21 – (a) tamanho da ilhas e domínios ordenados da amostra B em função do parâmetro de rede no plano e altura em relação ao substrato. (b) Representação esquemática da localização dos domínios ordenados dentro das ilhas da amostra B.

6.3.4 – Parâmetro de ordem S para a série de amostras

Utilizando-se a razão entre intensidades das reflexões (200) e (400) para as amostras A, B, C e D foi possível obter o parâmetro de ordem para cada temperatura de crescimento. Utilizando-se a eq. 6.7 foram encontrados valores relativamente altos para S em todas as amostras. Este conjunto de resultados, visto na fig. 6.22, foi qualitativamente corroborado pela razão de intensidades entre os picos Raman Si-Ge e Ge-Ge (I_{SiGe}/I_{GeGe}) que representa a abundância relativa de ligações Si-Ge (parâmetro de ordem de curto alcance) dentro das ilhas [Finkman01, Dvurechenskii04].

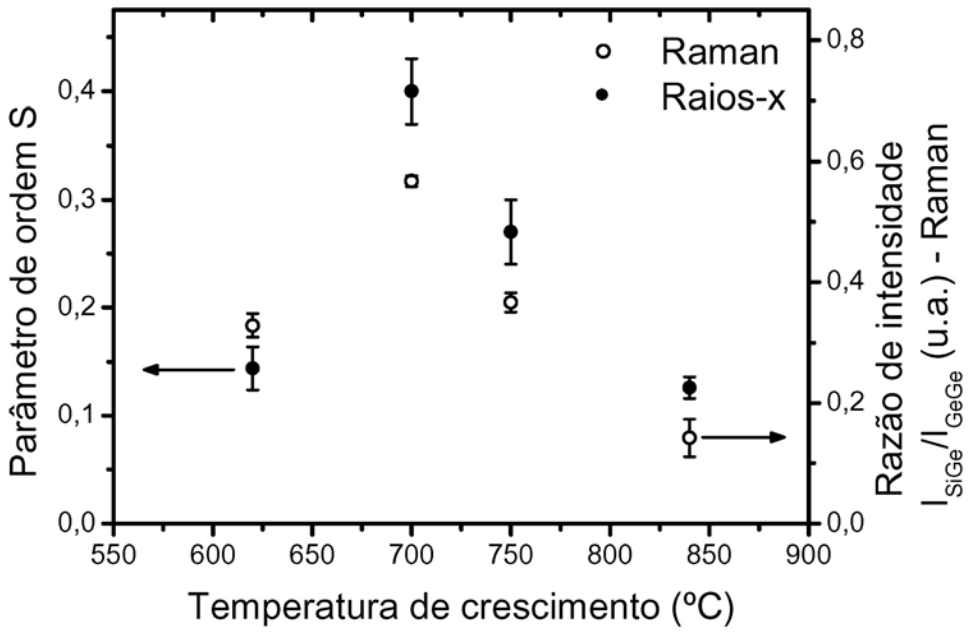

Fig. 6.22 – Parâmetro de ordem S obtido por raios-x e razão entre as intensidades Raman para os picos Si-Ge e Ge-Ge para a série de amostras descritas nesta seção.

6.4 – Conclusões

Ilhas de Ge em Si(001) têm sido estudadas como um modelo para crescimento de ilhas no modo Stranski-Krastanov pois apenas dois elementos estão envolvidos. Neste trabalho, técnicas de espalhamento de raios-x foram utilizadas para investigar as propriedades estruturais das ilhas que podem influenciar, de maneira relevante, a resposta optoeletrônica de dispositivos baseados nesses materiais.

A técnica de difração por incidência rasante (GID) provou ser altamente sensível à variações do parâmetro de rede dentro das ilhas, bem como a características morfológicas como tamanho e formato das mesmas. Medidas com contraste químico foram realizadas com o uso de espalhamento anômalo. Correlacionando os resultados de composição e strain foi possível constatar, diretamente, a redução de energia elástica durante as transições wetting-layer–pirâmide e pirâmide–domo. Tal redução é provavelmente o mecanismo mais importante que determina as transições de formato no sistema Ge:Si. Através de uma extensão destes métodos foram produzidos mapas tri-dimensionais de strain, composição

química e energia elástica dentro dos domos. Por fim, reflexões de superestrutura revelaram a formação de ligas atomicamente ordenadas em um conjunto de amostras crescidas a diferentes temperaturas. Este resultado, corroborado de maneira independente por medidas de Raman implica na existência de um mecanismo cinético que influencia (e talvez governe) a interdifusão de Si.

References

[AlsNielsen01] J. Als-Nielsen and D. McMorrow, *Elements of modern X-ray physics*, Wiley, New York (2001).

[Ahrenkiel99] S.P. Ahrenkiel *et. al.*, Appl. Phys. Lett., **74**, 3534 (1999).

[Chaparro99] S. A. Chaparro, Jeff Drucker, Y. Zhang, D. Chandrasekhar, M. R. McCartney, D. J. Smith, Phys. Rev. Lett, **83**, 1199 (1999).

[Chaparro00] S. A. Chaparro, Y. Zhang, Jeff Drucker, Appl. Phys. Lett., **76**, 3534 (2000).

[Cowley81] J. M. Cowley, *Diffraction Physics*, North-Holland, Amsterdam (1981).

[Cui03] J. Cui, Q. He, X. M. Jiang, Y. L. Fan, X. J. Yang, F. Xue, Z. M. Jianga, Appl. Phys. Lett., **83**, 2907 (2003).

[Cullis02] A. G. Cullis, D. J. Norris, T. Walther, M. A. Migliorato, M. Hopkinson, Phys. Rev. B, **66**, 81305 (2002).

[Denker03] U. Denker, M. Stoffel, O. G. Schmidt, Prys. Rev. Lett., **90**, 196102 (2003).

[Dorsch97] W. Dorsch, H. P. Strunk, H. Wawra, G. Wagner, J. Groenen, R. Carles, Appl. Phys. Lett., **72**, 179 (1997).

[Dosch92] H.Dosch, *Critical phenomena at surfaces and interfaces. Evanescent X-ray and neutron scattering*, Springer, Berlin (1992).

[Dvurechenskii04] A. V. Dvurechenskii2004, Zh. V. Smagina, V. A. Zinov'ev, V. A. Armbrister, V. A. Volodin, M. D. Efremov, JETP Lett., **79**, 333 (2004).

[Finkman2001] E. Finkman, F. Meyer, M. Mamor, Journal of Appl. Phys. **89**, 2580 (2001).

[Floyd03] M. Floyd, Y. Zhang, K. P. Driver, Jeff Drucker, P.A. Crozier, D. J. Smith, Appl. Phys. Lett., **82**, 1473 (2003).

[Garcia97] J. M. Garcia, G. Medeiros-Ribeiro, K. Schmidt, T. Ngo, J. L. Feng, A. Lorke, J. Kotthaus, P. M. Petroff, Appl. Phys. Lett., **71**, 2014 (1997).

[Hansen58] M. Hansen, *Constitution of Binary Alloys*, McGraw-Hill (New York), 1958, 2nd ed.

[Ide99] T. Ide, A. Sakai, K. Shimizu, Thin Solid Films, **357**, 22 (1999).

[Jackson99] J. D. Jackson, *Classical Electrodynamics (3rd ed.)*, John Wiley & Sons (1999).

[Jesson91] D. E. Jesson, S. J. Pennycook, J.-M. Baribeau, Phys. Rev. Lett., **66**, 750 (1991).

[Jesson92] D. E. Jesson, S. J. Pennycook, J.-M. Baribeau, D. C. Houghton, Phys. Rev. Lett., **68**, 2062 (1992).

[Jesson93] D. E. Jesson, S. J. Pennycook, J. Z. Tischler, J. D. Budai, J.-M. Baribeau, D.C. Houghton, Phys. Rev. Lett., **70**, 2293 (1993).

[Kamins98] T. I. Kamins, G. Medeiros-Ribeiro, D. A. A. Ohlberg, R. S. Williams, Appl. Phys. A, **67**, 727 (1998).

[Kamins99] T. I. Kamins, G. Medeiros-Ribeiro, D. A. A. Ohlberg, R. S. Williams, J. Appl. Phys., **85**, 1159 (1999).

[Kegel99] I. Kegel, T. H. Metzger, P. Fratz, J. Peisl, A. Lorke, J. M. Garcia, P. M. Petroff, Europhys. Lett., **45**, 222 (1999).

[Kegel01] I. Kegel, T. H. Metzger, A. Lorke, J. Peisl, J. Stangl, G. Bauer, K. Nordlund, W. V. Schoenfeld, P. M. Petroff, Phys. Rev. B, **63**, 035318 (2001).

[Kesan92] V.P. Kesan, F.K. LeGoues, S.S. Iyer, Phys. Rev. B, **46**, 1576 (1992).

[Landau59] L. D. Landau, *Theory of Elasticity*, Pergamon Press (1959).

[LandoltBornstein82] Landolt-Bornstein, Volume 17 (subvolume a), *Physics of Group IV Elements and III-V Compounds*, Springer-Verlag, Berlin (1982).

[LeGoues90a] F. K. LeGoues, V. P. Kesan, S. S. Iyer, Phys. Rev. Lett., **64**, 40.

[LeGoues90b] F. K. LeGoues, V. P. Kesan, S. S. Iyer, J. Tersoff, R. Tromp, Phys. Rev. Lett., **64**, 2038.

[Li03] J. H. Li, S. C. Moss, Y. Zhang, A. Mascarenhas, L. N. Pfeiffer, K. W. West, W. K. Ge, J. Bai, Phys. Rev. Lett. **91**, 106103 (2003).

[Liao02] X.Z. Liao, J. Zou, D. J. H. Cockayne, J. Wan, Z. M. Jiang, G. Jin, K. L. Wang, Phys. Rev. B, **65**, 153306 (2002).

[Liao99] X.Z. Liao, J. Zou, D. J. H. Cockayne, J. Qin, J. M. Jiang, X. Wang, R. Leon, Phys. Rev. B **60**, 15605 (1999).

[Littlewood86] P.B. Littlewood, Phys. Rev. B, **34**, 1363 (1986).

[Liu00] N. Liu, J. Tersoff, O. Baklenov, A. L. Holmes Jr., C. K. Shih, Phys. Rev. Lett., **84**, 334 (2000).

[Lockwood87] D. J. Lockwood, K. Rajan, E. W. Fenton, J.-M. Baribeau, M. W. Denhoff, Solid State Comm. **61**, 465 (1987)

[MagalhãesPaniago02] R. Magalhães-Paniago, G. Medeiros-Ribeiro, A. Malachias, S. Kycia, T. I. Kamins, and R. S. Williams, Phys. Rev. B, **66**, 245312 (2002).

[Malachias01] A. Malachias, R. Magalhães-Paniago, B. R. A. Neves, W. N. Rodrigues, M. V. B. Moreira, H. D. Pfannes, A. G. de Oliveira, S. Kycia, T. H. Metzger, Appl. Phys. Lett., **79**, 4342 (2001).

[Malachias02] A. Malachias, M. Sc. Thesis, UFMG, Brazil (2002).

[Malachias03a] A. Malachias, R. Magalhães-Paniago, G. Medeiros-Ribeiro, S. Kycia, T. I. Kamins, and R. S. Williams, Mat. Res. Soc. Symp. Proc. **737**, F2.5.1 (2003).

[Malachias03b] A. Malachias, W. N. Rodrigues, M. V. B. Moreira, S. Kycia, R. Magalhaes-Paniago, Journal of Phys. D, **36**, A249 (2003)

[Malachias03c] A. Malachias, S. Kycia, G. Medeiros-Ribeiro, R. Magalhães-Paniago, T. I. Kamins, R. Stanley Williams, *Phys. Rev. Lett.* **91**, 176101 (2003)

[Martins86] J.L. Martins, A. Zunger, Phys. Rev. Lett., **56**, 1400 (1986).

[MedeirosRibeiro98] G. Medeiros-Ribeiro, A. M. Bratkovski, T. I. Kamins, D. A. A. Ohlberg, R. S. Williams, Science, **279**, 353 (1998).

[MedeirosRibeiro05] G. Medeiros-Ribeiro, A. Malachias, S. Kycia, R. Magalhães-Paniago, T. I. Kamins, R. S. Williams, Appl. Phys. A, **80**, 1211 (2005).

[Metzger98] T. H. Metzger, I.Kegel, R. Paniago, A. Lorke, J. Peisl, Thin Solid Films, **336**, 1 (1998).

[Michette96] A. Michette, S. Pfauntsch, *X-RAYS: The First Hundred Years*, John Wiley & Sons, (1996).

[Montalenti04] F. Montalenti, P. Raiteri, D.B. Migas, H. von Kanel, A. Rastelli, C. Manzano, G. Costantini, U. Denker, O. G. Schmidt, K. Kern, L. Miglio, Phys. Rev. Lett., **93**, 216102 (2004).

[Muller89] E. Muller, H.-U. Nissen, M. Ospelt, H. von Kanel, Phys. Rev. Lett.,**63**, 1819.

[Nakajima99] K. Nakajima, A. Konishi, K. Kimura, Phys. Rev. Lett., **83**, 1802 (1999).

[Ourmazd85] A. Ourmazd, J.C. Bean, Phys. Rev. Lett., **55**, 765 (1985).

[Pietsch04] U. Pietsch, V. Holy, T. Baumbach, *High Resolution X-ray Scattering from Thin Films and Lateral Nanostructures (2nd ed.)*, Springer, Berlin (2004).

[Qteish88] A. Qteish, R. Resta, Phys. Rev. B, **37**, 6983 (1988).

[Raiteri02] P. Raiteri, Leo Miglio, F. Valentinotti, M. Celino, Appl. Phys. Lett., **80**, 3736 (2002).

[Rastelli01] A. Rastelli, M. Kummer, H. von Känel, Phys. Rev. Lett., **87**, 256101 (2001).

[Rastelli02] A. Rastelli, PhD thesis, Dipartimento di Fisica “A. Volta”, Università degli Studi di Pavia (2002).

[Rauscher99] M. Rauscher, R. Magalhães-Paniago, H. Metzger, J. Domke, J. Peisl, H.-D. Pfannes, J. Schulze, I. Eisele, J. Appl. Phys., **86**, 6763 (1999).

[Reichert99] H. Reichert, S. C. Moss, P. Imperatori, K. Evans-lutterodt, Appl. Phys. Lett. , **74**, 531 (1999).

[Robinson86] I. K. Robinson, Phys. Rev. B, **33**, 3830 (1986).

[Ross98] F. Ross, J. Tersoff, R. M. Tromp, Phys. Rev. Lett., **80**, 984 (1998).

[Ross99] F. Ross, R. Tromp, M. Reuter, Science, **286**, 1931 (1999).

[Schmidt02] O. G. Schmidt, U. Denker, S. Christiansen, F. Ernst, Appl. Phys. Lett., **81**, 2614 (2002).

[Schülli03a] T. U. Schülli, J. Stangl, Z. Zhong, R. T. Lechner, M. Sztucki, T. H. Metzger, G.Bauer, Phys. Rev. Lett., **90**, 066105 (2003).

[Schülli03b] T. U. Schülli, PhD thesis, Institut für Halbleiterphysik der Johannes Kepler Universität Linz (2003).

[Schülli05] T. U. Schülli, M. Stoffel, A. Hesse, J. Stangl, R. T. Lechner, E. Wintersberger, M. Sztucki, T. H. Metzger, O. G. Schmidt, G. Bauer, Phys. Rev. B, **71**, 035326 (2005).

[SchülliHP] http://www.schuelli.com/physics/kkpage.html

[Shchukin95] V. A. Shchukin, N. N. Ledenstov, P. S. Kop'ev, D. Bimberg, Phys. Rev. Lett., **75**, 2968 (1995).

[Springholz98] G. Springholz, V. Holy, M. Pinczolits, G. Bauer, Science, **282**, 734 (1998).

[StranskiKrastanov39] I. N. Stranski, L. von Krastanov, *Akad. Wiss. Let. Mainz Math-Natur. KL Iib*, **146**, 797 (1939).

[Tambe04] D. T. Tambe, V. B. Shenoy, Appl. Phys. Lett., **85**, 1586 (2004).

[Tersoff98] J. tersoff, Phys. Rev. Lett., **81**, 3183 (1998).

[Tischler95] J. Z. Tischler, J. D. Budai, D. E. Jesson, G. Eres, P. Zscack, J. M. Baribeau, D.C. Houghton, Phys. Rev. B **51**, 10947 (1995).

[Tsao93] J. Y. Tsao, *Materials Fundamentals of Molecular Beam Epitaxy*, Academic Press, London (1993).

[Vailionis00] A. Vailionis, B. Cho, G. Glass, P. Desjardins, D. G. Cahill, J. E. Greene, Phys. Rev. Lett., **85**, 3672 (2000)

[Venezuela99] P. Venezuela, J. Tersoff, J. A. Floro, E. Chason, D. M. Follstaedt, F. Liu, M. G. Lagally, Nature, **397**, 678 (1999).

[Vineyard82] G. H. Vineyard, Phys. Rev. B, **26**, 4146 (1982).

[Warren69] B. E. Warren, *X-Ray Diffraction*, Dover Publications (1969).

[Williams00] R. S. Williams, G. Medeiros-Ribeiro, T. I. Kamins, D. A. A. Ohlberg, Annu. Rev. Phys. Chem., **51**, 527 (2000).

[Wong00] G. C. L. Wong, J. X. Tang, A. Lin, Y. L. Li, P. A. Janmey, C.R. Safinya, Science, **288**, 2035 (2000).

[Yu97] W. Yu, A. Madhukar, Phys. Rev. Lett., **79**, 905 (1997).

[Zangenberg01] N. R. Zangenberg, J. L. Hansen, J. F. Pedersen, A. N. Larsen, Phys. Rev. Lett., **87**, 125901 (2001).

[Zhang00] K. Zhang, Ch. Heyn, W. Hansen. Th. Schmidt, J. Falta, Appl. Phys. Lett., **77**, 1295 (2000).

[Zhang01] Y. Zhang, M. Floyd, Jeff Drucker, G. L. Kellogg, J. Appl. Phys., **90**, 4748 (2001)

[Zhang03] Y. Zhang, Jeff Drucker, J. Appl. Phys., **93**, 9583 (2003).

List of publications (2002 – 2005)

1. ***Atomic Ordering in Self-Assembled Ge:Si(001) islands observed by X-ray Scattering*** – A. Malachias, T. U. Schulli, G. Medeiros-Ribeiro, M. Stoffel, O. Schmidt, T. H. Metzger, R. Magalhães-Paniago – Physical Review B, **72**, 165315 (2005).

2. ***Elastic Energy Mapping of Epitaxial Nanocrystals*** – G. Medeiros-Ribeiro, A. Malachias, S. Kycia, R. Magalhães-Paniago, T.I. Kamins, R.S. Williams – Applied Physics A, Materials science & processing, **80**, 1211 (2005).

3. ***Measurement of Si 311 defect properties using x-ray scattering*** – K. Nordlund, T.H. Metzger, A. Malachias, L. Capello, P. Calvo, A. Claverie, F. Cristiano – Journal of Applied Physics, **98**, 073529 (2005).

4. ***X-ray scattering from self-assembled InAs islands*** – A. Malachias, W.N. Rodrigues, M.V.B. Moreira, S. Kycia, T. H. Metzger, R. Magalhães-Paniago – Brazilian Journal of Physics, **34**, 571 (2004).

5. ***X-ray study of strain and composition of Si/Ge0.85Si0.15 (111) islands grown in Volmer-Weber mode*** – A. Malachias, R. Magalhães-Paniago, S. Kycia, D.G. Cahill, Journal of Applied Physics, **96**, 3234 (2004).

6. ***3D composition of epitaxial nanocrystals by anomalous x-ray diffraction: observation of a Si-rich core in Ge domes on Si(001)*** – A. Malachias, S. Kycia, G. Medeiros-Ribeiro, R. Magalhães-Paniago, T.I. Kamins, R.S. Williams – Physical Review Letters, **91**, 176101 (2003).

7. ***Anomalous x-ray scattering on self-assembled islands: direct evaluation of composition profile, strain relaxation and elastic energy*** – A. Malachias, R. Magalhães-Paniago, G. Medeiros-Ribeiro, S. Kycia, T.I. Kamins, R.S. Williams – Materials Research Society Symposia Proceedings, **737**, 2.5.1 (2003).

8. ***Determination of Ga Interdiffusion in InAs:GaAs(001) Islands by X-ray Reciprocal Space Mapping*** – A. Malachias, W.N. Rodrigues, M.V.B. Moreira, S. Kycia, R. Magalhães-Paniago – Journal of Physics D (Applied Physics), **36**, A249 (2003).

9. ***Structural Investigations of Octadecylphosphonic Acid Multilayers*** – G.N. Fontes, A. Malachias, R. Magalhães-Paniago, B.R.A. Neves – Langmuir, **19**, 3345 (2003).

10. ***Direct Evaluation of Composition Profile, Strain Relaxation and Elastic Energy of Ge:Si (001) Self-Assembled Islands by Anomalous X-ray Scattering*** – R. Magalhães-Paniago, G. Medeiros-Ribeiro, A. Malachias, S. Kycia, T.I. Kamins, R.S. Williams – Physical Review B, **66**, 45312 (2002).

Appendix A

List of samples

Chapter	Sample Name	Growth Method	Growth Temperature	Ge Coverage (ML)	Growth rate (ML/s)	Grown at
2	Pyr	CVD	600ºC	3.5	0.1	HP[1]
2-3	Dome-A	CVD	600ºC	11.2	0.05	HP[1]
3	Dome-B	MBE	700ºC	12	0.02	LNLS[2]
4	A (Domes)	MBE	620ºC	6.7	0.05	MPI[3]
4	B (Domes)	MBE	700ºC	11	0.05	MPI[3]
4	C (Domes)	MBE	750ºC	11	0.05	MPI[3]
4	D (Domes)	MBE	840ºC	6	0.05	MPI[3]

[1] Hewlett-Packard Laboratories, 1501 Page Mill Rd., Palo Alto, CA 94117.
[2] Laboratório Nacional de Luz Síncrotron, Campinas, Brazil.
[3] Max-Planck-Institut für Festkörperforschung, Heisenbergstraße 1, D-70569 Stuttgart, Germany.

Appendix B

Publications which are not related to this thesis

INSTITUTE OF PHYSICS PUBLISHING JOURNAL OF PHYSICS D: APPLIED PHYSICS
J. Phys. D: Appl. Phys. **36** (2003) A249–A252 PII: S0022-3727(03)60472-9

Determination of Ga interdiffusion in InAs : GaAs(001) islands by x-ray reciprocal space mapping

A Malachias[1], W N Rodrigues[1], M V B Moreira[1], S Kycia[2] and R Magalhães-Paniago[1,2]

[1] Departamento de Física, Universidade Federal de Minas Gerais, C.P. 702, CEP 30123-970, Belo Horizonte, MG, Brazil
[2] Laboratório Nacional de Luz Síncrotron, C.P. 6192, CEP 13084-97, Campinas, SP, Brazil

E-mail: angeloms@fisica.ufmg.br (A Malachias)

Received 14 September 2002
Published 28 April 2003
Online at stacks.iop.org/JPhysD/36/A249

Abstract
Structural and chemical properties of self-assembled InAs islands grown on GaAs(001) were studied using x-ray scattering. Two measurements performed under grazing incidence geometry were correlated to obtain the three-dimensional strain and chemical status of InGaAs coherent islands. Grazing incidence diffraction was employed to reveal the in-plane strain-size interplay. Mapping out the reciprocal space near the GaAs(022) reflection and correlating the in-plane and out-of-plane strain information, we have been able to quantify the tetragonal distortion of the unit cells at any position inside the islands. Simple theory of elasticity of alloys enabled us to analyse the elastic deformation of the unit cells. Any variation in the expected tetragonal distortion of the unit cell was associated to the presence of Ga atoms inside the islands. Using this method, the Ga content in our islands was shown to vary linearly from 25% (island bottom) to 8% (island top).

1. Introduction

The electronic properties of self-assembled islands, such as InAs grown on GaAs(001) are extremely dependent on their inner strain and chemical state. Although a large number of variables rule island formation, only a few features of their final state determines their technological applicability: (a) absence of defects like dislocations or stacking faults, directly related to quantum efficiency of quantum dots; (b) morphological homogeneity, which gives optical and electronic response quality; and (c) elastic strain and intermixing.

It has been already recognized that InAs islands grown on GaAs exhibit a measurable degree of Ga intermixing [1]. While Ga distribution inside these islands cannot be mapped by scanning probe techniques, strain and interdiffusion can be clearly determined by x-ray scattering. Recently, Kegel *et al* [2] have been able to determine the degree of Ga intermixing in InAs islands grown on GaAs(001), using an unique feature of fundamental and superstructure surface reflections. A general tool for other systems, however, is still lacking. X-ray reciprocal space mapping has already been used to study self-assembled islands, mainly using strain models to reproduce the intensity maps [3, 4]. In this work, grazing incidence diffraction (GID) was used in combination with x-ray reciprocal space mapping to infer the three-dimensional strain and chemical status of InGaAs islands. With this information, the tetragonal distortion of all unit cells inside the islands was quantified. The interdiffusion profile was then deduced from the elastic distortion of the unit cell determined by the Poisson ratio of the InGaAs alloy.

2. Experiment

Our InAs quantum island sample was grown as follows [5]. A 0.25 μm GaAs buffer layer was grown by molecular beam epitaxy on a GaAs(001) substrate at 620°C. This buffer was followed by a 40 × AlAs(10 ML)/GaAs(10 ML) short period superlattice grown to inhibit the propagation of dislocations formed at the substrate–buffer interface. This superlattice was then covered by another 0.28 μm GaAs

layer. Finally, 3.0 monolayers (ML) of InAs were deposited at 530°C and a rate of 0.16 ML s^{-1}. Atomic force microscopy measurements of the surface of the sample confirmed the formation of randomly distributed monodisperse islands, with a base diameter distribution of 320 ± 80 Å and a height of 100 ± 30 Å.

The scattering measurements were performed at the XD2 beamline at the Brazilian Synchrotron Light Source (Laboratório Nacional de Luz Síncrotron), in Campinas, Brazil. This beamline is equipped with a double bounce sagitally focused Si(111) monochromator and a standard four-circle diffractometer. First, GID measurements were done as a function of ω (sample rotation angle) and 2θ(scattering angle) near the GaAs(400) reflection. The incident angle α_i was set to 0.3° by an independent circle and the scattering was collected integrating the exit angle α_f from 0° to 1° by a position sensitive detector. The x-ray scattering was measured as a function of $q_{\text{angular}} = 4\pi/\lambda \sin(2\theta/2) \sin(\omega - 2\theta/2)$ (which is size sensitive) with $q_{\text{radial}} = 4\pi/\lambda \sin(2\theta/2)$ (which is strain sensitive) fixed [2, 5]. α_f-profiles (not shown here) revealed the height with respect to the substrate of specific regions of the islands with lattice parameter $a_{\parallel} = 2\pi/q_{\text{radial}}$ [2].

Following the GID measurements, x-ray reciprocal space mapping (in fixed incident angle mode) near the substrate GaAs(022) reflection was performed. The incidence angle α_i was set to 0.1° to maximize the islands/substrate signal ratio. The x-ray mapping was measured by a point scintillation detector, spanning from the InAs(022) peak position up to the GaAs(022) position.

3. Results and analysis

Figure 1 shows angular scans for our samples with q_{radial} fixed. The scans start near the GaAs reciprocal lattice point ($q_{\text{radial}} = 4.41$ Å^{-1}) and go up to the InAs position ($q_r = 4.25$ Å^{-1}). Since the full-width at half-maximum of these diffraction profiles is inversely proportional to the diameter of the scattering object $D = 2\pi/\Delta q_a$, a direct relationship between lateral lattice parameter $a_{\parallel}$ and the local diameter of the island D was obtained. Since there is a monotonic change of the width of the diffraction profile as a function of q_r, there is a gradual variation of the island diameter as a function of lattice parameter [2]. However, no out-of-plane strain information can be obtained in such a scan. Therefore, this result was correlated with reciprocal space mapping of an out-of-plane reflection.

Figure 2 shows the reciprocal space intensity map of the x-ray scattering stemming from our island sample. The difference of lattice parameter between InAs, $a = 6.06$ Å to GaAs, $a = 5.65$ Å, is 7%. This rectangular reciprocal space map scan starts near the position of the relaxed (022) InAs reflection and goes up to the position of the (022) GaAs substrate peak, spanning from $K = L = 1.76$ RLU until $K = 2.10$ RLU and $L = 2.0$ RLU. Two main contributions can be qualitatively identified. First, we clearly observe the crystal truncation rod along the 001 direction crossing the (022) GaAs peak, parallel to the GaAs surface normal. We also observe the island scattering intensity distribution, which already shows the sign of the tetragonal distortion of the island lattice. The lateral (in-plane) compression of the

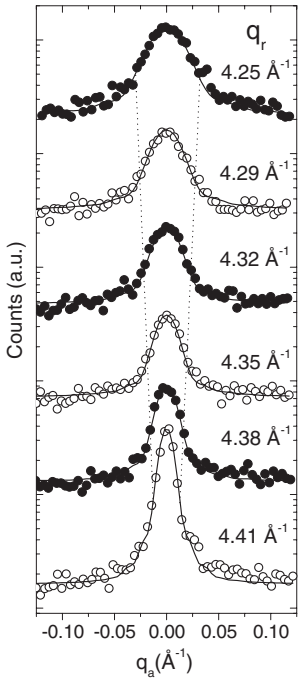

Figure 1. (400) angular scans at different radial positions for the InAs : GaAs(001) island sample. Dashed lines were drawn to indicate the approximate width of each angular scan.

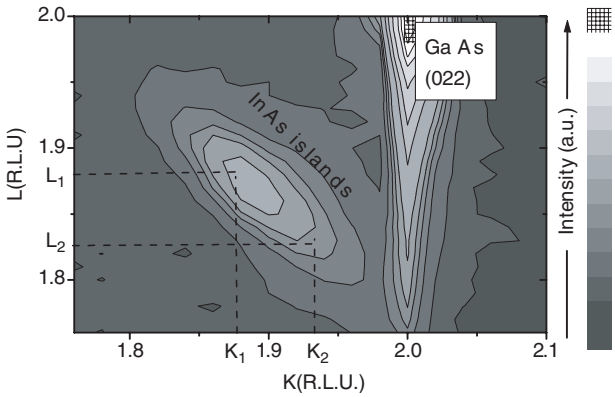

Figure 2. Log plots of the x-ray reciprocal space map of InAs/GaAs(001) islands near the (022) GaAs reflection. K and L reciprocal lattice units refer to the lattice of bulk GaAs. This scan allows us to associate horizontal and vertical lattice parameters, as represented by dashed lines for two pairs of values K_1, L_1 and K_2, L_2.

InAs island lattice by the substrate leads to a vertical (out-of-plane) expansion. In reciprocal space, this can be seen from the x-ray map, where for larger K, the main intensity is seen for smaller L.

In order to start a quantitative analysis of figure 2, a few assumptions were made. First, each portion of the islands at height z with respect to the substrate has a horizontal lattice parameter. This layer is constrained by a bi-axial strain that creates a tetragonal distortion in the islands unit cells, changing the out-of-plane lattice parameter. Finally, there is a direct correlation between horizontal and vertical lattice parameters. These approximations are valid assuming that the island behaviour is similar to the bulk, meaning that it has

the same elastic constants. Near the surface of the islands these approximations may not be valid.

The measurement of figure 2 allowed us to correlate the in-plane and out-of-plane lattice parameters. This correlation was obtained by an association of K values to in-plane lattice parameters and L values to out-of-plane lattice parameters. This association was obtained as follows: for each L scan for K fixed, an in-plane lattice parameter $a_\parallel = a_{\mathrm{GaAs}} * 2/K$ was associated. The peak position of each L scan (determined from a Gaussian fit) was associated to the out-of-plane lattice parameter $a_\perp = a_{\mathrm{GaAs}} * 2/L_{\mathrm{peak}}$. In this way, pairs of values of $(a_\parallel, a_\perp)$, obtained from (K, L_{peak}) pairs, were obtained. The left plot of figure 3 shows values of $(a_\parallel, a_\perp)$ related to regions of the island with these two lattice parameters.

Two factors can be responsible for changes in the unit cells volume inside the InAs islands: interdiffusion and elastic deformation (strain). As a starting point only interdiffusion was considered. By Vegard's law, a variation of lattice parameter of an alloy is linear with respect to its composition. The average lattice parameter for an $In_{1-x}Ga_xAs$ alloy is given by

$$a_{\mathrm{local}} = x a_{\mathrm{GaAs}} + (1 - x) a_{\mathrm{InAs}}, \tag{1}$$

where x ($0 < x < 1$) is the Ga concentration and a_{local} the local lattice parameter of the unit cell if it is not strained. The relationship between the Ga concentration and the local lattice parameter a_{local} is given by

$$x = \frac{a_{\mathrm{local}} - a_{\mathrm{InAs}}}{a_{\mathrm{GaAs}} - a_{\mathrm{InAs}}}. \tag{2}$$

As a first approximation, one can calculate the unit cell volume from pairs of values $(a_\parallel, a_\perp)$, considering that the unit cell is tetragonal, i.e. $V = a_\parallel^2 a_\perp$. The right part of figure 3 shows the unit cell volume as a function of in-plane lattice parameter. This result shows that the unit cell volume diminishes as the in-plane lattice parameter decreases. This is a first indication of the presence of Ga inside the islands. However, before the Ga concentration can be calculated one must consider the effect of strain imposed by the substrate.

A more realistic approximation of the behaviour of this system can be obtained using the elastic properties of InAs and GaAs. The in-plane and out-of-plane strain components are defined as:

$$\varepsilon_\parallel = 2\frac{a_\parallel - a_{\mathrm{local}}}{a_\parallel + a_{\mathrm{local}}} \tag{3a}$$

and

$$\varepsilon_\perp = 2\frac{a_\perp - a_{\mathrm{local}}}{a_\perp + a_{\mathrm{local}}}. \tag{3b}$$

The relationship between vertical and horizontal strain components depends on the type of compression (axial or bi-axial) the material is subjected to. In the case of an uni-axial compression, the unit cell can expand in the two other directions. This expansion will be given by (see, e.g. [6])

$$\varepsilon_\perp = -\nu \varepsilon_\parallel, \tag{4}$$

where ν is the Poisson ratio of the alloy.

For a bi-axial compression the strain components are related by [6]:

$$\varepsilon_\perp = \frac{-2\nu}{1 - \nu}\varepsilon_\parallel. \tag{5}$$

For most materials, the Poisson ratio varies between 0.2 and 0.4 (for a non-compressible material, ν is equal to 0.5). Inserting $\varepsilon_\perp$ and $\varepsilon_\parallel$ (equations (3a) and (3b)) into equation (5), a_{local} can be found solving the equation:

$$(a_\perp - a_{\mathrm{local}})(a_\parallel + a_{\mathrm{local}}) = \left(-\frac{2\nu}{1 - \nu}\right)(a_\perp + a_{\mathrm{local}}) \times (a_\parallel - a_{\mathrm{local}}), \tag{6}$$

leading to the equation

$$-(a_{\mathrm{local}})^2(1 + \nu) + a_{\mathrm{local}}(1 - 3\nu)(a_\perp - a_\parallel) + a_\perp a_{\mathrm{local}}(1 + \nu) = 0. \tag{7}$$

This quadratic equation has the following solutions

$$a_{\mathrm{local}} = \Big[(3\nu - 1)(a_\perp - a_\parallel) \pm \sqrt{(1 - 3\nu)^2(a_\perp - a_\parallel)^2 + 4(1 + \nu)^2 a_\perp a_\parallel}\Big] \times [-2(1 + \nu)]^{-1}, \tag{8}$$

where one of the solutions leads to a negative lattice parameter. From the positive value of a_{local} and equation (2), the Ga concentration could be estimated.

The InAs and GaAs Poisson ratios are 0.35 and 0.31 [7], respectively. For a more accurately determination of the Ga concentration, a self-consistent procedure to calculate a_{local} (equation (8)) was adopted: first the InAs Poisson ratio was used to obtain an initial estimate for the Ga concentration. Vegard's law was then employed to obtain a new Poisson ratio. A corrected value for the Poisson ratio was obtained from the concentration of Ga and In:

$$\nu_{\mathrm{alloy}} = x\nu_{\mathrm{GaAs}} + (1 - x)\nu_{\mathrm{InAs}}. \tag{9}$$

This new Poisson ratio was taken again to equation (8) and new values for a_{local} and x were found. These steps were repeated until the variation in the Ga concentration was smaller than 0.01%. The result of this calculation can be seen in figure 4. We have composed the results of the Ga content as a function of in-plane parameter $a_\parallel$ with the relationship between island diameter D to $a_\parallel$ obtained from figure 1 and the height information obtained from the α_f-profiles.

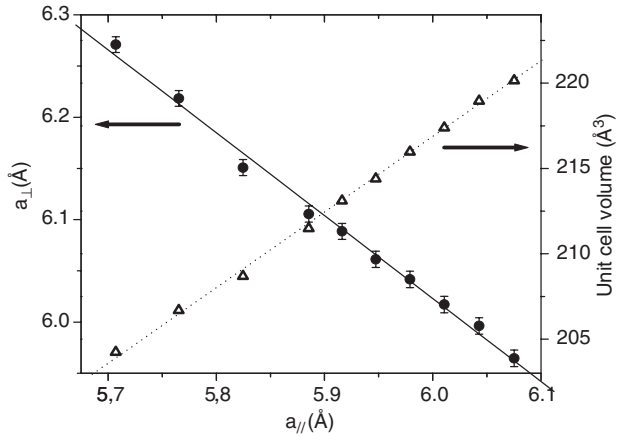

Figure 3. Left: correlation between in-plane and out-of-plane lattice parameters in InAs islands. Right: unit cell volume as a function of horizontal lattice parameter. The error bars are smaller than the symbol sizes.

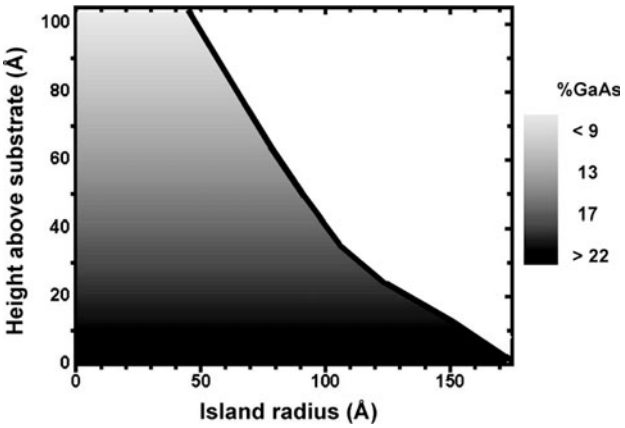

Figure 4. Ga content map in InAs : GaAs(001) islands determined using the method described in the text.

The interpretation of the plot of figure 4 is straightforward. For regions close to substrate, where the horizontal lattice parameter is near GaAs value the Ga concentration is higher (∼25%). Closer to the island top, the presence of Ga is smaller. This result is probably due to kinetic limited Ga interdiffusion during the deposition of InAs.

4. Conclusions

In conclusion, we have used reciprocal space mapping under grazing incidence geometry to study the local tetragonal distortion of InAs islands grown on GaAs(001). Using elasticity theory, we have been able to infer the degree of intermixing between the material of the substrate and the island. This relationship was obtained using the Poisson ratio of the two constituents of the island (InAs and GaAs). For the case of InAs/GaAs(001) we observed a variation of Ga content from 25% (base of the island) up to 8% (top of the islands). This method is in principle capable of determining the complete three-dimensional strain and chemical status of any island–substrate system.

Acknowledgments

The authors acknowledge support from the Brazilian research program PRONEX as well as the funding agencies FAPEMIG and CNPq. The research performed at the Brazilian Synchrotron Light Source was partially supported by ABTLus.

References

[1] Joyce P B, Krzyzewski T J, Bell G R, Joyce B A and Jones T S 1998 *Phys. Rev.* B **58** R15981
[2] Kegel I, Metzger T H, Fratzl P, Peisl J, Lorke A, Garcia J M and Petroff P M 1999 *Europhys. Lett.* **45** 222
Kegel I, Metzger T H, Lorke A, Peisl J, Stangl J, Bauer G, Nordlund K, Schoenfeld W V and Petroff P M 2001 *Phys. Rev.* B **63** 35318
[3] Zhang K, Heyn Ch, Hansen W, Schmidt Th and Falta J 2000 *Appl. Phys. Lett.* **77** 1295
[4] Stangl J, Daniel A, Holy V, Roch T, Bauer G, Kegel I, Metzger T H, Wiebach Th, Schmidt O G and Eberl K 2001 *Appl. Phys. Lett.* **79** 1474
[5] Malachias A, Magalhães-Paniago R, Neves B R A, Rodrigues W N, Moreira M V B, Pfannes H-D, Oliveira A G, Kycia S and Metzger T H 2001 *Appl. Phys. Lett.* **79** 4342
[6] Tsao J Y 1993 *Materials Fundamentals of Molecular Beam Epitaxy* (London: Academic)
[7] Landolt-Börnstein 1982 *Physics of Group IV Elements and III–V Compounds* vol 17a (Berlin: Springer)

X-ray study of strain and composition of Si/$Ge_{0.85}Si_{0.15}$ (111) islands grown in Volmer-Weber mode

A. Malachias[a)]
Departamento de Física, Uuniversidade Federal de Minas Gerais, Caixa Postal 702, CEP 30123-970, Belo Horizonte, Minas, Gerais, Brazil and European Synchrotron Radiation Facility, Boîte Postale 220, F-38043 Grenoble Cedex, France

R. Magalhães-Paniago
Departamento de Fisica, Universidade Federal de Minas Gerais, Caixa Postal 702, CEP 30123-970, Belo Horizonte, Minas Gerais, Brazil and Laboratório Nacional de Luz Síncrotron, Caixa Postal 6192, CEP 13084-971, Campinas, São Paulo, Brazil

S. Kycia
Laboratório Nacional de Luz Sincrotron, Caixa Postal 6192, CEP 13084-971, Campinas, São Paulo, Brazil

David G. Cahill
Department of Materials Science and Materials Research Laboratory, University of Illinois, Urbana, Illinois 61801

(Received 26 January 2004; accepted 7 June 2004)

Si islands were grown on Ge (111) in Volmer-Weber growth mode with a 40-nm thick $Ge_{0.85}Si_{0.15}$ buffer. The state of strain and chemical composition of these islands were evaluate by grazing incidence anomalous x-ray diffraction. The results show evidence of lattice coherence and Ge-Si intermixing. A direct relationship between increase in substrate temperature and enhancement of alloying was found, evidencing the importance of atomic interdiffusion in this growth mode. © *2004 American Institute of Physics*. [DOI: 10.1063/1.1777396]

I. INTRODUCTION

Self-assembled islands have been intensively investigated during the past few years, due to their potential applications in the optoelectronic industry. Several experimental techniques, each presenting specific advantages, have been used to study islands properties, both from the morphological as well as the structural point of view. Atomic force microscopy (AFM) and scanning tunneling microscopy (STM) have become crucial in determining the island morphology and size distribution.[1–3] Chemical composition profiles of individual islands have been extracted from transmission electron microscopy (TEM) data[4,5] and electron energy-loss spectroscopy.[6] For statistical averaging of this information, surface sensitive x-ray diffraction has been used as a unique tool to observe simultaneously lattice coherence and composition inside these nanostructures.[7–9]

Grazing incidence x-ray diffraction experiments have been particularly successful in mapping out the strain distribution and chemical composition inside self-assembled islands. However, this success was limited to Stranski-Krastanov systems such as InAs on GaAs (Ref. 7) and Ge on Si (Refs. 8 and 9). In these heteroepitaxial SK systems a wetting layer is formed before three-dimensional islands start to appear. The existence of this wetting layer play a role in smoothing out the stress concentrations at the edge of the islands. This favors the growth of coherent structures, desirable for optoelectronic applications.

Although many features of SK systems were clarified by x-ray studies, the elastic and chemical properties of Volmer-Weber (VW) islands are poorly understood, In fact, due to the high surface energy of the components, relaxed structures are predominantly formed in many (VW) islands systems such as InAs on GaP[10] and Si on Ge (111).[11] These relaxed structures are generally incoherent, often presenting misfit dislocations. Nevertheless, it has been shown that coherent Si islands are formed on Ge (111) when a thin $Ge_{0.85}Si_{0.15}$ film is grown between islands and substrate. Recently, the evolution of these coherent islands was characterized by STM, TEM, and AFM.[12] However, these techniques are not sensitive to the state of strain and chemical composition of these islands. In this work x-ray anomalous scattering was used to quantitatively evaluate strain and Ge interdiffusion inside Si islands.

II. SAMPLE CHARACTERIZATION

The samples investigated in this work were grown on Ge (111) substrates by molecular beam epitaxy. Before the deposition of Si, a 40 nm thick Ge buffer layer was grown at 380 °C followed by a $Ge_{0.85}Si_{0.15}$ film with the same thickness grown at 500 °C. After these steps eight equivalent bilayers (BL) of Si were deposited at two different temperatures with a flux of 1×10^{14} cm^{-2} s^{-1}. Sample *A* was grown at 500 °C and sample *B* at 650 °C. Due to the lattice parameter mismatch of 3.6%, between Si and the substrate tensile-strained island were formed. A detailed description of the growth procedure can be found in Ref. 12.

Figures 1(a) and 1(b) show 1-μm^2 AFM images of samples *A* and *B*, respectively, measured in Digital Instruments Nanoscope 4 microscope working in TappingMode.[13]

[a)]Electronic mail: angeloms@fisica.ufmg.br

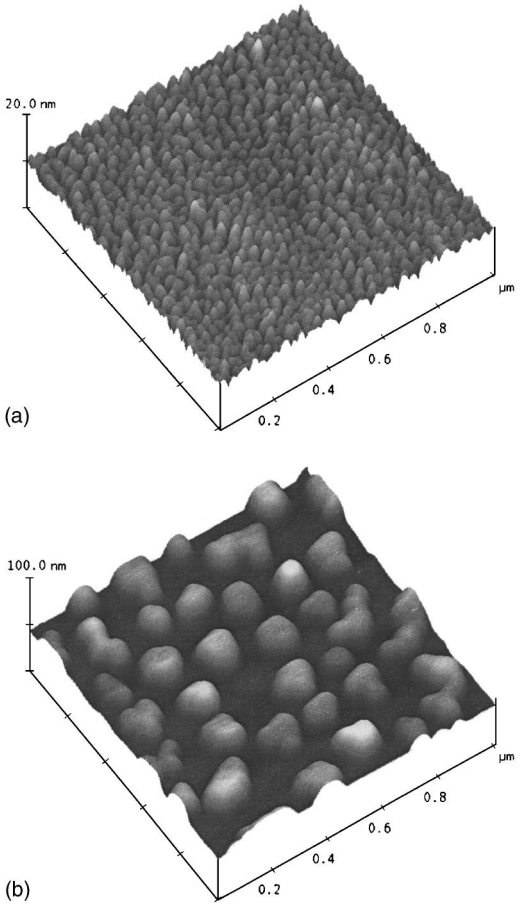

FIG. 1. 1-μm^2 AFM images of sample *A* (a), grown at 500 °C, and sample *B* (b), grown at 650 °C. The height scale in (b) is five times larger than in (a).

The islands density and size distribution were evaluated from 1-μm^2 area to sample *A* and 5-μm area to sample *B*. Sample *A* presents an ensemble of islands of height 2.6 ± 0.5 nm and radius 20 ± 4 nm; the island density is 7×10^{10} cm^{-2}. In sample *B* the island are larger, presenting a broader size distribution. The height of these nanostructures is 19 ± 5 nm and radius 80 ± 40 nm; the island density is 4×10^{9} cm^{-2}.[12] These measurements lead us to a simple calculation of the total island volume in equivalent BL. In sample *A* the island ensemble has a total volume equivalent to 7 BL, suggesting little Si interdiffusion into the $Ge_{0.85}Si_{0.15}$ film. In sample *B* the islands volume corresponds to 15.5 BL, roughly twice the amount of deposited Si, indicating a substantial interdiffusion of Ge into the Si islands.[14] Although AFM can be used to evaluate the average Ge content of Si islands, strain coherence, and chemical distribution cannot be properly mapped out.

III. X-RAY RESULTS AND ANALYSIS

In order to quantitatively evaluate the strain status and the SiGe composition profile inside these islands grazing incidence anomalous (resonant) x-ray diffraction measurements near the (220) in-plane substrate Ge reflection were performed at the XD1 beam line at the Brazilian National Synchrotron Light Source (LNLS). This beam line is

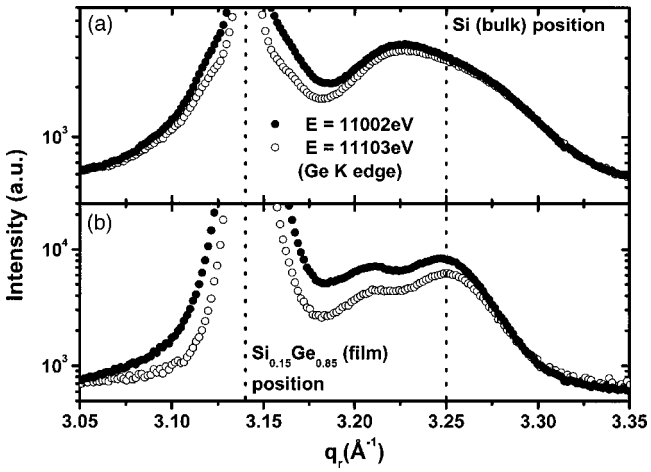

FIG. 2. Anomalous x-ray radial scans near the (220) Ge in-plane reflection for samples *A* (a) and *B* (b). The vertical dashed lines indicate the reciprocal space position for bulk Si and the $Ge_{0.85}Si_{0.15}$ alloy film. Open dots correspond to scans performed with the x-ray photon energy equal to the Ge *K* absorption edge (11 103 eV) while solid dots correspond to scans performed at 11 002 eV. The difference in scattered intensity of open dot and solid dot curves comes from the presence of Ge atoms inside islands.

equipped with a two circle θ-2θ diffractometer with an independent incident angle (α_i) circle. Both samples were illuminated at a grazing incidence angle $\alpha_i=0.15°$ at two selected x-ray photon energies: 11 002 eV and 11 103 eV (Ge *K* absorption edge). The x-ray scattering was measured as a function of $q_{\text{radial}}=q_r=(4\pi/\lambda)\sin(2\theta/2)$, which is strain sensitive, and $q_{\text{angular}}=q_a=q_r\sin(2\theta/2-\omega)$, which is size sensitive, integrating the exit α_f angle from 0 to 1.5°.

Two types of scans were done. A radial scan was performed coupling θ to 2θ. Thus, by Bragg's law $\lambda=2d\sin(2\theta/2)$, this scan was sensitive to the strain of the sample, since for each value of $2\theta(q_r)$, regions of different lattice parameter $a'=2\pi/q_r$ were probed. Angular scans were performed solely by $\theta(q_a)$, with fixed $2\theta(q_r)$. These scans were size sensitive, since the size of each region with a given lattice parameter can be inferred from the width of the q_a-scan profile.[7,8]

Figures 2(a) and 2(b) show radial scans along the (220) direction performed with samples *A* and *B*, respectively, at two different x-ray photon energies. In both samples a reasonable amount of x-ray scattered intensity was measured between the $Ge_{0.85}Si_{0.15}$ film peak and relaxed Si (bulk) position. These scans clearly evidence the existence of a lattice parameter gradient inside Si islands. Such a gradient is generally a characteristic of coherent or partially coherent nanostructures.[15]

In Figs. 3(a) and 3(b) some angular scans performed along the $[1-1\,0]$ direction at 11 002 eV are shown. Using these scans the dependence of island size to its local lattice parameter, $a'=2\pi/q_r$, was quantified. The scans start near the GeSi alloy reciprocal lattice position ($q_r=3.14$ Å^{-1}) and go up to the relaxed Si position ($q_r=3.25$ Å^{-1}). It can be seen for both samples that, as q_r increases, meaning that regions with smaller lattice parameter are been probed, the central maximum broadens. since the full width at half maxima of these angular diffraction profiles is inversely proportional to the size of the scattering object, broad angular scans corre-

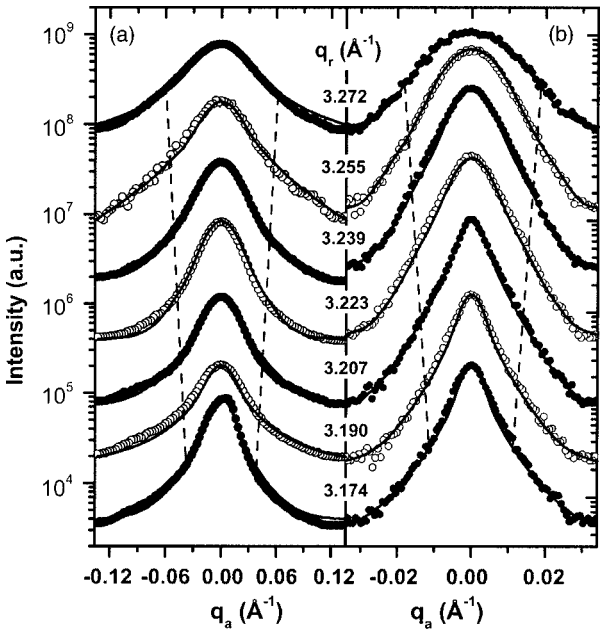

FIG. 3. Angular scans along the [1 −1 0] direction for (a) sample *A* and (b) sample *B*. The solid lines are fits assuming a square-shaped isostrain region with a size distribution of 70%. Dashed lines were drawn as guide to the eyes, indicating the approximate width of each angular scan.

spond to small isostrain regions (located at islands apex), while sharp angular scans are related to large regions (located at islands bottom).

The size of each isolattice parameter region was inferred from the profile of the scattering stemming from portions of the island limited by planes parallel to the substrate surface. The solid line fits to the angular scans were done assuming that islands have a square section of side L, with $I(q_a) \propto |\sin(q_a L/2)/q_a|^2$.[7,8] While this assumption may not be completely correct, it yields values for L which can be considered good estimates of the local mean island diameter. The fits were performed adjusting only the island side length L for every fixed q_r (corresponding to a fixed local lattice parameter a'), also including a size distribution of 70%. This value, larger than the AFM size distribution was used to broaden the intensity maxima, also washing out the subsidiary wings of angular scan fits, compensating the mosaic spread of islands, which cannot be evaluated by the measurements shown here. Figure 5(a) shows the relation between the side lengths L obtained from fits of Fig. 3 and the local lattice parameter. The angular scans conserve the typical behavior observed for coherent islands.[7,15] They are sharp in regions with small q_r close to the SiGe alloy, presenting a monotonic broadening as q_r increases to the Si value.

In order to determine the Si/Ge chemical composition inside islands radial scans were performed close to the Ge (220) reflection at two specific energies. One energy was 11 002 eV, below the Ge *K* absorption edge. The other energy was 11 103 eV, right at the Ge *K* absorption edge, where the Ge atomic scattering factor is significantly lower. In the radial scans of Figs. 2(a) and 2(b) the change in the scattered intensity for the two x-ray energies can be seen for samples *A* and *B*, respectively. Since at the Ge *K* edge the Ge atomic scattering factor f_{Ge} diminishes by 30%, this difference in intensity can be directly associated with the presence of Ge atoms inside islands.[8] It can be seen in both samples that islands bases are Ge-rich, since close to the GeSi alloy position a remarkable intensity contrast was observed comparing the two measured energies. Furthermore, the island apexes are composed of pure Si, corresponding to regions where no contrast was observed.

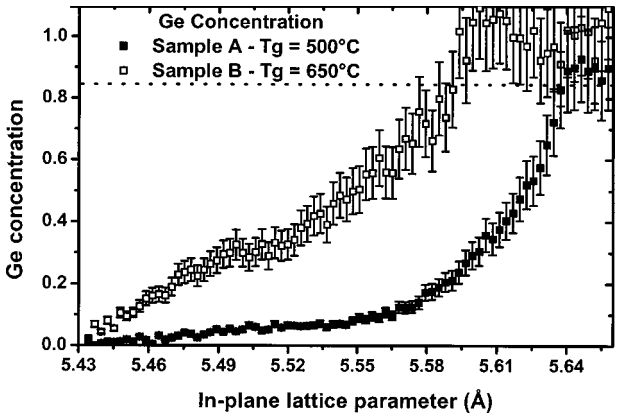

FIG. 4. Ge concentration as a function of lattice parameter obtained from the scattered intensity contrast of radial scans of Fig. 2; solid squares correspond to sample *A* and open squares to sample *B*. A 1.4 eV energy uncertainty was used to calculate the error bars. The dashed line indicates the upper nominal Ge concentration of 0.85.

For a quantitative determination of the Si concentration, the variation of the scattering factor of Ge (f_{Ge}) near its absorption edge was used. In this particular case, only two different species were involved and the chemical contrast was obtained by varying only f_{Ge} while f_{Si} was the same for the two measured energies.[8] In this case, the x-ray scattered intensity at the (220) reflection is proportional to the square of the sum of Si and Ge concentrations, multiplied by their respective scattering factors[8]

$$I_{(220)} = K|C_{\mathrm{Ge}} f_{\mathrm{Ge}} + G_{\mathrm{Si}} f_{\mathrm{Si}}|^2, \tag{1}$$

where C_{Ge} and C_{Si} are the Ge and Si concentrations (with $C_{\mathrm{Ge}} + C_{\mathrm{Si}} = 1$), f_{Ge} and f_{Si} are the Ge and Si scattering factors, and K is a constant which contains all the other scattering parameters (kept constant at the two used energies). Since at each of the two energies used the Ge atomic scattering factor is different, the ratio of the measured intensities is given by

$$\frac{I_1}{I_2} = \left| \frac{C_{\mathrm{Ge}} f_{\mathrm{Ge1}} + C_{\mathrm{Si}} f_{\mathrm{Si}}}{C_{\mathrm{Ge}} f_{\mathrm{Ge2}} + C_{\mathrm{Si}} f_{\mathrm{Si}}} \right|^2, \tag{2}$$

where I_1 and I_2 are the measured x-ray intensities and f_{Ge1} and f_{Ge2} are the atomic scattering factors of Ge at the Ge K edge (11 103 eV) and at 11 002 eV. The Ge concentration was then directly obtained from Eq. (2),

$$C_{\mathrm{Ge}} = \left(1 + \frac{f_{\mathrm{Ge2}}\sqrt{I_1} - f_{\mathrm{Ge1}}\sqrt{I_2}}{f_{\mathrm{Si}}(\sqrt{I_2} - \sqrt{I_1})} \right)^{-1}. \tag{3}$$

Figure 4 shows the Ge composition as a function of the in-plane lattice parameter for samples *A* and *B*.[16] In this figure the error bars were estimated considering the 1.4 eV monochromator energy fluctuation, typical of our experimental setup. It can be seen the Ge concentration profile of

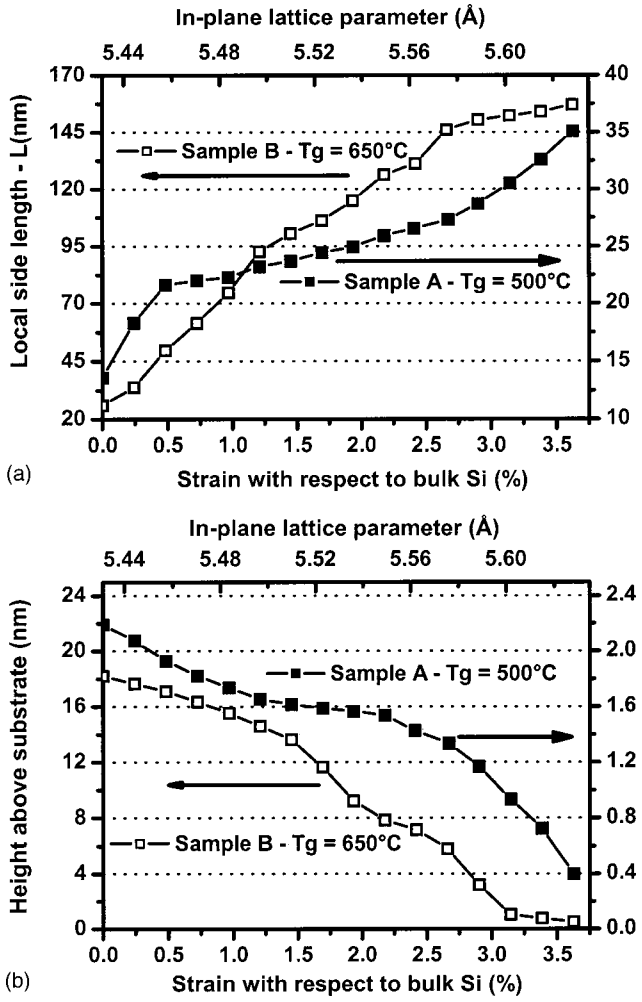

FIG. 5. (a) Island local side length as a function of strain for samples *A* (solid squares) and *B* (open squares). (b) Height as a function of strain for samples *A* and *B*. The result of (b) was obtained correlating the side lengths from angular scans of Fig. 3 and AFM island profiles.

sample *A* varies abruptly from the alloy concentration to pure Si as the lattice parameter diminishes. This concentration gradient is more monotonic for sample *B*, with the islands showing a higher average Ge concentration than in sample *A*. Notice that for sample *B* and lattice parameter larger than 5.6 Å the Ge concentration seems to be higher than 0.85. It is unclear if this is due to surface segregation or simply a systematic error of this x-ray method.

By correlating the AFM results (height × diameter) and angular scans side lengths of Fig. 3 (diameter × local lattice parameter), the relation between lattice parameter and height was obtained as seen in Fig. 5(b).[8,9] Finally, using the relationship between Ge composition and local lattice parameter. given in Fig. 4, an AFM-based composition map was made. In Figs. 6(a) and 6(b) the real space composition profiles of samples *A* and *B* are shown. The interpretation of these maps is quite straightforward. A higher Ge concentration can be found for regions close to the substrate while at the islands top the presence of Ge is smaller. It can be seen that interdiffusion is much more effective in sample *B*.

IV. CONCLUSIONS

Several conclusions can be drawn with respect to strain and composition of our Si islands studied in this work. X-ray diffraction was employed to show that Si islands can be grown coherently in Volmer-Weber mode on $Ge_{0.85}Si_{0.15}$ (111). They exhibit a strain gradient that was observed up to now only in Stranski-Krastanov systems. A strain relaxation gradient was clearly observed inside Volmer-Weber islands.

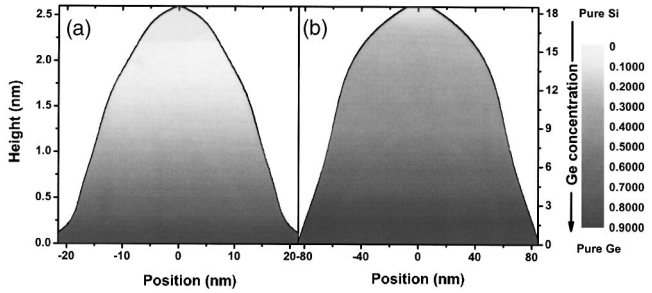

FIG. 6. Real space average chemical composition maps for samples *A* (a) and *B* (b). The islands shapes were obtained from typical AFM profiles.

Anomalous x-ray scattering measurements evidenced the presence of Ge from the buffer incorporated into the Si island. This incorporation dramatically increases as the substrate growth temperature is raised from 500 °C to 650 °C. This result is in agreement with the estimates of Ge incorporation obtained from the atomic force microscopy. Since both germanium and silicon crystallize in the diamond structure, the conclusive observation of strain gradient and interdiffusion in our islands may not be generally applicable to other systems. To achieve a completely coherent ensemble of Si islands, without mosaic spread, one may need to vary the SiGe buffer layer composition and perform AFM measurements to get the alloy concentration that minimizes the size distribution.

ACKNOWLEDGMENTS

This work was supported by CNPq (Brazilian Science Agency), ABTLuS, and Instituto do Milenio—Nanociências.The authors acknowledge the U.S. Department of Energy, Division of Materials Sciences under Award No. DEFG02-91ER45439, through the Frederick Seitz Materials Research Laboratory at the University of Illinois at Urbana Champaign.

[1]C. J. Huang, Y. H. Zuo, D. Z. Li, B. W. Cheng, L. P. Luo, J. Z. Yu, and Q. M. Wang, Appl. Phys. Lett. **78**, 3881 (2001).
[2]G. Costantini, C. Manzano, R. Songmuang, O. G. Schmidt, and K. Kern, Appl. Phys. Lett. **82**, 3194 (2003).
[3]T. Suzuki, Y. Temko, and K. Jacobi, Phys. Rev. B **67**, 045315 (2003).
[4]S. A. Chaparro, J. Drucker, Y. Zhang, D. Chandrasekhar, M. R. McCartney, and David J. Smith, Phys. Rev. Lett. **83**, 1199 (1999)
[5]X. Z. Liao, J. Zou, D. J. H. Cockayne, J. Wan, Z. M. Jiang, G. Jin, and Kang L. Wang, Phys. Rev. B **65**, 153306 (2002).
[6]M. Floyd, Y. Zhang, K. P. Driver, J. Drucker, P. A. Crozier, and D. J. Smith, Appl. Phys. Lett. **82**, 1473 (2003).
[7]I. Kegel *et al.*, Phys. Rev. B **63**, 035318 (2001).
[8]A. Malachias, S. Kycia, G. Mederos-Ribeiro, R. Magalhães-Pnaiago, T. I. Kamins, and R. Stanley Williams Phys. Rev. Lett. **91**, 176101 (2003).
[9]T. U. Schülli, J. Stangl, Z. Zhong, R. T. Lechner, M. Sztucki, T. H. Metzger, and G. Bauer, Phys. Rev. Lett. **90**, 066105 (2003).
[10]R. Leon, Appl. Phys. Lett. **72**, 1356 (1998).
[11]T. H. Metzger *et al.*, Thin Solid Films **336**, 1 (1998).
[12]A. Raviswaran, C.-P. Liu, J. Kim, D. G. Cahill, and J. M. Gibson, Phys.

Rev. B **63**, 125314 (2001).
[13]TappingMode® is a trademark of Digital Instruments, Santa Barbara, CA.
[14]P. B. Joyce, T. J. Krzyzewski, G. R. Bell, B. A. Joyce, and T. S. Jones, Phys. Rev. B **58**, R15981 (1998).
[15]A. Malachias *et al.*, Appl. Phys. Lett. **79**, 4342 (2001). Here the term "coherent" is employed to dislocations-free islands while "partially coherent" is related to islands which have some dislocations but still exhibit a strain gradient. The term "incoherent" is reserved for a strain-free structure.
[16]The radial scans of Figs. 2(a) and 2(b) are a result of the convolution of strain relaxation and size broadening. The estimation of the lattice parameter using a direct correlation with q_r is, consequently, a rough approximation.